Electrochemical Biosensor Development: Experimental and Computational Approaches Using Cu(I)-Catalysis and Click Chemistry

Marzia Amini
Nanobiotechnology

Master Thesis

Department of Materials and Production
Aalborg University

AALBORG UNIVERSITY
STUDENT REPORT

Title:
Electrochemical Biosensor Development: Experimental and Computational Approaches Using Cu(I)-Catalysis and Click Chemistry

Project Period:
Autumn Semester
2nd of September 2024 - 3rd of March 2025

Author:
Marzia Amini

Supervisors:
Leonid Gurevich
Thor Lindgren Videbæk Pedersen

Copies: 1

Page Numbers: 121

Date of Completion:
3rd of March 2025

Abstract:

This project successfully developed and optimised enzyme- and antibody-functionalised SPGEs through electrochemical experiments and computational modelling. Three methods were tested, each addressing electrode functionalisation and detection. A key challenge was SPGE reuse, with performance degrading over multiple uses—especially in Method 3, where CV showed a ∼50% signal drop compared to Method 1. Method 1 functionalised SPGEs with MUA, HRP, and Strep-HRP. CV confirmed MUA and enzyme binding, while EIS showed MUA had the highest charge transfer resistance. HRP and Strep-HRP exhibited increased impedance with dilution, though Strep-HRP had weaker signals. CA showed higher currents at lower dilutions, but non-specific binding made this method unreliable. Method 2 improved specificity by covalently immobilising BAM1676 antibodies on MUA-functionalised SPGEs. EIS showed concentration-dependent charge transfer resistance, while CA confirmed enhanced detection sensitivity. Method 3 introduced click chemistry for efficient functionalisation. A novel protocol was developed, with CA confirming specific Strep-HRP binding. This approach is highly promising, but needs further optimisation and testing. COMSOL Multiphysics® was used to simulate redox reactions at various electrode surfaces, with 3D biosensor models closely matching experimental CV data. Simulations revealed steric effects of SAMs, enzymes, and antibodies on electron transfer kinetics, providing a foundation for optimising biosensor performance and electrode spacing. Furthermore, the models can be extended to include systems with multiple working electrodes.

Preface

This Master Thesis was written by Marzia Amini during the 4^{th} semester of the Nanobiotechnology study program at Aalborg University. The project was carried out from September 2^{nd} 2024 to March 3^{rd} 2025 under the supervision of Leonid Gurevich, associate professor, and Thor Lindgren Videbæk Pedersen, Industrial PhD, from the Department of Materials and Production at Aalborg University.

The aim of this project is to develop and optimise a click chemistry-based functionalisation strategy for biosensor applications, and investigate the biosensor platform through computational modelling.

The project report is structured into six chapters. Chapter 1 provides a general introduction to the project, outlining its scope and objectives. Chapter 2 presents the relevant theoretical background. Chapter 3 outlines the project approach and objectives. Chapter 4 provides a comprehensive evaluation of the experimental procedures carried out during the project period, including lists of the chemicals, materials, and equipment used. Chapter 5 presents the results, followed by a thorough analysis and discussion. This chapter is divided into four sections, where each section presents and discuss the findings from each method. Section 1-3 details the findings from Method 1 through 3, while section 4 presents and discusses the results from COMSOL Multiphysics® simulations with the bare electrode and with functionalised electrode. Supplementary information, including the optimised protocol developed for the click reaction in Method 3, are provided in the appendix. Finally, Chapter 6 presents the conclusions based on the results and discussion, along with suggestions for future work.

The project report is written in British English and uses Oxford comma. The citation style used is IEEE and is presented as [number] and the number refers to the specific reference in the bibliography. Figures without citation are made by the student. Furthermore, all figures are named "X.X" [e.g.: Fig. 5.4] while tables are named "X.X" [e.g.: Table 3.2].

Aalborg University, March 3^{rd} 2025

Contents

Abbreviations & Acronyms

AA	Alkyne-Azide
Ab	Antibody
Ag	Silver
Au	Gold
AuNP	Gold Nanoparticle
CA	Chronoamperometry
CE	Counter Electrode
CNM	Carbon Nanomaterial
CNT	Carbon Nanotube
Cu(I)	Reduced copper(I) ion
CuAAC	Cu-assisted Alkyne-Azide Cycloaddition
CV	Cyclic Voltammetry
DPV	Differential Pulse Voltammetry
dsDNA	Double-stranded DNA
EDC	1-Ethyl-3-(3-dimethylaminopropyl)carbodiimide
EDL	Electrochemical Double Layer
EIS	Electrochemical Impedance Spectroscopy
ELISA	Enzyme-linked Immunosorbent Assay
Fc	Ferroscene
FEM	Finite Element Model
FSCV	Fast Scan Cyclic Voltammetry
FTIR	Fourier-Transform Infrared
GCE	Glassy Carbon Electrode
GO	Graphene Oxide
HRP	Horseradish Peroxidase
LOD	Limit-Of-detection
ME	Microelectrode
MES	2-Morpholinoethanesulfonic acid monohydrate
MPA	3-mercaptopropionic acid
MUA	11-mercaptpundocanoic acid
MWCNT	Multi-Walled Carbon nanotube
NGAL	Neutrophil Gelatinase-Associated Lipocalin
NHS	N-Hydroxysuccinimide
OCP	Open Circuit Potential
POC	Point-of-care
PVA	Polyvinyl Alcohol
RE	Reference Electrode
rGO	Reduced Graphene Oxide
SAM	Self-Assembled Monolayer

SPCE	Screen-printed Carbon Electrode
SPGE	Screen-printed Gold Electrode
SPE	Screen-printed Electrode
ssDNA	Single-stranded DNA
SWCNT	Single-walled Carbon Nanotube
SWV	Square Wave Voltammetry
UME	Ultramicroelectrode
WE	Working Electrode
Z	Impedance

1 Introduction

The timely detection of biomarkers related to certain infections or diseases is crucial when rapid diagnosis and intervention are necessary to improve patient outcomes, prevent disease progression, or enable appropriate therapeutic strategies. Typically, blood samples from patients are processed in the laboratories of hospitals or clinics. Additionally, it requires certain equipment and trained personnel to operate it, making it a long and inefficient process. Consequently, there is a high demand for easy-to-operate and portable Point-of-Care (POC) devices that can speed up the process and timely and accurately detect biomarkers. This has resulted in an increasing interest in developing immunoassay-based biosensors for the selective detection of specific biomarkers. [1]–[5]

Traditionally, Enzyme Labelled Immunosorbent Assay (ELISA) is used for immunoassay-based detection methods. More specifically, the sandwich immunoassay is used. This method ensures highly specific, accurate, and reproducible results. However, despite its many advantages, the Sandwich ELISA method is also very time-consuming, expensive, and not user-friendly. Thus, in an attempt to overcome these limitations and develop user-friendly portable POC biosensors, the Sandwich ELISA method has been successfully integrated into miniaturised electrochemical biosensors. [4]–[6] A crucial step in miniaturising the Sandwich ELISA method into electrochemical biosensors is the efficient functionalisation of the electrodes, for which the click chemistry-based Copper(Cu)-catalysed Alkyne-Azide Cycloaddition (CuAAC) technique has emerged as a highly effective solution. This technique relies on the formation of strong covalent bonds between alkyne- and azide groups, with Cu(I) ions catalysing the reaction. CuAAC offers many advantages, including its suitability for use across a wide range of pH levels, solvents, and temperatures. Hence, it is widely used to immobilise biorecognition elements to different substrates without affecting their biological activity. [5], [7]

While CuAAC provides an efficient and versatile approach for electrode functionalisation, the development and optimisation of these electrochemical biosensors can greatly benefit from computational modelling. Combining the empirical approach (i.e. the experimental fabrication of electrochemical biosensors) with computational mod-

elling and simulations provides a comprehensive approach to address the challenges of biosensor design in a cost-effective and time-efficient manner. In recent years, Finite Element Modelling (FEM) and simulations have gained significant traction in engineering and nanotechnology, particularly in biosensor development. This computational approach allows for the development, optimisation, and testing of biosensors through mathematical modelling of entire systems. This way, the behaviour/response of separate components of the system can be studied under various conditions, making it easier to predict their outcome in real-world applications. [8]–[11]

In this context, COMSOL Multiphysics® is particularly useful. This software is a finite element multi-model simulator that offers a broad range of applications and possibilities for simulating physical and chemical phenomena, including electrochemistry. However, only a few state-of-the-art studies utilising COMSOL Multiphysics® for biosensor development have been reported (of which even few have been verified experimentally), with most studies focusing on electrode design and optimisation. This limitation arises from the inherent complexity of modelling entire electrochemical biosensor systems such as: 1) the identification of the dominant microscopic mechanisms, 2) definitions of synergies in the multiphysics models, 3) proper calibration of the experimental-related parameters, and 4) the analysis of signal generation and conditioning. Integrating COMSOL modelling and simulations with advanced electrode functionalisation techniques, like the Cu-catalysed click chemistry technique, provides a deeper understanding of biosensor behaviour while facilitating the design of robust, reliable, and high-performing POC electrochemical immunosensor devices. [8]–[11]

In the current thesis, the aim is to experimentally investigate and develop an electrochemical immunosensor platform utilising the CuAAC technique. The end goal is to develop an electrochemical immunosensor platform for the specific and accurate detection of several analytes from the same sample (i.e. multiple working electrodes (WE)). The first step, however, is to successfully functionalise and detect analytes with a single WE. Thus, screen-printed gold electrodes (SPGE) are functionalised layer-by-layer and verified after each step through the following electrochemical techniques: Cyclic voltammetry (CV), Electrical Impedance Spectroscopy (EIS), and Chronoamperometry (CA).

It is also of special interest to computationally investigate and develop an electrochemical immunosensor platform with multiple WEs. For this purpose, COMSOL Multiphysics® will be utilised. Initially, the aim is to develop a 3D COMSOL model of a miniaturised electrochemical cell consisting of a single WE, a reference electrode (RE), and a counter electrode (CE). Following the modelling of the single electrode system, CV, EIS, and CA simulations will be performed under different conditions (i.e. layer-by-layer functionalisation) in order to analyse their electrochemical activity.

2 Theoretical Background

2.1 Electrochemistry

Electrochemistry is the study of electron movement during oxidation and reduction (redox) reactions at charged electrode surfaces. In these processes, each analyte undergoes oxidation or reduction at a specific potential, with the resulting current being directly proportional to its concentration. Electrochemistry thus connects the flow of electrons at the electrode-electrolyte interface to chemical changes. The driving force is controlled by the externally applied voltage, which adjusts the energy of the electrons in the electrode, allowing for precise control over the reaction. [12]–[14]

When an external potential is applied to an electrochemical system, the electrode acquires a charge, thereby attracting oppositely charged ions from the surrounding solution. This leads to the formation of an electrochemical double layer (EDL), which consists of two distinct regions: the Stern layer and the diffuse layer. In the Stern layer, ions are strongly adsorbed onto the electrode surface, while in the diffuse layer, ions are more loosely bound and thus move more freely. As a result, the concentration of counterions gradually decreases with increasing distance from the electrode surface. It follows then, that by regulating and adjusting the electrode potential, it is possible to control and manipulate the behaviour and arrangement of adsorbed ions/molecules. This, in turn, has a direct impact on the resulting electrochemical signal. Conversely, the concentration of electrolytes has a direct influence on the structure and thickness of the double layer. A high electrolyte concentration compresses the double layer (making it thinner), while a low concentration expands it. [15]–[17]

Thus, the understanding of charge transport (i.e. the flow of electrons), mass transport (i.e. diffusion, convection), and interfacial phenomena (e.g. double-layer capacitance and charging currents) at the electrode-electrolyte interface is critical for developing efficient electrochemical biosensors. These mechanisms are fundamental to the operation of electrochemical biosensors, where precise control of electrode reactions and optimisation of transport processes directly impact sensitivity and specificity. By understanding and manipulating these factors, biosensors can achieve efficient signal transduction, enabling real-time and reliable analyte detection. [12], [13]

2.1.1 Principles and Basics of Electrochemistry

First of all, processes occurring at the electrode-electrolyte interface can be broadly classified into faradaic and non-faradaic processes, based on whether electron transfer (i.e. charge transfer) takes place. These two classes of processes are fundamentally distinct in their mechanisms and behaviour. Faradaic processes involve the transfer of electrons across the electrode-electrolyte interface, leading to oxidation or reduction reactions. These processes are characterised by the movement of charge, where the amount of charge transferred is stoichiometrically related to the quantity of reactant consumed and product generated. This relationship is governed by Faraday's law, which states that the total charge transferred is proportional to the number of moles of electrons exchanged in the redox reaction. Electrodes at which faradaic processes occur are often referred to as charge-transfer electrodes because their defining feature is the flow of electrons between the electrode and the electroactive species in the solution. [12], [13]

In contrast, there are regions of potential where no charge transfer reactions occur because such processes are either thermodynamically or kinetically unfavourable. These processes, where no electron transfer occurs, are referred to as non-faradaic processes. Although no net charge crosses the interface in non-faradaic processes, external currents can still be observed transiently. These transient currents arise due to changes in factors such as the applied potential, electrode surface area, or composition of the solution. For example, altering the electrode potential can cause ions to rearrange at the interface, leading to the charging or discharging of the EDL, which behaves similarly to a capacitor. Such processes play a critical role in studies focused on the electrode-electrolyte interface, where phenomena like double-layer capacitance and adsorption dominate the system behaviour. [12], [13]

In Faradaic processes, a redox reaction can be described as two half-reactions; one representing the oxidation process (for an analyte A: $A \longrightarrow A^+ + e^-$) and the other the reduction process ($A + e^- \longrightarrow A^-$). The sum of the half-reactions gives the overall chemical reaction. Here, the overall redox reaction is balanced when the number of electrons lost by the reductant equals the number of electrons gained by the oxidant. It is, however, also possible to physically separate the oxidation and reduction half-reactions in space, as long as there is a complete circuit, including an external electrical connection (such as a wire) between the two half-reactions. As the reaction progresses, the electrons flow from the reductant to the oxidant over this electrical connection, producing an electric current. [12], [13] An overview of this can be seen in Figure 2.1.

The Electrochemical Cell

An electrochemical cell is an apparatus that can either generate electricity from a spontaneous redox reaction (Galvanic cell: $(\Delta G < 0)$) or consume electricity to drive a non-spontaneous reaction (electrolytic cell: $\Delta G > 0$). Both types utilise at least two

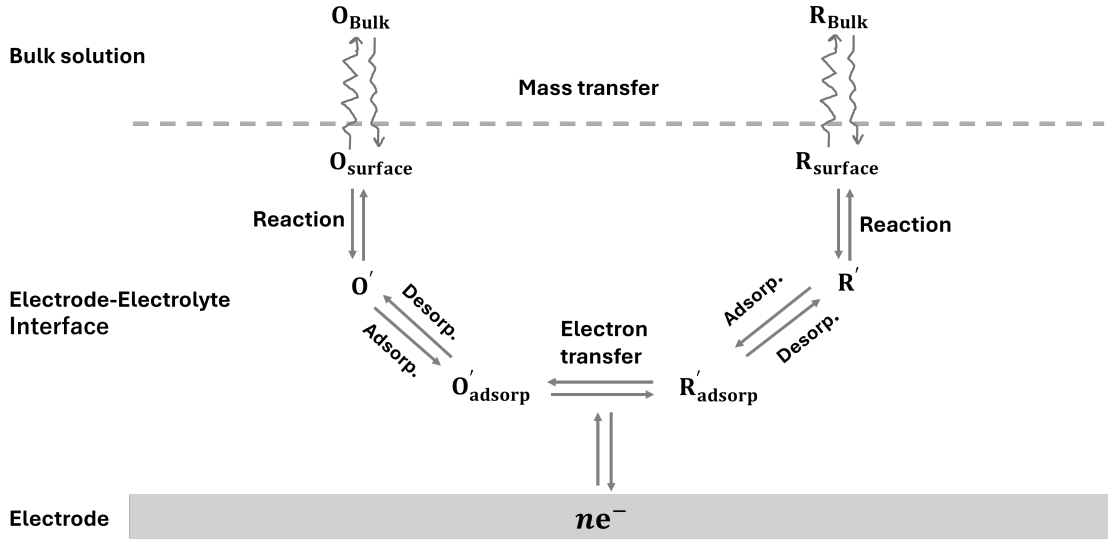

Figure 2.1: Process of an Electrochemical Reaction. During an electrochemical reaction, the analyte in the bulk solution moves toward the electrode surface region via mass transfer mechanisms (diffusion, migration, and/or convection). At the electrode surface, the analyte undergoes oxidation or reduction. After the reaction, the analyte may desorb from the electrode surface and move back into the bulk solution as either O_{Bulk} or R_{Bulk}, depending on the reaction direction, through the same mass transfer processes. Adapted from Patel et al.[13].

electrodes, which are usually made of solid conducting material connected to an external circuit that provides an electrical connection between the two parts of the system. The oxidation half-reaction occurs at one electrode (called the anode), and the reduction half-reaction occurs at the other electrode (called the cathode). When the circuit is closed, electrons flow from the anode to the cathode. The electrodes are also connected by an electrolyte solution, which is the ionic substance or solution that allows ions to transfer between the electrode compartments, thereby maintaining the system's electrical neutrality. [12], [13]

An electrochemical cell with a two-electrode system consists of a WE and a RE. Here, the redox reactions occur at the WE and are also where the generated current is recorded. To accurately isolate and understand the processes on the WE, the other half of the cell must be standardised. This is achieved using a RE. The RE provides a stable, reproducible, and invariant potential difference at its electrode-electrolyte interface. By maintaining a well-defined constant composition at the RE interface and ensuring that both oxidised and reduced species involved in the half-reaction are present, a fixed potential is secured that is virtually independent of the WE conditions. Because the RE maintains an unchanging potential, any shift in the overall cell potential can be attributed to the WE. [12], [13]

However, in practical electrochemical systems, the externally applied voltage, $E_{applied}$, differs from the actual voltage experienced in the electrochemical cell due to the ohmic

drop (iR_s). This ohmic drop arises from the current passing through the resistive solution of the electrolyte and is expressed by the following equation [12], [13]:

$$E_{applied} = E_{cell} - iR_s \tag{2.1}$$

Where $E_{applied}$ is the externally applied voltage and is distributed into two parts. The first part, E_{cell}, is the voltage required to drive the redox reaction at the WE, while the second part, iR_s, is the voltage loss due to resistance in the bulk solution. The ohmic drop depends on the electrolyte concentration and hence varies with the concentration and cell configuration. For small electrodes (e.g., nano- or micro-electrodes) with low current (in nano amperes) and sufficient electrolyte concentration, the ohmic drop is negligible, making a two-electrode system suitable. However, in cases where electrode sizes are greater than hundreds of micrometres and the electrolyte concentration is low, the ohmic drop becomes significant. To minimise this effect, a three-electrode system is preferred. This system introduces a third electrode: the CE. The CE helps separate the current path from the potential measurement, reducing interference between the WE and RE by only having it flow between the CE and RE. [12], [13]

Electric Current & Reaction Rates

As the potential of the WE relative to the RE is varied using an external power supply, a current can flow through the external circuit due to the electron transfer across the electrode-electrolyte interface as redox reactions take place. The flow of electrons is related to the stoichiometry of the electrochemical reaction taking place at the WE. Hence, the number of electrons involved in this transfer is specific to the reaction and reflects the chemical changes taking place. Specifically, for every mole of reactant undergoing the reaction, n moles of electrons must flow. Hence, the number of electrons transferred is directly proportional to the amount of reactant consumed or product generated, with n moles of electrons flowing for every mole of reactant transformed. The total amount of charge Q generated during the reaction is described by Faraday's law, which states [12], [13]:

$$Q = nFN \tag{2.2}$$

where Q is the total charge transferred (coulombs), n is the number of electrons transferred per mole of reactant, F is Faradays constant, and N is the number of moles of reactant transformed. The relationship between electric current and the rate of an electrochemical reaction is thus given by the following expression [12], [13]:

$$i = \frac{dQ}{dt} = nF\frac{dN}{dt} \tag{2.3}$$

where i is the electric current, Q is the total electric charge transferred, n is the number of electrons involved in the reaction per molecule of reactant, dQ/dt is the rate of change of charge with respect to time, and dN/dt is the rate at which the number of moles of reactant (or product) changes over time. The reaction rate can then be written as follows [12], [13]:

$$Rate = \frac{dN}{dt} = \frac{i}{nF} \tag{2.4}$$

Thus, the current observed in the external circuit reflects the rate of the electrochemical reaction. Higher reaction rates (more reactant consumed or product formed per unit time) result in a greater flow of electrons, and therefore a larger current. Conversely, slower reactions produce less current. Hence, a higher current means that the reaction is proceeding faster, as more charge (and hence more electrons) is being transferred per second. Thus, the current is a direct measure of the rate of the reaction at the WE. [12], [13]

Electrochemical reactions are heterogeneous because they occur at the electrode surface, where electrons are transferred between the electrode and chemical species in the solution. Generally, the rates of heterogeneous reactions depend on mass transfer (which is the diffusion of reactants from the bulk to the electrode surface) and surface effects (e.g. adsorption). Moreover, for heterogeneous reactions, it is useful to express the reaction rate per unit area ($\text{mol} \cdot \text{s}^{-1} \cdot \text{cm}^{-2}$) because the size of the electrode surface affects the rate of electron transfer. The reaction rate per unit area, v, can be written as follows [12], [13]:

$$v = \frac{i}{nFA} = \frac{j}{nF} \tag{2.5}$$

where v is the reaction rate per unit area, i is the total current, A is the electrode surface area, $j = \frac{i}{A}$ is the current density (current per unit area), n is no. of transferred electrons per reactant, and F is Faradays constant. [12], [13]

2.1.2 Electrochemical Techniques: CV, EIS, & CA

Various electroanalytical methods have been developed to qualitatively and quantitatively analyse target molecules by measuring electrical and electrochemical parameters on electrochemical biosensors. Among the techniques used to detect electroactive species, voltammetry, amperometry, impedimetry, and potentiometry are the most common. In this project, however, the focus will be on voltammetry (section 2.1.2), impedimetry (section 2.1.2), and amperometry (section 2.1.2). In these methods, a target analyte binds a recognition element immobilised on an electrode surface, where the electrode surface functions as the transducer (or conversion component). The detected signals are typically based on potential or current. All three techniques will be discussed in further detail in the following next sections.

Cyclic Voltammetry

Cyclic voltammetry is a highly effective and widely employed electrochemical technique for investigating the redox behaviour of molecular species. It serves as a valuable tool for quantifying biological and biochemical processes across various industries, including medical, pharmaceutical, biological, biotechnological, and biosensor development. The technique operates by perturbing an electrochemical system through the linear cycling of potential over a defined range while measuring the corresponding current response of a redox-active solution. [14], [18]

A conventional experimental setup usually involves a three-electrode system. The process begins by preparing an electrochemical cell containing an electrolyte solution and immersing the three electrodes in the solution. A potentiostat is then used to sweep the potential between the WE and RE at a fixed rate, causing redox reactions to occur at the WE surface. When the externally applied potential reaches a fixed limit, the sweep direction is reversed. This allows for both the oxidation and reduction reactions to be observed in a single scan. [14], [18]

The potentiostat records the current flowing between the WE and CE as the potential changes. This data is then plotted as current versus potential, generating a characteristic duck-shaped cyclic voltammogram. The waveform of the externally applied potential and its resulting I vs. E plot are shown in Figure 2.2. The waveform plot shows a system initially in equilibrium. At time $t = 0$ a potential is then swept between two fixed values: V_1 and V_2. That is, the potential is first increased to V_1. Next, the potential is gradually increased in the positive direction towards V_2. As it reaches V_2, the scan is reversed and the potential goes in the negative direction towards V_1. The cyclic voltammogram often exhibits a duck-shaped curve, with peaks corresponding to oxidation and reduction processes, as shown in Figure 2.2b. The position, height, and shape of these peaks provide crucial insights into reaction kinetics, diffusion-controlled processes, and the thermodynamics of the analyte. Initially, during the forward scan, the potential is not strong enough to oxidise the analytes on the

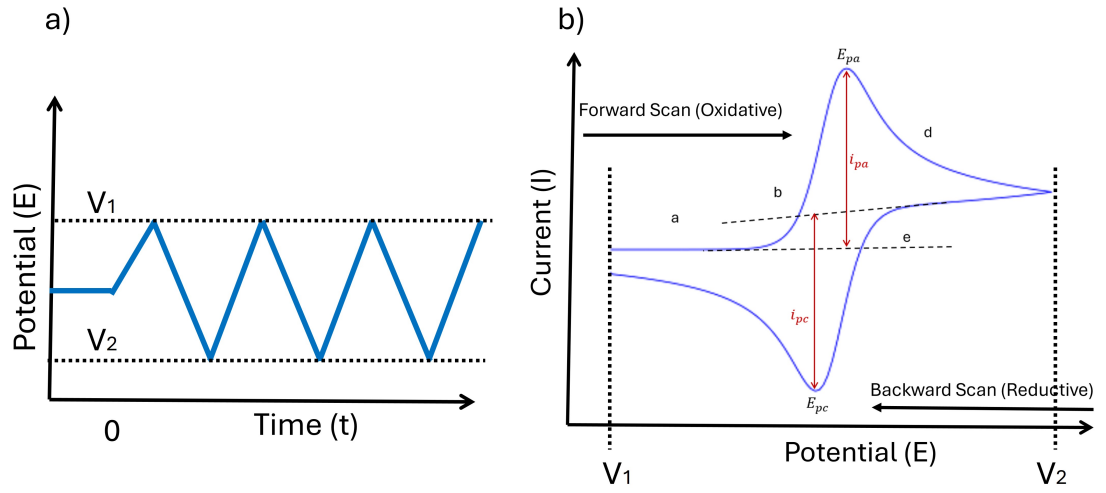

Figure 2.2: Characteristic Cyclic Voltammogra and Its Corresponding Potential Waveform. a) Waveform of applied cyclic potential and **b)** basics of a cyclic voltammogram. V_1 and V_2: potential sweep, i_{pc}: cathodic peak current, i_{pa}: anodic peak current, E_{pa}: anodic potential peak, E_{pc}: cathodic potential peak, a: capacitive region, b: potential onset, d: current decrease, e: reverse scan.

electrode surface (a). As the potential increases, it reaches the onset of oxidation and causes the current to increase exponentially as the analytes are oxidised (b). Slowly, as the scan continues, the amount of oxidant is depleted and the current culminates in an anodic peak current (i_{pa}) for oxidation at the anodic peak potential (E_{pa}). After reaching this point, the current is restricted to diffusion (mass transport) of analytes from longer distances to the electrode surface, which results in a decrease in current and eventually reaching a steady state at maximum positive potential (d). Thus, the backward scan is initiated. Here, the potential is scanned in the negative direction, causing the oxidised species to undergo reduction at the electrode surface. The current initially remains small, as the concentration of oxidised species is still high at the electrode surface (e). As the potential becomes more negative, the cathodic current increases due to more electrons being transferred from the electrode to the electrolytes. Eventually, the cathodic current reaches a cathodic current peak (i_{pc}), which corresponds to the potential at which the reduction rate is at its maximum (E_{pc}). Gradually, the concentration of oxidised species decreases due to continuous reduction, and eventually reaching a steady state where no significant redox activity occurs. [12], [14], [18]

As the potential is swept, electroactive species undergo oxidation and reduction at specific potentials, leading to characteristic peaks in the current response. The potential at which these redox reactions occur is governed by the Nernst equation, which relates the applied potential to the standard reduction potential (E^0) of the species and the concentrations of the oxidised and reduced forms at equilibrium. The Nernst equation is expressed as [14]:

$$E = E^0 + \frac{RT}{nF} \ln\left(\frac{[Ox]}{[Red]}\right) \tag{2.6}$$

where E is the applied potential, R is the gas constant, T is the temperature, n is the number of electrons transferred, F is Faraday's constant, and $[Ox]$ and $[Red]$ are the concentrations of the oxidised and reduced species, respectively. [14]

The Nernst equation establishes a direct correlation between the applied potential and the concentration ratio of the oxidised and reduced forms of the electroactive species involved in the electrochemical reaction. When the concentrations of the oxidised and reduced species are equal ($[Ox] = [Red]$), the logarithmic term becomes zero, and the electrode potential E equals the standard potential E^0. This point is referred to as the formal reduction potential and is an important parameter in characterising redox couples. Thus, the Nernst equation provides a way to predict how a system will respond to a change in the concentration of species in solution or a change in the electrode potential. Thus, during a CV measurement, as the potential is swept, the concentration of the species in the solution near the electrode varies over time, following the principles defined by the Nernst equation. [14]

Additionally, the Nernst equation helps explain the position of the redox peaks observed in the voltammogram. As the potential is swept during the experiment, the ratio $\frac{[Ox]}{[Red]}$ changes, leading to variations in the electrode potential. The peak potentials (E_{pa} for oxidation and E_{pc} for reduction) correspond to the potentials at which the concentrations of the oxidised and reduced species are significantly altered due to the redox reaction. For a reversible system, the peak separation (ΔE_p) between the anodic and cathodic peaks is approximately 59 mV at 25°. [14]

The reversibility of a reaction refers to the ability of the redox process to proceed in both the forward and reverse directions with minimal kinetic limitations. For a fully reversible reaction, the peak potentials are independent of the scan rate, and the peak separation remains close to the theoretical value of 59 mV/n. Here, the ratio of the anodic peak current (i_{pa}) to the cathodic peak current (i_{pc}) should be close to one for reversible reaction, meaning that for irreversible reactions, the ratio of i_{pa} to i_{pc} may deviate significantly from 1, reflecting the asymmetry in the oxidation and reduction processes. Electrochemically reversible processes where the electron transfers are fast and the processes follow the Nernst equation, are often called "Nernstian". [14]

Electrochemical Impedance Spectroscopy

EIS is another powerful and versatile electrochemical technique which is widely employed across various electrochemical systems. Due to its high sensitivity and ability to provide detailed kinetic and mechanistic insights, EIS is extensively utilised in fields such as corrosion analysis, semiconductor research, chemical sensing, biosensing, non-invasive diagnostics, and many more. This technique operates by perturbing an electrochemical system at equilibrium or steady state through the application of

either voltage or current; let us assume a sinusoidal potential excitation is applied to an electrochemical cell. The excitation signal is given by:

$$E_t = E_0 \sin(\omega t) \tag{2.7}$$

where E_t is the potential at time t, E_0 is the amplitude of the signal, and ω is the radial frequency. Here, the relationship between the radial frequency (units of radians/second) and frequency f (units in Hz) is given by:

$$\omega = 2\pi f \tag{2.8}$$

The response signal, in the form of a corresponding current or voltage, is then monitored to analyse its behaviour under the applied perturbation. The response signal, in this case, is a current with a shifted phase (ϕ) and a new amplitude (I_0). This signal is given by:

$$I_t = I_0 \sin(\omega t + \phi) \tag{2.9}$$

Then, by utilising Ohm's Law ($R = \frac{E}{I}$), we can express the impedance of the electrochemical system as:

$$Z = \frac{E_t}{I_t} = \frac{E_0 \sin(\omega t)}{I_0 \sin(\omega t + \phi)} = Z_0 \frac{\sin(\omega t)}{\sin(\omega t + \phi)} \tag{2.10}$$

Thus, the impedance is expressed in terms of magnitude Z_0 and phase shift ϕ, as shown by Equation 2.10. By plotting these two against the corresponding frequencies, a Bode plot can be obtained, i.e. log(frequency) vs. $\log|Z|$ (impedance) and log(frequency) vs. phase angle as shown in Figure 2.3b. However, by further utilising Eulers relationship ($e^{j\phi} = \cos\phi + j\sin\phi$), the impedance can be expressed as a complex function with an imaginary part and a real part. That is, the excitation- and response signals become:

$$E_t = E_0 e^{j\omega t} \tag{2.11}$$

$$I_t = I_0 e^{j\omega t - \phi} \tag{2.12}$$

Consequently, the impedance becomes:

$$Z(\omega) = \frac{E}{I} = Z_0 e^{j\phi} = Z_0(\cos(\phi) + j\sin(\phi)) \tag{2.13}$$

The imaginary part of the impedance can then be plotted against the real part, and a Nyquist Plot is achieved (example shown in Figure 2.3a). Lastly, by fitting EIS data to a theoretical electrical circuit, typically the Randles cell model, an equivalent circuit model can be obtained (Figure 2.3c). [19]–[21]

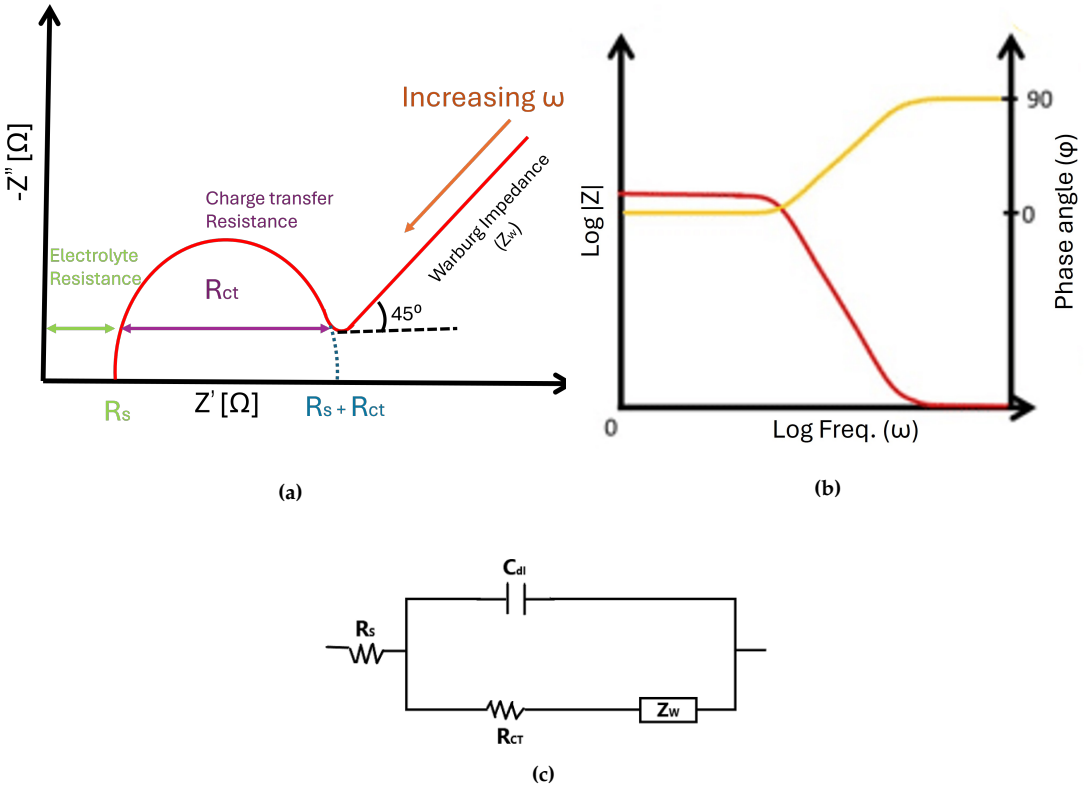

Figure 2.3: The Three Types of EIS Data Representation. a. Nyquist plot, **b.** Bode plot, and **c.** a Typical Equivalent Circuit Model (usually Randals Cell Model).

As already discussed in earlier sections, the electrochemical reaction at an electrode-electrolyte interface can be broken down into a sequence of multi-step processes, including mass transport, charge transfer, double-layer charging (interfacial capacitance C_{dl}), and adsorption, each proceeding at different rates and with a unique impedance response. For example, the mass transport process tends to be slower compared to the charge transfer process, which means their effect is seen at lower frequencies. The advantage of EIS is that it enables the characterisation of these multiple time-dependent processes within a single measurement. That is, by applying a sinusoidal perturbation over a wide range of frequencies, typically 100 kHz to 0.1 Hz, and then measure the responding signals, EIS can distinguish between the individual reaction steps based on their frequency-dependent behaviour. In terms of biosensing, the processes of mass transport and charge transfer are of special interest. These are typically represented via the Nyquist plot, as shown in Figure 2.3a, where the negative imaginary part of impedance, $-Z''$ (capacitive and inductive behaviour), is plotted against the real part of impedance, Z' (resistive behaviour), and each point on the curve corresponds to a specific frequency (i.e. the entire frequency spectrum is compressed into a single

curve). Thus, the curve can be divided into three parts: the electrolyte resistance (R_s), the charge resistance (R_{ct}), and the Warburg impedance (Z_W). [19], [20], [22]

Here, the electrolyte (solution) resistance and charge transfer resistance are in the high-frequency region, while the mass transfer resistance, also known as the Warburg impedance, is in the low-frequency region. The electrolyte resistance is due to 1) the electrolyte conductivity and 2) the distance between the electrodes. In the former, a lower R_S means better ion conductivity in the solution. Conversely, an increased ionic strength (higher salt concentration) reduces R_S. Thus, poor conductivity, i.e. low electrolyte concentration or insulating species, increases R_S. In the latter, it has been shown that shorter separation between electrodes yields smaller ion diffusion lengths and thus lower R_S. [22], [23]

R_{CT} represents the difficulty of electron transfer between the electrode and electrolyte and can be derived from the diameter of the semi-circle; a larger semi-circle means a higher R_{CT}, indicating slower electron transfer, while a smaller semi-circle represents a lower R_{CT}, indicating faster reaction rates (faster electron transfer).

Electrode surface modification, e.g. functionalisation with MUA, SAMs, or polymer layers, increases R_{CT} by blocking electron transfer [24]. Catalysts, e.g. Pt, AuNP, enzymes, decreases R_{CT} by promoting charge transfer [5]. Higher analyte concentration can reduce R_{CT}, facilitating faster redox kinetics.

The Warburg impedance, also known as the diffusion effects, is represented by a linear plot with a 45°slope at lower frequencies. This region is associated with mass transport processes, i.e. diffusion of electroactive species to/from the electrode surface. Increasing solution stirring or convection reduces Z_W. Higher analyte concentration can improve diffusion, reducing Z_W. Thicker diffusion layers, e.g. polymer coatings or biofilms, increase Z_W. [22], [23], [25]

The second intercept with the x-axis at low frequency represents the sum of the electrolyte resistance and charge transfer resistance. This value gives an estimate of the total resistance of the system. If this intercept shifts to a higher Z' value, it indicates total resistance due to passivation layers on the electrode, surface fouling due to adsorption of unwanted species, and lower conductivity of the electrolyte or electrode modifications. [19], [22], [26]

Chronoamperometry

Chronoamperometry is a highly popular and widely used electrochemical technique, as it is primarily used to study electron transfer kinetics (at the electrode-electrolyte), mass transport mechanisms (diffusion), and analyte detection. Similar to EIS, it operates under the principle of faradaic processes, meaning the induced current is directly related to the redox reaction taking place at the electrode surface. However, in contrast to CV and EIS, this technique applies a fixed potential to the electrochemical system and measures the induced current over time. The resulting current, I, can then be plotted against the time, t, thus obtaining an I-t plot as shown in Figure 2.4b. [12], [13]

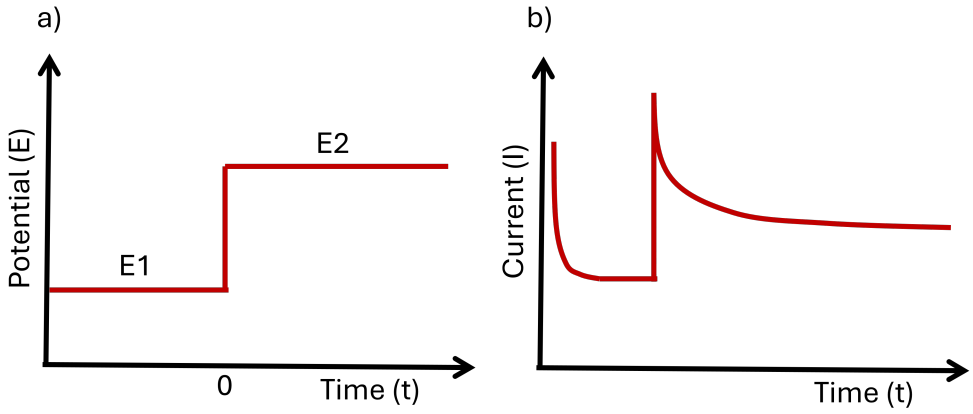

Figure 2.4: Chronoampeometry. a) Waveform of applied potential and **b)** expected I-t profile. The jump in the current is due to the application of E2.

Initially, at the beginning of a CA experiment, the WE is held at a fixed potential (E1). The waveform is shown in Figure 2.4a. In this phase, no oxidation or reduction of the analytes of interest can occur. Subsequently, the potential at the WE surface is stepped such that oxidation/reduction of the analyte can occur (E2). If we translate this process into an I-t plot, a large current peak can be seen right at the beginning. This is when E1 is applied, causing a sudden rise in non-faradaic charging current and is effectively the background current during the measurements. This, in turn, means that there is always a non-zero baseline response, which can have a significant influence on the faradaic measurements. In other words, when a voltage is applied, a very high initial charging current is observed. Suppose the electrode's surface starts with no charge, and the potential is suddenly shifted to a positive charge. In response, cations near the electrode surface migrate away from the positively charged electrode, while anions move toward it. This ion migration continues until the positive charge on the electrode surface is balanced by the negative charge in the electrolyte solution. Since the movement of ions and electrons cannot be distinguished, this process generates a brief, non-faradaic current known as the charging current.

In the next step, when the potential is stepped to E2, and effectively oxidising/reducing the analytes, the resultant faradaic current increases immediately. This is the second peak in Figure 2.4. From this point forward, the current gradually decreases with increasing time, as the molecules diffuse away from the electrode surface. This current behaviour can be described by the Cottrell equation [12], [13], [27]:

$$I(t) = \frac{nFAC\sqrt{D}}{\sqrt{\pi t}} \tag{2.14}$$

where n is the number of electrons transferred, F is Faraday's constant (the total

electric charge carried by one mole of electrons, $F = 9.6485 \times 10^4 C \cdot mol^{-1}$ OR $F = 96.485 C \cdot mol^{-1}$ [28]), A is the area of the electrode, C is the initial concentration of the analyte, D is the diffusion coefficient of the analyte, and t is time after the potential step. This equation (Equation 2.14), however, only applies to large electrodes, where semi-infinite linear diffusion on a planar surface is assumed. In small electrodes (e.g. ultramicroelectrodes (UME) and microelectrodes (ME)), however, the diffusion is more radial (hemispherical diffusion) due to their small surface area and their geometry. In the case of microelectrodes, for example, the diffusion, and thus the current, is affected by the geometry and size of the electrode as is illustrated in Figure 2.5. For a disc-shaped electrode, the steady-state current then becomes [12], [13], [27]:

$$I(t) = 4nFCDr \tag{2.15}$$

where r is the radius of the disc-shaped electrode. Hence, for large electrodes, the current response predominantly follows Cottrell behaviour, gradually decreasing over time and asymptotically approaching zero (Cottrell decay). In contrast, for small electrodes, the current eventually stabilises and reaches a steady-state plateau for long time scales (steady-state current). Moreover, by plotting the current as a function of the square root of time ($t^{-1/2}$), the diffusion coefficient D and the concentration C can be determined from the slope and intercept of the resulting linear relationship. [12], [13], [27]

In a 2012 study by Giraud et al. [27], this approach was utilised to determine the diffusion coefficient and various concentrations of Silicomolybdic complex in oceanic samples. The group performed CA successively on gold disk ME of millimetric size and gold disk UME of micrometric size, both in the presence of Ferrocyanide. They found that, for very short times, both electrodes (ME and UME) followed the Cottrell behaviour. At relatively longer experimental times, however, the current gradually reached a steady state described by [27]:

$$I_{ME} = \frac{nFA_{ME}C_0D_0}{\sqrt{\pi t_{ME} D_0}} \tag{2.16}$$

$$I_{UME} = 4nFD_0C_0r_{UME} \tag{2.17}$$

The group then plotted I vs $t^{-1/2}$, where the slope and intercept were used to determine all D_0 and C_0 of Silicomolybdic. This was done by first combining Equation 2.16 (where $A_{ME} = \pi r_{ME}^2$) and Equation 2.17 to get D_0 [27]:

$$D_0 = \frac{\pi}{16 t_{ME}} \left(\frac{I_{UME} r_{ME}^2}{I_{ME} r_{UME}} \right)^2 \tag{2.18}$$

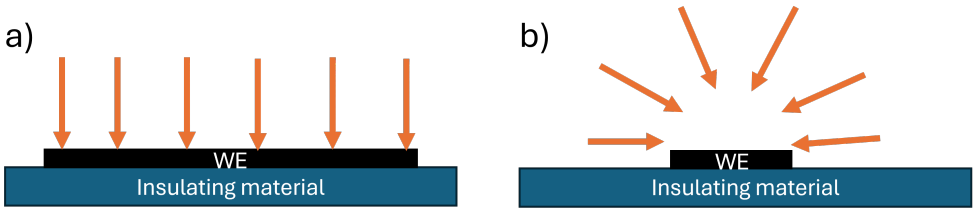

Figure 2.5: Representation of Diffusion Lines Arriving at the Working Electrode surface. Left: planar linear surface, **Right:** hemispherical (radial) surface.

Subsequently, knowing D_0, C_0 was determined by using Equation 2.17. [27]

To summarise, electrochemical techniques provide a fundamental toolkit for investigating and controlling electron transfer processes at the electrode interface. CV enables the characterization of redox-active species by monitoring current responses as the potential is cycled. EIS offers insight into system kinetics and interfacial properties by measuring frequency-dependent impedance, making it particularly useful for assessing charge transfer resistance and diffusion behavior. CA provides valuable information on mass transport and reaction kinetics by applying a sudden potential step and recording the resulting current decay. Together, these techniques allow for precise characterisation and optimisation of electrochemical systems. [12]–[14]

Beyond fundamental studies, these methods are instrumental in biosensing applications, where the detection of biomolecules relies on controlled electrochemical reactions [3], [4], [18]. The next section will delve into biosensors, exploring their design, operational principles, and functionalisation strategies, with a particular emphasis on how electrochemical techniques enhance their sensitivity and specificity.

2.2 Biosensors

Biosensors are devices that integrate a biological element with a physicochemical detector to detect specific substances, providing valuable information in a variety of applications. These devices work by recognising a target analyte, such as proteins, nucleic acids, or small molecules, using a bioreceptor (e.g. an enzyme, antibody, or nucleic acids (DNA or RNA)). The interaction between the bioreceptor and the analyte generates a signal, which is then converted into a readable output, such as an electrical or optical signal. Biosensors are widely utilised in medical diagnostics, environmental monitoring, food safety, and biotechnology due to their ability to offer rapid, specific, and sensitive detection. With advances in nanobiotechnology and materials science, modern biosensors are increasingly sophisticated, offering enhanced sensitivity, portability, and multi-analyte detection capabilities. [29], [30] Among various types of biosensors, electrochemical biosensors are particularly prominent due to their high sensitivity, low cost, and simple detection mechanisms. These biosensors rely on electrochemical transduction, where the biochemical reaction is converted into an electrical signal. Electrochemical biosensors are widely applied in PoC diagnostics, environmental testing, glucose monitoring and many more. [30], [31]

2.2.1 Electrochemical Biosensors

Electrochemical biosensors are analytical devices in which biological receptors interact with electrochemical transducers to analyse samples containing a target analyte. These biosensors generate current, voltage, or impedance due to a biochemical reaction between the recognition element and the analyte. An electrochemical biosensor consists of three main components: a biological recognition element, a transducer (electrode), and a signal processing unit. The recognition element makes direct contact with the analyte to enhance detection. The transducer then converts the biochemical signal into an electrical signal, which is subsequently filtered, amplified, and displayed by the signal processor as a quantitative or qualitative measure of the analyte concentration. [30]–[32] A conventional electrochemical cell in a laboratory is shown in Figure 2.6 and Figure 2.7a.

However, with the invention and development of screen-printing technologies, a more advantageous alternative has been developed and implemented in many fields, namely screen-printed electrodes (SPE). An illustration of this can be seen in Figure 2.7. In this setup, the conventional electrochemical cell is miniaturised into a three-electrode system, where the electrodes (made of conductive ink) are printed onto an insulating, planar material with a reduced substrate surface area. These electrochemical SPE sensors have numerous advantages: portability, simplicity, ease of (mass)production, low cost, consistent performance, low power requirements, low analyte/reagent consumption, and quick response. [30]–[33] There are various commercial SPEs available on the market from multiple manufacturers such as MetrOhm

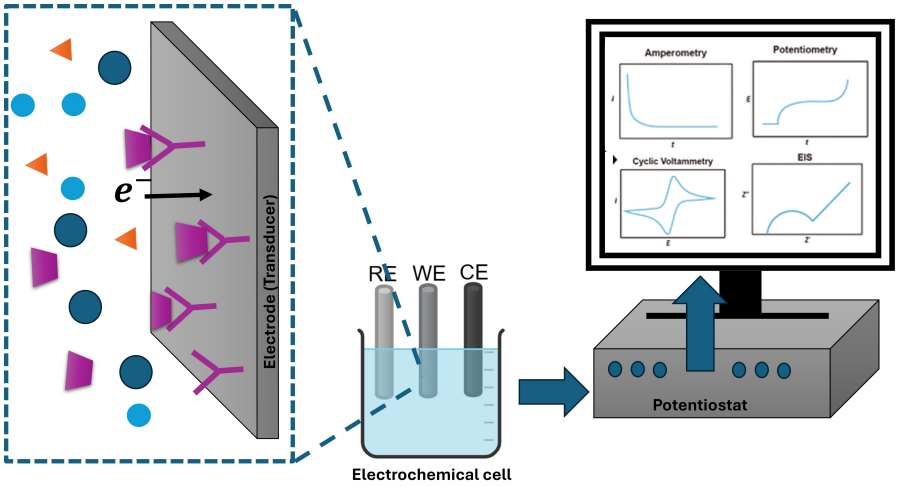

Figure 2.6: A Conventional Electrochemical Biosensor Setup. This system includes a functionalised electrode (transducer) interacting with analyte molecules in solution, generating an electrochemical signal. The electrode system comprises a working electrode (WE), a reference electrode (RE), and a counter electrode (CE) immersed in an electrolytic solution (electrochemical cell). The electrochemical signal is recorded and analysed using a potentiostat, which displays the data via techniques such as amperometry, potentiometry, voltammetry, and impedimetry.

DropSens [34], Zimmer and Peacock [35] and PalmSens [36], to name a few. Additionally, with the help of screen-printing machines, SPEs can also easily be custom-made according to the desired outcome [37]–[39].

2.2.2 Electrochemical Immunosensors

Immunosensors are based on the highly specific interaction between an antibody and its antigen, enabling the detection and quantification of biomarkers or analytes with high sensitivity and selectivity. Most commonly, the sandwich immunoassay technique is used. The Sandwich Enzyme-Linked ImmunoSorbent Assay (ELISA) technique relies on the sandwich immunoassay configuration and refers to the use of two antibodies and an enzyme label (e.g. Horseradish peroxidase (HRP)). Here, the target analyte is sandwiched between surface-immobilised capture antibodies (primary antibody) and enzyme-linked detection antibodies (secondary antibody). Typically, ELISA is the method of choice for accurate and reproducible detection and quantification of biomarkers as it offers high sensitivity and specificity for a wide range of applications, including clinical diagnostics and research. Despite its many advantages, ELISA can also be limited by its time-consuming protocols, high cost, and impracticality for outside laboratory settings. These drawbacks underscore the value of integrating electrochemical methods with the sandwich immunoassay technique, adapting ELISA's principles into biosensor platforms that preserve sensitivity and specificity while being time-efficient, cost-effective, and easy-to-use for PoC diagnostics. These types

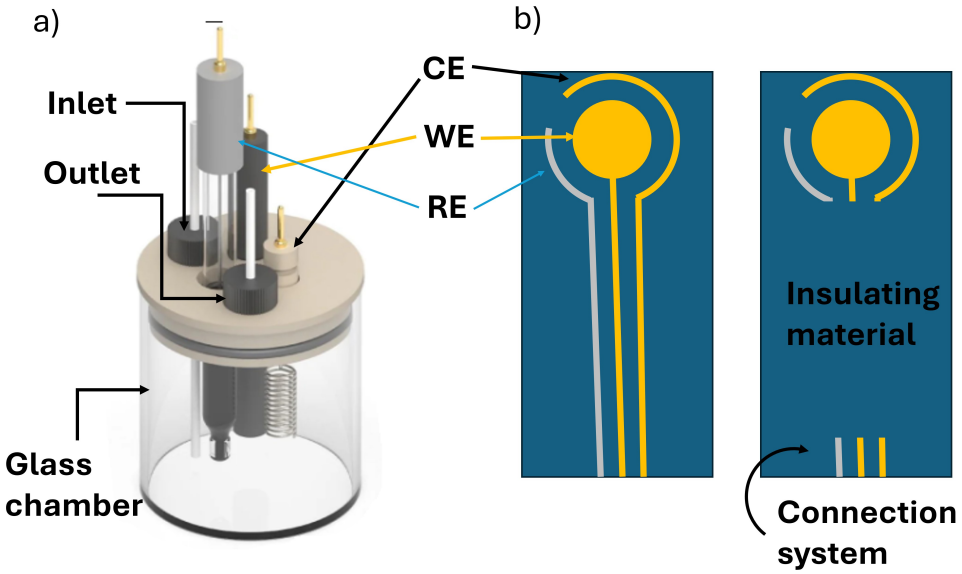

Figure 2.7: A Conventional Electrochemical Cell Setup and A Screen-Printed Electrode. Both setups rely on a three-electrode system: WE, CE, and RE. **a)** Conventional electrochemical cell with a glass chamber, separate WE, RE, and CE, designed for laboratory use and solution exchange. Image from PalmSens Website [40]. **b)** Miniaturised SPE integrating WE, RE, and CE on a single compact substrate, offering portability and ease of use for PoC applications.

of biosensors are also known as immunosensors. [4], [5], [31], [41] Consequently, a plethora of electrochemical immunosensing detection systems have been developed in the past few decades. Electrochemical Immunoassay detection methods commonly utilise one of the following approaches: (1) labelling with a redox enzyme, (2) electrochemical impedance spectroscopy (EIS), (3) nanoparticle labelling, or (4) magnetoimmunosensing. Among these, redox enzyme-labelling and EIS are the most frequently employed techniques in the majority of studies [5], [42]. The first approach employs redox-active enzymes, generating electroactive species that can be detected and quantified through e.g. CV, CA, differential pulse voltammetry (DPV), or amperometry. The HRP enzyme is widely regarded as the standard enzyme label in electrochemical immunosensors due to its robustness, compact size, cost-effectiveness, high catalytic turnover rate, and, notably, its compatibility with a broad spectrum of electroactive species [5], [43]. The second approach works without (enzyme) labels and involves the use of an extra redox probe in an electrolytic solution (e.g. ferri/ferrocyanide [44], [45], ferrocene [46], ubiquinone [47], methylene blue [48], etc.). The outgoing signal is the change in impedance (Z) and the results are represented via the Nyquist plot [45].

In a 2024 study by Huang et al.[41], the sandwich immunoassay method was utilised to develop a PoC electrochemical biosensor for the rapid and selective detection of neurofilament light chain (NEFL) protein and interleukin-6 (IL-6) protein,

where the presence of both can be indicative of neurodegenerative diseases (Parkinson's disease, Alzheimer's disease, Multiple Sclerosis, Huntington's disease, etc.). These biomarkers are present in relatively low concentrations in the human body (pg/mL levels in blood and cerebrospinal fluid), and thus require detection methods with high sensitivity and specificity.

The immunosensor was designed with a double-antibody sandwich configuration on a two-channel electrode using a screen-printed carbon electrode (SPCE) (WE and CE of carbon, RE of Ag/AgCl), enabling the collection of electrochemical biosensing signals through a smartphone. The biosensor setup can be seen in Figure 2.8a. In this design, the capture antibody is immobilised on the electrode surface to specifically bind the target analyte in blood samples. A biotinylated detection antibody then attaches to the captured target analyte, followed by streptavidin-poly-horseradish peroxidase (SA-poly-HRP). The HRP enzyme amplifies the signal, thereby increasing the sensitivity of the biosensor.

The group found that the immunosensor successfully detects NEFL and IL-6 using a redox reaction catalysed by HRP. Moreover, NEFL and IL-6 were detected as low as 5.22 pg/mL and 3.69 pg/mL respectively, outperforming the ELISA method in sensitivity and at a smaller sample volume (6 μL vs. 50 μL). The CV voltammogram showed that, as the analyte concentration increased, the oxidation (anodic) current decreased and the reduction (cathodic) current increased- confirming a successful sandwich structure formation. Similarly, the CA also showed the reduction steady-state current increased with the analyte concentration. This further confirmed that the primary antibodies immobilised on the electrode successfully recognised and bound to the analytes, enabling the subsequent attachment of the HRP-labelled secondary antibodies and thus causing the increase in cathodic current. [41]

The rapid and specific detection of IL-6 was also investigated in an earlier study by Cancelliere et al.[6] (2023), which involved the development of a label-free PoC electrochemical sandwich immunosensor. This study utilised a double-antibody configuration on an SPE, where the secondary antibody was label-free, meaning no enzymes were attached. The experimental setup is illustrated in Figure 2.8b. The assembly of the biosensor was characterised and validated electrochemically, layer-by-layer, using CV and EIS. The CV results demonstrated a reduction in anodic and cathodic peaks as the IL-6 concentration increased, confirming the formation of the sandwich immunoassay configuration. Similarly, EIS exhibited a linear correlation between charge transfer resistance R_{ct} and IL-6 concentration, with an increase in R_{ct} reflecting higher IL-6 levels. The biosensor successfully detected IL-6 with a limit-of-detection (LOD) of 0.78 pg/mL in buffer and 5.4 pg/mL in serum, while the linear detection rate was in the 2-250 pg/mL range. Additionally, the sensor displayed relatively low cross-reactivity ($< 20\%$) and demonstrated a strong correlation with ELISA results, offering comparable accuracy but with significantly shorter detection times.

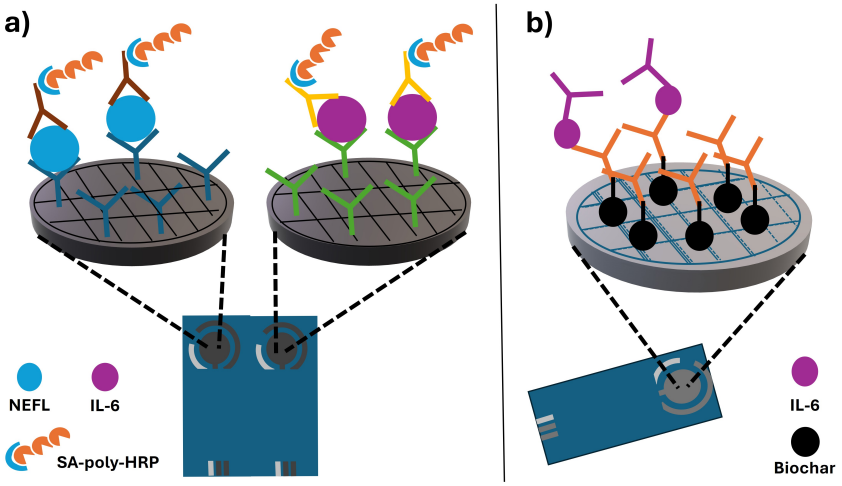

Figure 2.8: Two Distinct Biosensor Setups Using the Sandwich Immunoassay Technique. a) Detection of NEFL (left) and IL-6 (right) on a two-channel SPCE sensor. Primary antibodies are immobilised through non-covalent interactions (hydrophobic interactions). Blocking agent: casein (represented by lattice) [41]. **b)** IL-6 detection using an SPE and label-free secondary antibodies. The primary antibodies were immobilised on biochar (carbonaceous nanomaterial) through covalent interactions (C-N). Blocking agent: PVA (represented by lattice) [6].

2.2.3 Electrode Functionalisation

Electrode functionalisation is the process of altering the structure of an electrode surface to improve its properties and enable specific applications. This modification is brought about by introducing specific functional groups onto the electrode surface which, in turn, leads to optimised electrochemical activity, stability, and selectivity. [2] The functionalisation of each electrochemical biosensor varies greatly, as it depends entirely on the nature of the surface material, bioreceptor/biorecognition element, and the target analyte [3]. Functionalisation can be achieved through two distinct approaches: covalent interactions and non-covalent interactions. The non-covalent approaches include $\pi - \pi$-stacking, electrostatic interactions, Hydrogen (H) bonding, and Van der Waals forces. For instance, researchers have taken advantage of well-known molecular structures such as $\pi - \pi$ stacking interactions and functionalised surfaces with these conjugated structures (e.g. pyrene). In other cases, researchers have used carbon-based nanomaterials such as carbon nanotubes (CNTs) and graphene dispersed on a surface to functionalise the electrode surface through non-covalent interactions. The covalent approach includes the introduction and formation of stable chemical bonds between functional groups (e.g. sulfur groups (-SH), silanes (SiH_4), phosphonates ($CPO(OR)_2$), carboxylic acids (R-COOH), etc.) and the surface material. Another covalent functionalisation approach is the "click chemistry" approach, which relies on an alkyne-azide (AA) formation reaction. [1]–[3] This approach is decsribed further in the next section.

2.3 Click Chemistry

The term "click chemistry" was first introduced in 2001 by Sharpless et al. [49]. The group endeavoured to generate molecules by joining small units with heteroatom links, i.e. C-X-C. The goal was to, ultimately, develop a bolstering group of powerful, highly selective, and modular building blocks that work accurately in both small- and large-scale operations. The basis of this approach was termed "click chemistry" and a strict set of criteria, which a process must satisfy to be applicable in this context, was established; the reaction should be flexible, work with a wide range of substances, give a very high yield, produce harmless by-products which can be easily removed (by non-chromatographic methods), and be stereospecific. Moreover, the process itself should have the following characteristics: simple reaction conditions and (ideally) work well with oxygen and water present, use of easily available materials, no use of solvent (ideally) or use of easily removable solvents (e.g. water), easy isolation of final product and purification-if required-must be done with basic and non-chromatographic methods (such as crystallisation or distillation). Finally, the yield product must be stable under physiological conditions. The group also draws attention to the importance of click reactions having a high thermodynamic driving force (typically >20 $kcalmol^{-1}$) to achieve these required characteristics. [7], [49]

In simpler terms, click reactions are fast, efficient, highly selective, and reliable because they have relatively strong energy "pushing" them forward in a single trajectory. The different types of reactions that are common in click chemistry include I) cycloadditions of unsaturated species (e.g. 1,3-dipolar cycloaddition (Huisgen) reactions and Diels-Alder transformations), II) nucleophilic substitution reactions (e.g. ring-opening reactions of strained heterocyclic electrophiles), III) carbonyl reactions of the non-aldol type, e.g. formation of ureas, thioureas, aromatic heterocycles, etc., and IV) addition reactions to C-C multiple bonds. Among these reactions, the most popular and representative click reaction is the cycloaddition of unsaturated species- more specifically the 1,3-dipolar cycloaddition reaction. This reaction involves the interactions between an azide- and an alkyne group and is highly advantageous in terms of its compatibility with a wide range of pHs, solvents, and temperatures. [7], [49], [50]

2.3.1 Cu(I)-catalysed Azide-Alkyne Cycloaddition Reaction

While click chemistry was initially developed as a tool for organic synthesis [49], this process is now regarded as one of the most effective methods for constructing architectures and adding functionalities to various materials. One of the many state-of-the-art applications of click chemistry is in the biosensor field, namely the immobilisation of biomolecules (e.g. enzymes, antibodies (Ab), and nucleic acids) to different substrates while maintaining their biological function. Not long after developing the click chemistry methodology, researchers incorporated catalysts into the reaction process.

The most representative cycloaddition reaction is the Cu(I)-catalysed azide-alkyne cycloaddition (CuAAC) reaction, the reaction rate of which is 10^7 higher than the non-catalysed reactions and can take place at room temperature. [7], [50] Here, the incorporation of the Cu(I)-species can be carried out via three different routes: I) the direct addition of Cu(I) salts (e.g. chloride (CuCl), iodide (CuI), acetate (CH_3COOCu)) to the reaction medium, II) *in situ* generation by reaction of Cu(II) salts (e.g. sulfate (CuSO_4) or acetate (CH_3COOCu)) with reducing agents, and III) electrochemical Cu(I) generation [50], [51]. The first two are referred to as the "traditional click chemistry" approach and here the Cu(I) species are chemically synthesised. The third one is known as the "electroclick chemistry" approach, where the Cu(I) species are generated electrochemically via an applied potential. Both approaches are used extensively, while the electroclick approach provides a slightly more stable chemical environment. Additionally, the electroclick approach provides precise control over Cu(I) production and offers several other advantages such as environmental compatibility, rapid reaction kinetics, lack of chemical residues [51], [52], and ideal for the functionalisation of multielectrode surfaces without the risk of cross-contamination [7], [52].

The CuAAC reaction was first introduced by Meldal et al. [53] in 2001 and is based on the 1,3-dipolar Huisgen cycloaddition. In this reaction, Cu(I) acetylides reacts with azides and nitrile oxides, resulting in 1,4-disubstituted 2,3-triazoles and 3,4-disubstituted isoxazoles. The Cu(I)-catalysed reaction mechanism is shown in Figure 2.9. The reaction starts by adding Cu(I) species to a solution of alkynes, a), yielding the acetylide complex in the first step. Next, another Cu(I) species is added to the complex, forming a dicopper complex. In the third step, the dicopper complex undergoes two distinct reactions; in the first part, the azide, b), is added. This yields the first C-N bond. The second part of the third step is initiated by the formation of the six-membered ring, which subsequently forms the intramolecular C-N bond by "pushing" out a Cu(I) species. This leads to the formation of the unstable triazolyl-Cu(I) intermediate in the fourth step. Finally, a proton transfer from the alkyne to the triazolyl ligand leads to the release of the second Cu(I) species and the 1,4-triazole product c). [53]–[55]

2.3.2 Electrochemical Platforms: Electrode Functionalisation Using Various Electrode Materials

To ensure high performance, reproducible results, and highly selective and sensitive electrochemical responses, meticulous electrode preparation and functionalisation is vital. That is, the surface of the electrode must be able to support the stable immobilisation of the biorecognition element. Over the past few decades, the CuAAC method has been used extensively as a tool for the proper preparation and functionalisation of different electrode materials. [7], [52] A popular strategy for electrode preparation and subsequent functionalisation is electrografting followed by CuAAC modification [7],

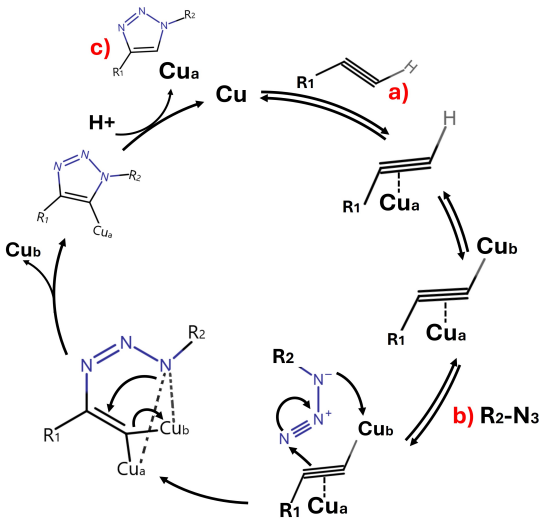

Figure 2.9: CuAAC Reaction Mechanism. a) alkyne, b) azide, and c) alkyne-azide product. Inspired from Pineda-Castañeda et al. [55].

[52], as described in the study by Nxele et al. [56]; here, glassy carbon electrodes (GCE) were functionalised by grafting the electrode surface with terminal azide groups, followed by the recognition and binding of alkynyl tetra-substituted phthalocyanine in the presence of Cu(I). The functionalised electrodes exhibited good electrocatalytic activity specific towards hydrazine (test analyte), with a sensitivity of 15.38 $\mu A \cdot mM^{-1}$ and a LOD of 1.09 μM. A schematic representation of this setup can be seen in Figure 2.10a. Another very common electrode material preparation and functionalisation strategy using CuAAC is the formation of a Self-Assembled Monolayer (SAM) on the electrode surface. More specifically, the formation of alkanethiol SAMs on Au surfaces as a prior functionalisation step before the cycloaddition reaction [7], [52]. In 2004, Collman et al. [57] reported the first use of CuAAC chemistry in combination with SAM to modify well-defined electrode surfaces (as the method was previously used to functionalise polymers). A SAM of azidoundecanethiol ($N_3(CH_2)_{11}SH$)- and decanethiol ($(CH_2)_{10}SH$)- molecules were immobilised on a Au surface, followed by the addition of propynone ferrocene ($FcCOCCH$). The reaction between the SAM of azidoundecanethiols and ferrocene alkanes were catalysed by Cu(II) species. The setup can be seen in Figure 2.10b. The development of this field is constantly evolving, and in recent years SAM/CuAAC-based biosensors have been coupled with alkyne/azide-modified gold nanoparticles (AuNPs) in the presence of Cu-species [7].

Carbon nanomaterials (CNM), such as graphene and carbon nanotubes (CNT), have also been widely used as electrode materials due to their advantageous electrical, chemical, and mechanical properties. Graphene (sheets) and CNTs have large surface areas, possess tunable bandgaps, and offer high mechanical strength, thermal con-

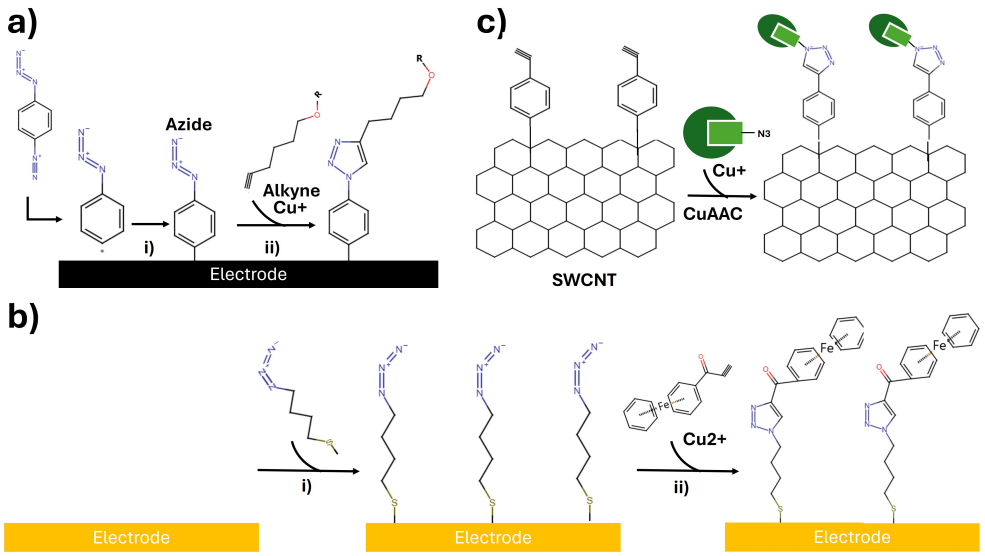

Figure 2.10: Electrode Functionalisation Through Different Azide-Alkyne Modification Strategies. a) Electrografting (i)+ CuAAC reaction (ii). **b)** SAM formation (i) + CuAAC (ii), **c)** SWCNT (i) + CuAAC reaction (ii). Inspired from Nxele et al. [56] **(a**, Collman et al. [57] **(b)**, and Onoda et al. [58] **(c)**.

ductivity, and electrical conductance. Additionally, they are cheaper to produce and have longer lifetimes. These carbon nanomaterials in combination with click chemistry have been demonstrated to successfully produce functionalised electrodes for biosensing purposes. [7], [59], [60] One such study was conducted by Onoda et al. [58], in which CuAAC was utilised to covalently link redox-active cytochrome b_{562} molecules (tethered with an azide group) to acetylene groups immobilised on the surface of single-walled CNTs (SWCNT). This is shown in Figure 2.10c. Thus, the group demonstrated that the functionalisation of CNTs via CuAAC has great potential for designing customised biosensing electrode interfaces. In a study by Seifati et al. [61], an electrochemical biosensor platform was developed by utilising CuAAC in combination with reduced graphene oxide (rGO) and AuNPs on SPCEs. The aim was to detect phenylketonuria (PKU)-associated DNA mutations in newborns. The biosensor exhibited great sensitivity with a LOD of 21.3 fM and a linear detection range of 80-1200 fM. Moreover, the biosensor demonstrated outstanding selectivity and specificity, effectively distinguishing between single-stranded DNA (ssDNA) and target hybridised double-stranded DNA (dsDNA). The group credited the biosensor's exceptional performance to the incorporation of rGO and AuNPs, known for their high conductivity, rapid electron transfer, and extensive surface area. There exist many more methods for proper electrode preparation and functionalisation, with the three mentioned here being the most common types (i.e. electrografting, SAM formation, and CNMs) [7], [52].

Thus, the electrode surface (usually Au or CNMs) is typically functionalised with

thiolated SAMs, followed by immobilisation of the biorecognition element through the CuAAC technique [7], [62]. However, despite its numerous advantages and growing interest, only a few studies so far have reported the application of the CuAAC technique in developing electrochemical immunosensors [7], [50], [52]. A comprehensive overview of these CuAAC-based electrochemical immunosensors is provided in Table 2.1.

One of the papers in this area was presented by Guerrero et al. [50] in 2019, who developed a CuAAC-based electrochemical immunosensor platform for the detection of Chemokine (C-X-C motif) Ligand 7 (CXCL7), a biomarker associated with rheumatoid arthritis and potentially lung cancer. The disposable immunosensor was prepared by using SPCEs functionalised with azide-modified Multi-walled Carbon Nanotubes (MWCNT), enabling the Cu(I)-catalysed click reaction with alkyne-modified Immunoglobulin G (IgG) Abs and directly followed by immobilisation of anti-CXCL7 Abs. Finally, the sandwich immunoassay technique was employed, where the captured CXCL7 was sandwiched between the surface Abs (SPCE/MWCNT-IgG-anti-CXCL7) and the detection Abs (biotinylated anti-CXCL7 Abs labelled with AP-Strep). The immunosensor successfully demonstrated its ability to detect and quantify CXCL7 from patients with RA, achieving a linear calibration plot between 0.5 pg/mL and 600 pg/mL, and a LOD of 0.1 pg/mL. [50]

Another CuAAC-based electrochemical immunosensor was developed by Guerrero et al. [52] in 2020, for the detection of IL-1β cytokine in saliva (biomarker relevant for monitoring diseases related to inflammation, immune processes, and cancer). The SPCEs were functionalised with Cu(I)-clicked MWCNT-azide-alkyne-IgG conjugates followed by the immobilisation of anti-IL-1β Abs. The electro-click reaction was performed by applying a constant potential (-0.4V Ag) to the SPCE/MWCNT and depositing a solution containing alkynylated IgG and $CuSO_4$ in the span of 300 seconds. Sandwich immunoassay was employed to detect and quantify the analyte, wherein the analyte was sandwiched between the capture Abs (SPCE/MWCNT-IgG-anti-IL-1β Abs) and the detection Abs (biotinylated anti-IL-1β Abs labelled with AP-Strep). The immunosensor achieved a LOD of 5.2 pg/mL and showed a calibration curve with two linear ranges; 10-200 pg/mL and 200-1200 pg/mL, thus outperforming those run with commercial ELISA. [52]

Table 2.1: Electrochemical Immunosensors Utilising the CuAAC Technique. The studies shown in this table are reported for various electrode materials and click strategies.

Group (Year)	Electrode Material	Clicked Materials	Click Strategy	Electrochemical Biosensor	Analyte	Transduction Technique
Qi et al. [63] (2012)	GCE	Alkyne-IgG & Azide-SWCNT	AA reaction + $Cu(II)SO_4$	HRP-anti-IgG & IgG-SWCNT/GCE	IgG	Amperometric
Qi et al. [64] (2013)	GCE	Alkyne-hIgG & Azido-aniline	Electroclick + $Cu(II)SO_4$	HRP-anti-gIgG & anti-hIgG-hIgG-GCE	hIgG	Amperometric
Ge et al. [65] (2013)	Au-PWE	1-azidoundecan-11-thiol, Alkyne-Ab1, Azide-Fe_3O_4@SiO_2, Alkyne-Ab2, Alkyne-HRP	AA reaction + $Cu(II)SO_4$	Ab2/HRP-MSN	Microcystin-LR	DPV
Ge et al. [66] (2014)	SPCE	Azide-MSN & Alkyne-GO & Azide-MSN & Alkyne-Ab2	AA reaction + $Cu(II)SO_4$	GO-MSN-Ab2-CA153 & Ab1-GO/SPCE	CA153	DPV
S. Tirado et al. [67] (2016)	GCE	Azide-MWCNT & Alkyne-IgG	AA reaction + $Cu(II)SO_4$	poly-HRP-Strep & Biotin-anti-TGF & SPCE/MWCNT-IgG-anti-TGF-TGFβ	TGF-1β	Amperometric
Zheng et al. [68] (2018)	GCE	Azide-dsDNA & PA	AA reaction + $Cu(II)SO_4$	Cu-PDA-Ab2-CA242 & PA/Ab1-PEI-GO/GCE	CA242	SWV
Guerrero et al. [50] (2019)	SPCE	Azide-MWCNT & Alkyne-IgG	AA reaction + $Cu(II)SO_4$	poly-HRP-Strep & Biotin-antiCXCL7 & CXCL7-antiCXCL7-IgG-MWCNT/SPCE	CXCL7	Amperometric
Guerrero et al. [52] (2020)	SPCE	Azide-MWCNT & Alkyne-IgG	Electro-click reaction + $Cu(II)SO_4$	SPCE/MWCNT-IgG-anti-IL-1β & Biotin-anti-IL-1β-IL-1β & AP	IL-1β	DPV
Svalova et al. [69] (2020)	SPE	Azide-PVBA & Alkyne-NHS ester	AA reaction + CuNP & $Cu(II)(hfac)_2$	SPE/PVBA-NHS ester-anti-*E. coli*-*E. coli*	*E. coli*	Impedimetric

2.4 COMSOL Modelling

The development and optimisation of biosensors rely not only on experimental validation but also on computational modelling to predict and optimise their performance. While electrochemical and surface functionalisation techniques enable biosensor fabrication, computational simulations provide valuable insights into the underlying physicochemical processes, helping to optimise parameters such as electrode geometry, diffusion dynamics, and electron transfer efficiency. In order to save time and resources, as well as getting a deeper understanding of these complex interactions, numerical modelling tools such as COMSOL Multiphysics® are widely used. These simulations allow researchers to study coupled physical phenomena, such as mass transport, reaction kinetics, and electron transfer, within an electrochemical biosensor system. [8]–[10], [70]

COMSOL Multiphysics® stands out as a premier simulation platform, extensively utilised in both academia and industry. It excels at modelling, analysing, and optimising real-world systems where interconnected physical phenomena play a critical role. By employing FEM, COMSOL Multiphysics® enables engineers, researchers, and scientists to address complex multiphysics problems by converting physical laws into mathematical equations and simulating their interactions within a virtual environment. The software integrates theoretical modelling with experimental validation, facilitating virtual prototyping to minimise costs and speed up innovation. Its capacity to tackle multidisciplinary challenges, from tiny MEMS (micro-electromechanical systems) devices to vast industrial systems, makes it invaluable for addressing contemporary engineering and scientific issues. [71]–[73]

Several modules are available in COMSOL Multiphysics®, categorised according to their application and domain areas. Hence, in order to create models for use in specialised application domains, it is possible to use COMSOL Multiphysics® with any combination of add-on modules to produce more customised models. To select a particular physics interface, the software suggests the study types, such as time-dependent or stationary solvers. Accordingly, the relevant numerical discretisation of the mathematical model, solver sequence, and visualisation are specific to the physics phenomena. It is also possible to combine the physics interfaces to describe a system involving multiple phenomena. [72], [74], [75]

To accurately model real-world applications such as biosensors, it is often necessary to incorporate multiple physics fields. Effectively simulating these models provides a deeper understanding of parameters, such as the diffusion process of the sample droplet, scan rate, rate constant, and geometry of the biosensor impacts the overall performance of the biosensor. Additionally, it clarifies how each functionalisation step or layer influences the CV data output. These insights then enable us to fine-tune and optimise the sensor performance. [72], [74], [75]

In a recent study by Bonaldo et al.[10], the group proposed a multiphysics model

for simulating CV of electrochemical biosensors through COMSOL. The simulation took into account the predominant chemical and electrical processes occurring in a redox couple diluted within an electrolyte solution. The simulation model was based on a geometrical 3D structure which was designed by using geometric primitives and computer-aided design (CAD) operations. The 3D geometric structure included the substrate, the three electrodes (WE, RE, and CE), metal interconnections, contact areas, and an isolation layer. Furthermore, the sample drop was designed as a hemisphere, with a radius of 4 mm and an electrode thickness of 100 μm. Finally, the 3D structure was finely meshed by tetrahedral elements in all the regions of interest, i.e. the sample drop, electrodes, interconnections, and contacts. [10]

The simulation model combined four different COMSOL physics, which include: secondary current distribution (*s-cd*), transport of diluted species (*tds*), electrical currents (*ec*), and electrical circuits (*cir*). Here, the *s-cd* was used to model the potentials and electric currents at the electrode-electrolyte interface and the 3D regions of the solution and electrode. Here, the electrochemical kinetics at the electrode-electrolyte interface are described by the Butler-Volmer equation (Equation 2.23). The *tds* simulated the mass transport, i.e. diffusion, in the electrolyte solution as well as the redox species at the electrode-electrolyte interface. This module implemented the Nernst-Planck equation (Equation 2.20) and was coupled with the *s-cd* physics. The *ec* module was used to simulate the voltage and current distributions at the electrode and the contacts, based on Maxwell's Laws. Finally, the *cir* module was used to model an ideal potentiostat and thus simulate the generation, conditioning, and readout of the electric signals. Following the setup of the 3D geometrical model and its corresponding multiphysics modules, the group calibrated the model by using experimental data obtained from commercial SPE biosensors. Subsequently, validation was performed by comparing it with experimental results under varying conditions, including different concentrations and scan rates. The comparison showed a CV response with differences < 10%, confirming the relatively great agreement between the simulated and experimental values. [10]

In another study by the same authors [9], the group presented a multiphysics model capable of simulating EIS responses from an SPE biosensor functionalised with SAM of 11-mercaptoundecanoic acid (MUA). Once again, a 3D geometrical model was designed with a substrate, electrodes (WE, RE, and CE- each 100 μm thick), metal interconnections, contact areas, an isolation layer, and a sample drop (hemisphere with $r = 4.5$ mm). The same four electrochemistry modules were then used for this simulation model as well: the *s-cd*, *tds*, *ec*, and *cir* modules. In this model, however, the electrochemical response of the MUA-functionalised SPE was taken into account as well. This was done by calculating the exchange current density (i_0), which reflects the electron transfer efficiency altered by MUA, for each MUA concentration by using experimentally obtained R_{ct} values. A more detailed explanation of this process can be found in the study. Following the incorporation and optimisations of the electro-

chemistry modules, the model was calibrated and finally, EIS simulations were run for different concentrations of MUA (1 μM - 100 μM). The simulations were compared to experimental results, and it was found that there were < 7% differences between the simulated R_{ct} values and the experimental. Additionally, the simulated surface coverage deviated by only 2% from the experimental results, indicating the potential reliability of the biosensor simulation model.[9]

In the next two sections, the kinetics behind the modules used in these studies, and in electrochemical biosensor studies in general, will be described briefly.

Electrochemistry Module

The Electrochemistry Module in COMSOL Multiphysics® provides specialised physics for modelling electrochemical cells. It enables detailed simulations of electrode configurations, electrolyte transport, and electrochemical reactions, making it a comprehensive tool for understanding electrochemical behaviour under various conditions. The module includes a variety of functionalities, including chemical species transport, charge balances, and fluid flow, allowing users to simulate electrochemical and electroanalytical processes under different operating conditions and electrode configurations. [72], [74], [75]

One of its strengths is its ability to model current distribution at different levels of complexity. It includes Primary, Secondary, and Tertiary Current Distribution models, as well as the Nernst-Planck equations, making it possible to simulate both simple and advanced electrochemical systems. Additionally, the module integrates with other physics-based simulations, which allows users to study how electrochemical reactions interact with heat transfer, fluid dynamics, and mass transport. Hence, this module is a specialised toolkit for modelling and simulating electrochemical systems, integrating charge transfer reactions, ion transport, and coupled physical phenomena. The Electrochemistry module uses Nernst-Plank equations to simulate ion transport in electrolytes under electric fields, including diffusion, migration, and convection and reaction kinetics to support Butler-Volmer and Tafel equations for Faradaic reactions, as well as equilibrium (Nernst) or non-equilibrium dynamics. This module offers various features, one of which is Electroanalysis. That is, the Electroanalysis (Tertiary Current Distribution (*t-cd*) module is an add-on within the Electrochemistry Module and is used for modelling and simulating electrochemical systems where mass transport, charge transfer, and reaction kinetics contribute to the overall current/potential. It is an interface specifically designed to model electrochemical systems such as CV, amperometry, and EIS. [72], [74], [75]

Kinetics of Electrochemical Reactions

The concentration distribution of redox species in the electrolyte can be described using the continuity equation, expressed as follows [11], [12], [73]:

$$\frac{\partial c_i}{\partial t} = -\nabla \cdot J_i \tag{2.19}$$

where c_i is the concentration of ionic species i (mol/m^3), and J_i is the flux of the ionic species ($mol/m^2 \cdot s$). Here, $\nabla \cdot J_i$ represents the divergence of the flux, describing how species move in and out of a given point in space, and $\frac{\partial c_i}{\partial t}$ accounts for the changes in concentration over time. [11], [12], [73]

The flux can be further defined by the Nernst-Planck equation. The Nernst-Planck equations form a fundamental framework for modelling the transport of charged species (ions) in electrochemical systems, accounting for three primary mechanisms which include diffusion (due to concentration gradient), migration (due to electric fields), and convection (due to fluid motion). The general form of the Nernst-Plank equation for the flux J_i of an ionic species i is expressed as [11], [12], [73]:

$$J_i = -z_i u_i F c_i \nabla \phi - D_i \nabla c_i + c_i v \tag{2.20}$$

where:
J_i = Flux of species i ($mol/m^2 \cdot s$),
D_i = Diffusion coefficient (m^2/s),
∇c_i = Concentration gradient of species i ($mol/m^3 \cdot m$),
z_i = Charge number of species i,
u_i = Ionic mobility of species i ($m^2/V \cdot s$),
F = Farday's constant (C/mol),
R = Universal gas constant $J/mol \cdot K$,
T = Temperature (K),
$\nabla \phi$ = Electrostatic potential gradient (V),
v = Velocity field of the electrolyte (m/s).

In this equation, the first term, $-D_i \nabla c_i$, corresponds to diffusion and follows Ficks' law of diffusion, the second term, $-z_i u_i c_i F \nabla \phi$, describes the electromigration, while the third and last term, $c_i v$, represents the convective transport due to fluid motion. [11], [12], [73]

The first term on the right-hand side of Equation 2.4 is the flux contribution by electromigration due to potential gradient, which accounts for the movement of ionic species under the influence of an electric field established by a potential gradient. [11], [12], [73] In the case where the electrolyte solution is buffered with a supporting electrolyte of high ionic strength such as PBS, and in the absence of a potential gradient from the bulk electrolyte region, electroneutrality holds. Hence, the electromigration term contribution to the overall flux, J, is suppressed. The second term on the right-hand side of Equation 2.4 is the diffusive flux governed by Fick's law of diffusion, which describes the movement of species from a region of high concentration to low

concentration regions. [11], [12], [73] The diffusion speed can be impacted by the scan rate during CV, which results in different forms of voltammograms and electrochemical responses of the biosensor. The last term is the advective flux that accounts for the convection of the ionic species due to the electrolyte fluid flow. [11], [12], [73] In the biosensor, the electrolyte is contained within the hemispherical chamber where fluid motion is absent, hence $v = 0$ and the advective flux becomes negligible.

Based on these assumptions, the transport of species is solely governed by diffusion and Equation 2.4 becomes simplified as [9], [10], [12], [70], [75]:

$$J_i = -D_i \nabla c_i \tag{2.21}$$

This equation only considers diffusion and neglects electromigration and convection. The governing equation for species conservation in the Electroanalysis interface is [9], [10], [12], [70], [75]:

$$\frac{\partial c_i}{\partial t} + \nabla \cdot J_i + v \cdot \nabla c_i = R_i \tag{2.22}$$

where R_i represents the reaction term accounting for the consumption or generation of species at the electrode surface. [9], [10], [12], [70], [75]

The electrochemical reaction kinetics at the metal/solution interface can be described by the Butler-Volmer equation, which is a fundamental electrochemical equation that describes the kinetics of electron transfer reactions occurring at the interface between an electrode and electrolyte solution. The general form of the Bulter-Volmer equation is [9], [10], [12], [70], [75]:

$$i = i_0 \left[c_O \exp\left(\frac{\alpha_a z F \eta}{RT}\right) - c_R \exp\left(\frac{-\alpha_c z F \eta}{RT}\right) \right] \tag{2.23}$$

where:
i = The net current density at the electrode
i_O = The exchange current density at the electrode
α_a = The anodic transfer coefficient
α_c = Cathodic transfer coefficient
c_O = Concentration of the oxidation species
c_R = Concentration of the reduction species
c_R = Concentration of the reduction species
F = Faraday's constant
R = the universal gas constant
T = Temperature
z = Number of electrons transferred
η = The overpotential

Here, the overpotential is defined as the difference between the applied $(E_{appl}$ and (E_{eq}) as follows [9], [10], [12], [70], [75]:

$$\eta = E_{appl} - E_{eq} \tag{2.24}$$

In the Butler-Volmer equation, the first exponential term $\exp\left(\frac{\alpha_a F\eta}{RT}\right)$ represents the oxidation process, where electrons are transferred from the electrolyte to the electrode, while the second exponential term $\exp\left(\frac{-\alpha_c F\eta}{RT}\right)$ represents the reduction process, where electrons are transferred from the electrode to the electrolyte solution. This equation allows for either anodic or cathodic current flow depending on the sign and magnitude of the overpotential η. [9], [10], [12], [70], [75]

Double Layer Capacitance

The Butler-Volmer equation can be used to calculate the magnitude of the current due to electrolysis, known as faradaic current. However, the electrode-electrolyte interface can also generate a capacitive current. This is due to the electrical double layer. The double layer can be conceptually compared to a parallel plate capacitor, as the total charge it holds varies depending on the charge density at the electrode and its potential. Although the formation and behaviour of the double layer are inherently complex and not yet fully understood, a common empirical approach to account for its influence on polarisation curves is to introduce a constant ideal capacitance at the electrode-electrolyte interface. This feature can be included by adding the Double Layer Capacitance node. [12], [75]

The initial current sensed during CV is non-faradaic and hence, mostly attributed to double-layer charging or discharging. This is imposed on the WE as a double-layer capacitance C_{dl} boundary condition defined as:

$$C_{dl} = \frac{\epsilon_r \epsilon_0 A}{d} \tag{2.25}$$

where ϵ_r is the relative permittivity of the solution, ϵ_0 is the vacuum permittivity, A is the geometric area of the electrode (m^2) and d is the electric double layer thickness. The capacitance current (i_{captn}) is related to the double layer capacitance by:

$$i_{captn} = C_{dl}\frac{dE}{dt} \tag{2.26}$$

3 Project Approach

The primary focus of this thesis project is the development and optimisation of a click chemistry-based functionalisation strategy for biosensor applications, alongside with computational modelling. The project is hence divided into two parts:

1. An experimental approach
2. A computational approach

In the experimental part, the aim is to develop and model an electrochemical biosensor that is functionalised using Cu(I)-catalysed click chemistry (CuAAC) for biomarker detection. The functionalisation steps will include a SAM of MUA on gold SPEs, followed by covalent attachment of a click chemistry reagent via EDC/NHS chemistry. Afterwards, the required antibodies and enzymes functionalised with a complimentary click chemistry reagent will be attached to the surface using CuAAC. Consequently, the biosensor will be constructed in a layer by layer with each functionalisation step validated through electrochemical methods, including CV, EIS, and CA. The initial experimental work is based on the previous work of Pedersen et al. [5] (2023). The computational modelling will simulate electrochemical processes using a three-electrode system based on the Metrohm DropSens 220BT screen-printed electrode (SPE), which is also employed experimentally. The model incorporates a Au WE, Au CE, and Ag RE printed on a ceramic substrate. A 3D COMSOL geometry replicates the SPE platform, including the electrode arrangement and electrolyte droplet configuration used during CV. Modelled outcomes will be compared to experimental CV data to assess the model's accuracy in replicating real-world behaviour and validate the functionalisation process.

Both approaches will be briefly outlined in the next two sections.

3.1 Experimental Approach

For the experimental part, various electrochemical biosensor setups will be investigated via three different methods.
Method 1: Au electrode functionalised with MUA and HRP (the simplest setup which

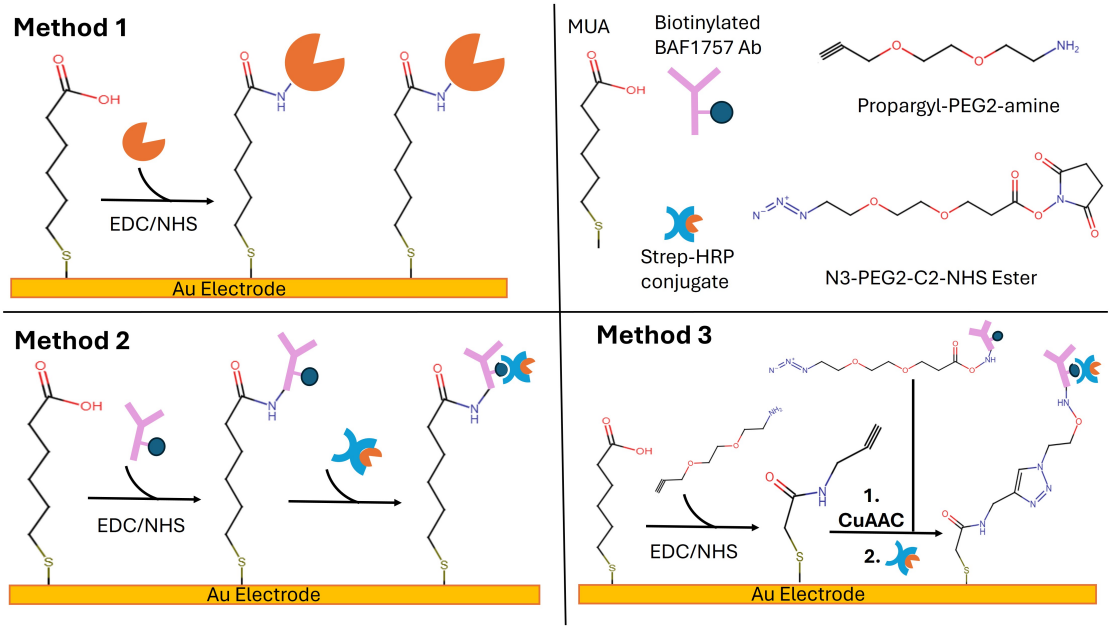

Figure 3.1: Simplified Overview of The Three Experimental Setups of Eectrochemical Immunosensor Platforms and Their Components. All three WEs are covered by a SAM of MUA and activated by EDC/NHS, while the CuAAC technique is only applied in method 3.

lays the foundation for Method 2 & 3). **Method 2:** Au electrode functionalised with MUA and Antibody/HRP-Streptavidin conjugate, and **Method 3:** Au electrode functionalised with MUA and application of the click chemistry technique for efficient and stable immobilisation of the biorecognition element (biotinylated antibody). A simplified overview of the three methods is provided in Figure 3.1.
All experiments employed SPGE (MetrOhm DropSens 220AT) to ensure comparability. An additional objective of this project involve optimising electrode reuse. For this reason, efficient cleaning steps will be developed to restore electrode surfaces, thereby reducing material costs.

Thus, in **Method 1**, the surface of a Au WE is covered with MUA, which binds to the Au surface via its thiol groups. The carboxylic acid group on the other end is activated through EDC/NHS chemistry, allowing for the binding of HRP molecules through their amine groups. Furthermore, the electrochemistry of each layer will be measured; i.e. blank electrode, after MUA layer formation, and once the HRP ligands have been added to the electrode. In **Method 2**, the MUA layer is covered with biotinylated Abs (bio-Abs). Here, an amine group from the bio-Ab will form an amide bond with the carbonyl group from MUA. Once the Abs are bound to the activated MUA layer, Streptavidin-HRP conjugates are added. These conjugates will bind to the Abs through Streptavidin-biotin interactions, which, in turn, will initiate a series of biochemical events on the gold surface. These biochemical events are then recorded,

converted to electrochemical signals by CV, CA, and EIS, and plotted accordingly. In **Method 3**, the click chemistry technique is applied. Here, the click chemicals include an alkyne group (Propargyl-PEG2-Amine), an azide group (N3-PEG2-C2-NHS ester), and a Cu(II)-source to generate Cu(I) ions, in this case $CuSO_4$. Given the novelty of this method within the current laboratory, a new and customised protocol was developed and can be seen in Appendix A. This method can be divided into three main parts: 1) formation of a SAM of MUA and subsequent activation by EDC/NHS, 2) conjugation of MUA & alkyne and bio-Ab & azide respectively, followed by click reaction, and 3) addition of Streptavidin-HRP ligand.

As described in earlier sections, Cu(I) generation can be achieved either *in-situ* or electrochemically. In the former, $CuSO_4$ is chemically reduced by a reducing agent such as sodium ascorbate (NaAsc) or Hydroxylamine ($OH - NH_2$), while the latter uses a fixed potential to reduce $CuSO_4$.

3.2 Computational Approach

The computational approach aims to employ COMSOL Multiphysics® to develop a multiphysics model capable of simulating CV responses for SPEs across sequential functionalisation stages: bare electrodes and functionalised electrodes with SAM, antibody, and enzyme. Inspired by the methodologies of Bonaldo et al. [10] and Franchin et al. [9], the model focuses on replicating experimental CV behaviour for both bare electrodes and functionalised electrodes using the ferri/ferrocyanide redox couple as the electrolyte. The results from each simulation will be compared to the experimentally obtained CV data to assess model's predictive accuracy. The computational workflow for simulating the electrochemical behaviour of the biosensor platform is structured into four interconnected phases, as illustrated in the Figure 3.2, where the computational framework begins with the reconstruction of the Metrohm DropSens 220BT SPE in COMSOL Multiphysics®, translating its physical dimensions into a 3D geometric model. The ceramic substrate $(34 \times 10 \times 0.5$mm is replicated with the electrodes (b). The electrochemical domain of interest centres on the hemispherical electrolyte droplet covering the WE, CE, and RE during measurements. This droplet, containing the ferri/ferrocyanide (in PBS), is discretised to resolve ion transport, electron transfer kinetics, and interfacial phenomena (c). Boundary conditions replicate experimental parameters: a linear voltage sweep (-0.3 V to +0.6 V) is applied to the WE, while the CE and RE are modelled as current sink and reference potential nodes, respectively. Finally, CV curves are generated as the output that capture the redox behaviour as seen in (d).

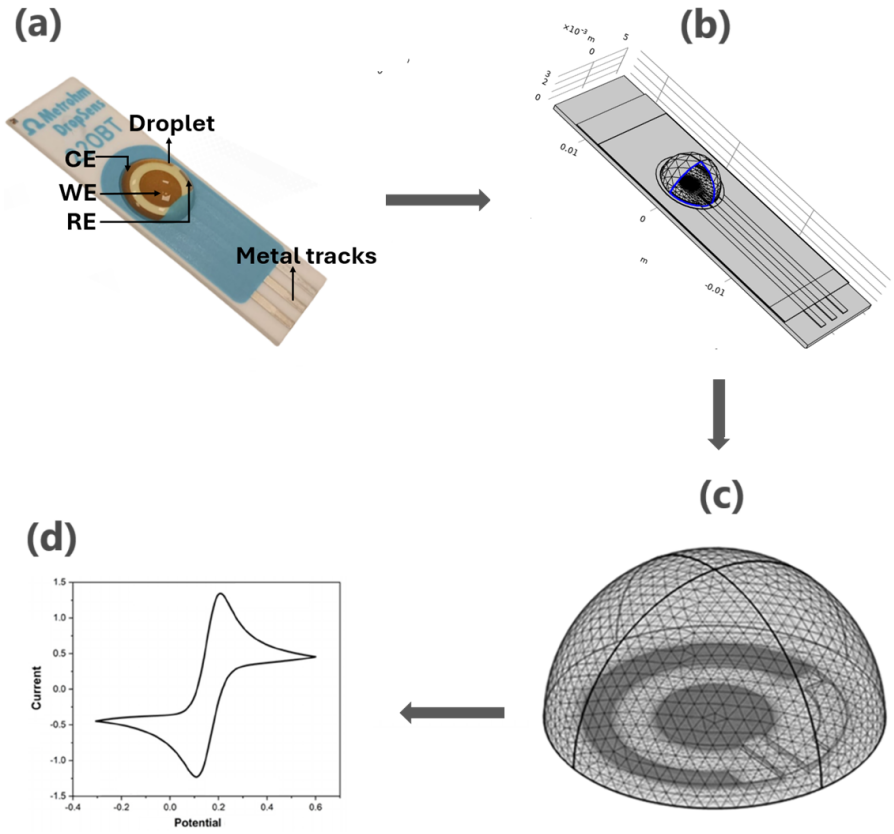

Figure 3.2: Illustration of the Computational workflow for modelling the Metrohm DropSens 220BT biosensor. (a) physical electrode geometry, (b) 3D COMSOL reconstruction, (c) electrochemical domain (electrolyte droplet and electrodes), and (d) simulated CV response.

4 Materials & Methods

4.1 Chemicals, Biologicals, & Equipment

Extensive lists of the devices, biologicals, and chemicals used throughout the project are presented in Table 4.1, Table 4.2, and Table 4.3.

Table 4.1: Devices utilised throughout the project period.

Device	Description	Supplier	Use
Anycubic Wash and Cure	A post-processing device for resin 3D prints	Anycubic	Employed in blocking step of electrodes
Eppendorf Thermomixer Comfort	Simultaneously incubate and shake samples	Eppendorf	For preparation of blocking agent
Potentiostat	Boxed connector for screen-printed electrodes	Metrohm DropSens	Electrochemical cleaning and measurements
Sensit Smart Potentiostat	USB Potentiostat and Impedance analyser for electrochemical sensors	PalmSens	Electrochemical cleaning and measurements
VWR pHenomenal pH 1100L Bench pH Meter	pH meter	VWR Collection	Adjusting pH of NHS/MES sol.

Table 4.2: Biologicals utilised throughout the project period.

Name	Lot No	Supplier	Use
BAM1676 (Ab)	N/A	N/A	Immobilisation Process and detection
Horse radish peroxidase (HRP)	0000358283 (P8375-2KU) Sigma Aldrich	Sigma Aldrich	Immobilisation Process
Streptavidin-HRP A	P272052	R&D Systems™	Immobilisation Process

Table 4.3: Chemicals utilised throughout the project period.

Chemical	Cas No.	Supplier	Use
Aluminum Oxide Powder (0.3 μm)	1344-28-1	Ossila	Mechanical polishing of used electrodes
Copper(II) sulfate hydrate	23254-43-5	Sigma Aldrich	Copper tests
Cystamine	60-23-1	Sigma Aldrich	Electrode surface blocking
Dimethyl sulfoxide (DMSO)	67-68-5	Sigma Aldrich	Copper tests
Ethanol absolute	64-17-5	VWR Chemicals	Electrode cleaning and MUA Solution
Hydroxylamine	N/A	In-house	Quenching
2-Hydroxy-4′ -(2-hydroxyethoxy)-2-methylpropiophenone (Irgacure)	106797-53-9	Sigma Aldrich	Blocking agent

Table 4.3 continued from previous page...

11-mercaptoundecanoic acid	71310-21-9	Sigma Aldrich	SAM of MUA
MES Monohydrate	145224-94-8	MedChem-Express	MES Buffer Solution
N-(3-Dimethylaminopropyl) -N′-ethylcarbodiimide hydrochloride (EDC)	25952-53-8	Sigma aldrich	EDC/NHS Chemistry
N-Hydroxysuccinimde	6066-82-6	Sigma Aldrich	EDC/NHS Chemistry
N3-PEG2-C2-NHS ester (Azide)	1312309-64-0	MedChem-Express	Click Chemistry reaction
PBS (pH = 7.3)	N/A	In-house	Buffer
Poly(ethylene glycol) (PEGDA) diacrylate	25570-48-9	Sigma Aldrich	Blocking agent
Potassium Ferricyanide ($K_3[Fe(CN)_6]$)	13746-66-2	Sigma Aldrich	Ferri/Ferro-cyanide Solution
Potassium Hexacyanoferrate(II) trihydrate ($K_4[Fe(CN)_6] \cdot H_2O$)	14459-95-1	Sigma Aldrich	Ferri/Ferro-cyanide Solution
Propargyl-PEG2-amine (Alkyne)	944561-44-8	MedChem-Express	Click Chemistry reaction
Sodium chloride	7647-14-5	VWR Chemicals	Copper tests
Sodium hydroxide	1310-73-2	Sigma Aldrich	pH adjusting of MES buffer
Sulfuric acid (50 mM H_2SO_4)	N/A	In-house	Electrode Cleaning (Step 2)
1-Step™Turbo TMB-ELISA	(Lot No: WQ332035)	Thermo Scientific	CA measure-ments

4.2 Experimental Methods

This section describes all the settings and methods used to achieve the results for the characterisation, detection, and measurement of each step involved in the three experimental approaches for developing a biosensor. It outlines the parameters, procedures, and techniques applied, as well as how each step was performed to produce the results.

4.2.1 Buffers & Solutions

This subsection provides a detailed description of all the solutions and buffers applied during the experimental work.

Ferri/Ferrocyanide Solution

A 3 mM ferri/ferrocyanide solution was freshly prepared prior to use to ensure optimal reactivity. The solution was prepared by mixing potassium ferricyanide $(K_3[Fe(CN)_6], MW = 329.24 g/mol)$ and potassium hexacyanoferrate(II) trihydrate $(K_4[Fe(CN)_6] \cdot 3H_2O, MW = 422.39 g/mol)$ in equimolar concentrations. The salts were dissolved in 150 mM PBS, ensuring thorough mixing until a homogeneous solution was achieved and applied afterwards.

PBS Solution

An in-house PBS solution, at a concentration of 150 mM and adjusted to a pH of 7.3, was employed in all experiments.

EDC/NHS Solution in MES Buffer

In order to activate the SAM of MUA on the electrodes, EDC/NHS chemistry was applied. A stock solution of NHS in MES buffer was prepared and stored to ensure consistency throughout the experimental procedure. A solution of 20 mL of NHS in MES buffer was prepared by dissolving 213.1 mg of MES monohydrate in 15 mL deionised water. The pH was carefully adjusted to 5 (4.970) using 0.1 M NaOH solution. Subsequently, 230.1 mg of NHS was added to the buffer and stirred until it fully dissolved. The solution volume was then adjusted to 20 mL by adding an additional 5 mL of deionised water, followed by thorough mixing to ensure all components were uniformly distributed.

The final NHS solution was aliquoted into Eppendorf tubes, each containing 300 μL , and stored at $-20\,^{\circ}$C to maintain its stability and usability throughout the project period. Before use, the frozen NHS in MES buffer solution was thawed at room temperature until it became liquid again. EDC was then freshly added to the thawed NHS

solution and mixed thoroughly to ensure activation of the reagents. The EDC/NHS solution was immediately applied to the MUA-functionalised electrodes.

Click Chemicals: Alkyne, Azide & $CuSO_4$ Stock Solutions

Alkyne Stock Solution. A 200 mM alkyne stock solution was prepared by dissolving alkyne ($MW = 143.18 g/mol, \rho = 0.992 g/cm^3$) in 200 μL of DMSO. The mixture was shaken using a shaker until the alkyne was completely dissolved.

Azide Stock Solution. A stock solution of azide was prepared by mixing 100 mg of azide ($MW = 300.27 g/mol$) with 100 μL DMSO. The total volume was measured manually using a pipette, yielding approximately 145 μL. The final concentration was determined to be 2.3 M.

$CuSO_4$ **Stock Solution.** A series of preliminary experiments was conducted to identify the optimal $CuSO_4$ solution formulation. The final procedure, which was used in the protocol for Method 3 (protocol can be seen in Appendix A), is outlined here. Details of alternative $CuSO_4$ formulations can be found in section 4.2.5. To prepare a 1 mM $CuSO_4$ solution in 0.5 M NaCl, the required mass of $CuSO_4$ powder was first weighed and then an appropriate volume of 0.5 M NaCl solution was added to the powder. The mixture was stirred thoroughly until complete dissolution was achieved.

MUA Solution

To form a SAM of MUA on the electrodes, a 2 mM solution was prepared using a solvent mixture of 50% absolute ethanol and 50% deionised water. An appropriate amount of MUA powder was dissolved in absolute ethanol to ensure proper solubilisation, as ethanol effectively dissolves hydrophobic compounds. Afterwards, an equal volume of deionised water was added to the ethanol solution. The mixture was thoroughly stirred to achieve a homogeneous solution. This solution was then used to coat the Au electrode surface, facilitating the formation of a MUA layer.

Enzyme Solution

The enzymes applied are the HRP and the streptavidin-conjugated HRP as listed in Table 4.2. The enzymes were applied as dilution series of 1:20, 1:100, and 1:500. The enzymes were diluted with 150 mM PBS.

Antibody Solution

The antibody (BAM1676) was supplied by the supervisor in a stock solution of 5 μL at a concentration of 500 μg/mL. To prepare working solutions, this stock solution

was serially diluted to final concentrations of 20 μg/mL, 10 μg/mL, 5 μg/mL, and 1 μg/mL. Each dilution was performed using 150 mM PBS as the diluent.

Preparation of Blocking Agent Solutions

PEGDA Stock Solution. A solution of 200 μL of 10 % PEGDa ($\rho = 1.12 mg/\mu L$) was prepared by adding 17.9 μL PEGDA to 182.1 μL of PBS and mixed.

Irgacure Stock Solution. A stock solution of 200 μL of 1% Irgacure was prepared by dissolving 2.1 mg of Irgacure in PBS at 40°C for 40 minutes in Thermomixer Comfort machine.

PEGDA-Irgacure Working Solution. From the stock solutions of PEGDA and Irgacure, a 600 μL solution containing 1% PEGDA and 0.05% Irgacure was prepared by adding 510 μL of PBS, 60 μL of 10% PEGDA stock solution, and 30 μL of Irgacure stock and mix them. This solution was then used for blocking the electrode surfaces.

4.2.2 Cleaning of Electrodes

The electrodes were cleaned using both mechanical and electrochemical methods to clean the used electrodes for impurities as much as possible.

Mechanical Cleaning

All electrodes were first mechanically cleaned using the Ossila electrode polishing tool kit (EPK-3) with 0.3 μm grain size alumina polishing powder. A coffee-coloured polishing cloth was securely fixed to a stable surface, and alumina powder was applied to the cloth and moistened with deionised water. The electrodes were polished in an eight-figure motion for two minute two minutes while held vertically and securely, avoiding excessive force to prevent damage to the electrodes. After polishing, the electrodes were thoroughly rinsed with deionised water, dipped in absolute ethanol, and dried with a nitrogen flow.

Electrochemical Cleaning

The electrochemical cleaning process consisted of two steps: Step and Step 2. In Step 1, CA was utilised, while in Step 2, CV was utilised. The settings applied for the CA and CV can be seen in Table 4.4. The software PSTrace v5.10 from PalmSens, which controls the potentiostat and facilitates precise parameters, is applied to conduct the electrochemical measurements. Among the two potentiostats listed in Table 4.1, the Sensit Smart Potentiostat was predominantly used for electrochemical cleaning and measurements throughout the project while the Metrohm DropSens potentiostat was employed only during the initial stages.

Step 1: Cleaning with CA. A droplet of 150 mM PBS was applied to the electrode, ensuring it covered all three electrodes. CA was performed at a constant potential of 1.4 V for 30 seconds. Afterwards, the electrodes were rinsed thoroughly with deionised water and dried using nitrogen flow.

Step 2: Cleaning with CV. The electrodes were further cleaned using CV in a 50 mM Sulfuric acid (H_2SO_4) solution. A droplet of H_2SO_4 was added onto the electrode, ensuring it covered all three electrodes. The CV was run for 10 cycles, sweeping the potential from 1.4 V to -0,1 V at a scan rate of 100 mV/s with a step size of 2 mV. After completion, the electrodes were rinsed with deionised water and dried with nitrogen flow, ready for subsequent experimental use.

Table 4.4: Electrochemical Settings for Cleaning (Step 1-2). The settings for Step 1 cleaning with CA are shown on the right, while the settings for Step 2 cleaning with CV are shown on the left.

CV		CA	
E vertex 1	1.4 V	t eq.	0 s
E vertex 2	-0.1 V	E dc	1.4 V
E Step	0.002 V	t interval	0.1 s
Scan rate	0.1 V/s	t run	30 s
Number of scans	10		

4.2.3 Method 1

After the mechanical and electrochemical cleaning, the electrodes were ready for functionalisation and detection tests. In Method 1, the electrodes were functionalised with a SAM of MUA by exposing the electrodes to MUA solution, as described in section 4.2.1, and left overnight ($\sim$ 18 hours) at $4°C$. To activate the carboxylic acid groups on the SAM, the electrodes were exposed to a freshly prepared 1:2 solution of NHS and EDC in 50 mM MES buffer (pH 5.0) for 40 minutes, followed by thorough rinsing to remove any unreacted reagents. Immediately after, 5μL of enzymes (HRP and Strep-HRP, respectively) were pipetted onto the activated electrode surface and incubated for 1 hour at room temperature. The enzyme solutions (HRP and Strep-HRP) were prepared beforehand. Both were first diluted to the desired concentrations and subsequently applied to their designated electrodes. After 1 hour of incubation, the electrochemical activity of the electrodes was measured through CV, EIS, and CA. Here, for CV and EIS measurements, the redox couple ferri/ferrocyanide (3 mM in PBS) was used. For CA measurements, 1-Step™Turbo TMB-ELISA Substrate Solution was used. The CV, EIS, and CA settings can be found in Table 4.5.

Table 4.5: Electrochemical Settings for Measurements. The electrochemical measurements for Methods 1–3 were conducted using the following settings. The E dc was determined individually for each method based on CV measurements and subsequently applied to the corresponding method. The E dc value of 0.75 V is applied for Method 1, while Edc for Method 2 was 0.125 V

EIS		CV		CA	
t eq.	0 s	E vertex 1	0.6 V	t eq.	0 s
E dc	0.75 V	E vertex 2	-0.3 V	E dc	0.0 V
E ac	0.01 V	E Step	0.002 V	t interval	0.1 s
n freq.	61, 10 points/dec	Scan rate	0.1 v/s	t run	120 s
Max. freq.	100.000 Hz	No. of scans	5		
Min. freq.	0.1 Hz				

4.2.4 Method 2

Method 2 follows the same initial steps as Method 1 (see section 4.2.3), including the mechanical and electrochemical cleaning of electrodes, the formation of a SAM of MUA, and the activation of the SAM using a freshly prepared 1:2 (v/v) solution of NHS and EDC in 50 mM MES buffer.

Here, an additional step is introduced before adding the enzymes. Immediately after EDC/NHS activation, 5 μL of BAM1676 antibodies were added to the electrode surface and left for 1 hour at room temperature. Subsequently, 5 μL of the HRP and Strep-HRP solutions are pipetted onto the electrodes and incubated for 30 minutes at room temperature while covered. Following incubation, unbound material is removed by rinsing with deionised water, and the electrodes were dried under a nitrogen flow, preparing them for the subsequent electrochemical measurements (CV, EIS, and CA). Here, for CV and EIS measurements, the redox couple ferri/ferrocyanide (3 mM in PBS) was used. For CA measurements, 1-Step™Turbo TMB-ELISA Substrate Solution was used. The electrochemical settings applied in this method are the same as for Method 1, however with an E dc value of 0.125 V. The settings are listed in Table 4.5.

4.2.5 Method 3: Click Chemistry

Method 3 introduces a click chemistry approach that necessitated developing a new protocol. Preliminary tests were conducted to optimise parameters and procedures. The initial steps are identical to those in Methods 1 and 2, wherein electrodes are first cleaned mechanically (by polishing) and electrochemically, followed by the formation of a MUA layer and activation with EDC/NHS chemistry. The protocol in its entirety can be seen in Appendix A. The click chemistry procedure comprises the following steps:

Step 1: Conjugation of the Alkyne Layer

A 200 mM stock solution of alkyne was prepared and diluted 10-fold with DMSO to obtain a 20 mM working solution. Next, 5 μL of the 20 mM alkyne solution was added to the EDC/NHS-activated electrodes and incubated for 2 hours at room temperature. Following incubation, the electrodes were thoroughly rinsed with deionised water. At this stage, the blocking step was introduced. Specifically, electrodes intended for testing were subjected to the blocking procedure at this point, prior to the click reaction.

Step 2: Conjugation of the Azide-Antibody

First, the BAM1676 stock solution ($V = 5\mu$L, c=500 μg/mL) was diluted with 45 μL PBS to achieve a final concentration of 50 μg/mL. Next, the azide stock solution (200 mM) was diluted 10-fold to obtain a 20 mM azide working solution. From this 20 mM solution, 5 μL was transferred to 50 μL of the antibody solution, yielding a 55 μL azide-antibody conjugate solution, which was then incubated for 30 minutes at room temperature. Finally, 1 μL of hydroxylamine was added to quench the unreacted NHS ester.

Step 3: Click Reaction

For the click reaction to occur, Cu(I) ions were generated via two approaches. For this, a droplet with a total volume of 35 μL was used. This droplet consists of 30.75 μL of 0.5 M NaCl, 1.25 μL of $CuSO_4$, and 3 μL of azide-antibody conjugates. The order in which the constituents were added, however, was different for the two approaches. The two approaches are outlined in the following:

Approach 1:

1. Apply 32μL of the NaCl and $CuSO_4$ mixture to the electrode.
2. Run CA for 15 minutes at 160 mV.
3. Immediately add 3μL of azide-antibody (except for the control).
4. Incubate the electrode for 2 hours at room temperature.
5. Rinse the electrode with PBS.
6. Apply 5μL of Strep-HRP (diluted 1:20) to the working electrode.
7. Incubate for 30 minutes at room temperature and rinse.
8. Add a droplet of Turbo TMB Solution, and conduct CA with $E_{dc} = 0.0V$, a time interval of 0.1 s, and a total run time of 120 s.

Approach 2:

1. Apply all constituents (NaCl, $CuSO_4$), and azide-antibody) simultaneously to form the 35μL droplet.
2. Run CA for 15 minutes at 160 mV.
3. Incubate the reaction for 2 hours at room temperature.
4. Rinse the electrode with PBS.
5. Apply 5 μL of Strep-HRP (diluted 1:20).
6. Incubate for 30 minutes at room temperature and rinse.
7. Add a droplet of Turbo TMB Solution, and conduct CA under the same settings as in Approach 1.

A control experiment was conducted to evaluate the specificity of Strep-HRP binding to the azide-antibody layer, following Approach 1. In this test, 32 μL of the NaCl and $CuSO_4$ mixture was first applied, and CA was run for 15 minutes at 160 mV. Subsequently, 3 μL of PBS was added and incubated for 2 hours. It was rinsed with deionized water. Then, Strep-HRP (1:20) was added, followed by the TMB-based measurement.

Optimal Concentration and Potential Test for $CuSO_4$

In order to determine the potential at which $CuSO_4$ is reduced from Cu(II) to Cu(I) ions, several tests were run:

Test 1: A 10 mM $CuSO_4$ stock solution was prepared in PBS by dissolving 15.96 mg of $CuSO_4$ powder in 10 mL of PBS. From this stock solution, four dilutions were subsequently prepared according to Table 4.6.

Afterwards, a droplet of 70 μL of each dilution was added to a bare electrode and CV was conducted with the following parameters: a potential range from -0.6 V to 0.8 V, a step size of 0.002 V, a scan rate of 0.1 V/s, and 5 scans. Between each measurement, the electrode was thoroughly rinsed and dried with nitrogen gas. In the next step, the reduction potentials obtained from these CV measurements were used for subsequent CA measurements. Each concentration was subjected to CA for 15 minutes at the reduction potential E dc = -0.4 V, with a sampling interval of 0.1 s, and a total run time of 15 minutes.

Test 2: Test 2 followed the same procedure as described in Test 1, with two key modifications. First, $CuSO_4$ powder was dissolved in PBS containing 10% DMSO, and the solution was subjected to enhanced agitation to improve dissolution. Second, a new

Table 4.6: $CuSO_4$ **Dilutions in PBS. For Optimal Concentration and Potential Determination via CV and CA.** The $CuSO_4$ were taken from the 10 mM stock solution.

Concentration	$CuSO_4$ in PBS
1 μM	Serial Dilution: I) 100 μL of 1 mM 10 μL stock + 90 μL PBS **II) 1 mL of 1 μM** 10 μL of (I) + 990 μL PBS
10 μM	Serial Dilution: I) 1 mL of 1 mM 100 μL stock + 900 μL PBS **II) 1 mL of 10 μM**: 10 μL of (I) + 990 μL PBS
100 μM	10 μL stock + 990 μL PBS
1 mM	100 μL stock + 900 μL PBS
10 mM	Stock solution

electrode was used for each concentration measurement to prevent interference from $CuSO_4$ deposition on the electrode surface, which could lead to inaccurate or unreliable results. Electrochemical measurements were performed using the same CV and CA settings as in Test 1.

Test 3: In Test 3, the CV potential range was adjusted to -0.2 to $0.6V$. Five measurements of $CuSO_4$ with varying concentrations were performed using only PBS on a single electrode. This was repeated on a second electrode but with PBS mixed with 10% DMSO. The reduction potential derived from the CV measurements was subsequently applied for CA.

Test 4: Test 4 evaluated the impact of electrode reuse on signal integrity. All measurements were performed on the same electrode, beginning with control CV and CA tests without $CuSO_4$ (using 0.5 M NaCl and PBS containing 10% 0.5 M NaCl) to assess electrode cleanliness after rinsing with deionised water. Subsequently, two $CuSO_4$ solutions were tested: a 2 mM solution in a medium of 10% 0.5 M NaCl and 90% PBS and, a solution prepared by dissolving $CuSO_4$ in 100% 0.5 M NaCl. All measurements were conducted using the same CV and CA settings as in Test 3.

Test 5: A new series of $CuSO_4$ dilutions in 0.5 M NaCl was prepared. Target concen-

trations were 1 μM, 10 μM, 100 μM, 1 mM, and 2 mM, along with a control containing only 0.5 M NaCl. First, a 2 mM $CuSO_4$ stock solution in 0.5 M NaCl was prepared, from which the dilution series was derived. CV measurements yielded a reduction potential of 0.16 V, which was subsequently applied during CA measurements. The CV and CA settings are provided in Table 4.7.

Table 4.7: Electrochemical Settings for The $CuSO_4$ Tests. The following settings are applied for CV and CA measurements in the $CuSO_4$ test, where the E dc value is extracted from the CV measurements.

CV		CA	
E vertex 1	0.6 V	t eq.	0 s
E vertex 2	-0.2 V	E dc	0.16 V
E Step	0.002 V	t interval	0.1 s
Scan rate	0.1 V/s	t run	900 s
Number of scans	5		

Blocking of Electrode surface Before and After Click Reaction

In Method 3, an additional step was introduced to the electrode functionalisation process: blocking the electrode surface before and after the click reaction. The blocking of the electrode surface was done in the following steps:

1. 70 μL 1 mM Cystamine solution was added onto the electrodes and incubated overnight at 4°C.

2. After the overnight step, electrodes were rinsed with PBS and dried under nitrogen flow.

3. Next, 45 μL of the freshly prepared 1% PEGDA and 0.05% Irgacure solution was applied to the electrodes, which were then exposed to UV light for 2 minutes in an Anycubic Cure & Wash Machine.

4. After UV curing, the electrodes were rinsed with PBS and prepared for the subsequent step.

Blocking of Electrode Surface Before Click reaction: Electrodes were blocked before click reaction step. After addition of Alkyne layer, the electrodes were blocked as described above.

Blocking of Electrode Surface After Click reaction: Electrodes were blocked after click reaction step was performed. The blocking step was performed before adding the Strep-HRP solution to the electrodes.

Blocking of Electrode Surface After Click reaction at varying azide-antibody Concentrations Two sets of experiments were conducted to evaluate the impact of electrode surface blocking immediately after the click reaction, using varying azide-antibody concentrations of 25% (1.04 μg/mL) azide-antibody concentration, 50% (2.083 μg/mL), 100% (4.1666 μg/mL), 200% (8.333 μg/mL), and 400% (16.66 μg/mL). One set included a blocking step, while the other set omitted the blocking step.

4.3 Computational Methods

The electrochemical biosensor platform employed in this project is the 220BT SPE from Metrohm DropSens, which serves as the foundation for both experimental measurements and numerical modelling in COMSOL Multiphysics®. This commercially available electrode is designed with a three-electrode configuration, consisting of a Au WE, a Au CE, and a Ag RE, all printed onto a ceramic substrate. The WE, positioned at the centre, features a 4 mm diameter sensing area, while the total substrate dimension measures $34mm \times 10mm \times 0.5mm$. Figure 4.1 illustrates the physical electrode (a) and its 3D computational counterpart (b), including the spatial arrangement of the electrodes and the electrolyte droplet covering all three terminals during electrochemical measurements.

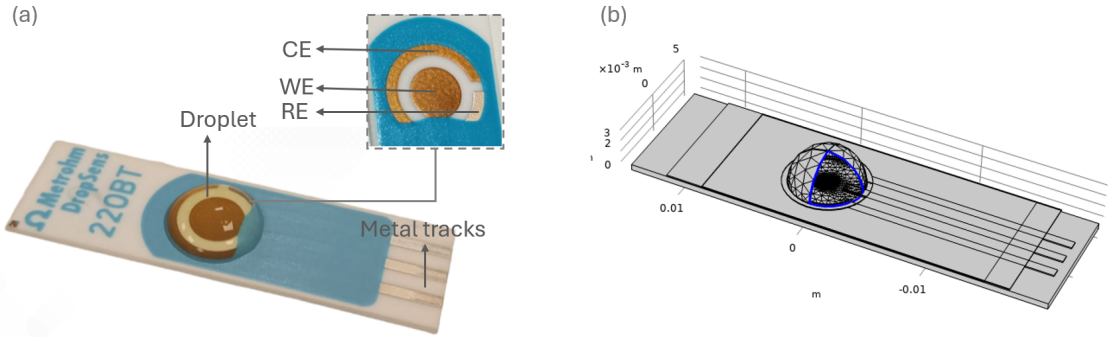

Figure 4.1: Electrode Geometry and Simulation Setup for Modelling. (a) Image of the Metrohm DropSens 220BT SPE used in this project. Zoomed-In: The electrode consists of a conventional three-electrode system, including a WE made of gold, a CE, and a RE made of silver. A droplet of electrolyte is deposited on the electrode surface, covering all three electrodes for electrochemical measurements. The metal tracks facilitate electrical connections. The inset shows a magnified view of the electrode layout, highlighting the spatial arrangement of the three electrodes. (b) 3D computational model of the electrode geometry implemented in COMSOL Multiphysics®, featuring a hemispherical droplet of electrolyte on the electrode surface. The mesh structure illustrates the discretisation of the computational domain for numerical simulations of electrochemical processes.

The development of the COMSOL Multiphysics® models required a systematic approach which involve multiple stages. The process started with setting up the geometry, assigning necessary material properties, and choosing the right physics to

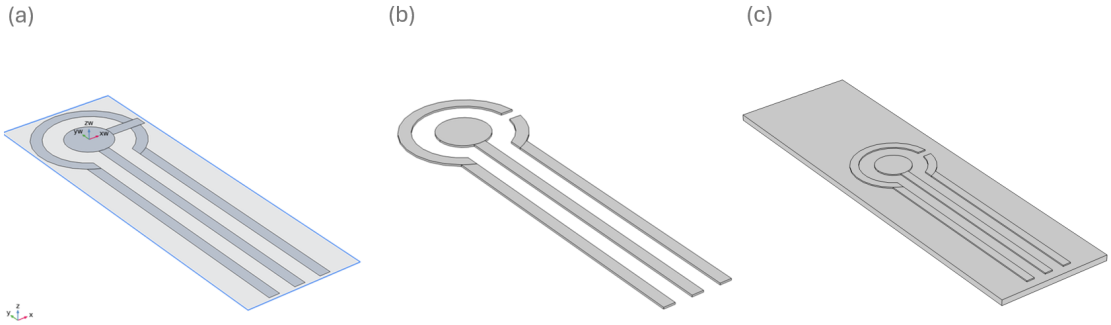

Figure 4.2: Electrode Geometry and Simulation Setup for Modelling. Image (a) shows the creation of the work planes for the electrode and conductive tracks. Image (b) shows the extrusion of the electrodes and conductive tracks, while image (c) shows the extruded electrode geometry to represent the ceramic substrate.

describe the electrochemical behaviour. Then, the appropriate boundary conditions were applied, followed by meshing and running simulations. Finally, results were analysed to validate the model.

The image in Figure 4.1(a) shows the physical 220BT SPE, with an inset that highlights the electrode layout. A droplet of electrolyte spans the WE, CE, and RE, enabling ionic conduction during measurements. Figure 4.1(b) shows the 3D computational model, which includes a hemispherical electrolyte droplet and a discretised mesh structure for numerical simulations.

Model Geometry Setup

First, a work plane (x-y plane) was defined in the geometry module. Then, circular, arc, and rectangular shapes corresponding to the WE, CE, RF, and their conductive tracks were drawn on this plane. These components were extruded and then the substrate upon which the electrodes are deposited is created using a rectangular block element as seen in Figure 4.2a, b, and c.

The hemisphere chamber that contains the electrode and electrolyte solution is created using a spherical element. The extruded electrodes were subtracted from the hemispherical domain so that only the electrolyte region remained. This step explicitly creates the electrode-electrolyte interface essential for simulating ionic transport and electrochemical reactions as seen in Figure 4.3.

To create the electrode-electrolyte computational domain, a boolean subtraction operation is performed, where the electrodes (WE, CE, and RE), as well as the contact pads, are subtracted from the hemispherical domain. This process explicitly removes the solid electrode structures, presents the electrode-electrolyte interface and ensures that only the electrolyte-filled region remains as the computational domain, allowing for the accurate simulation of ionic species transport and electrode reaction kinetics within the solution. To reduce the model by removing the contact pads, a z–x plane

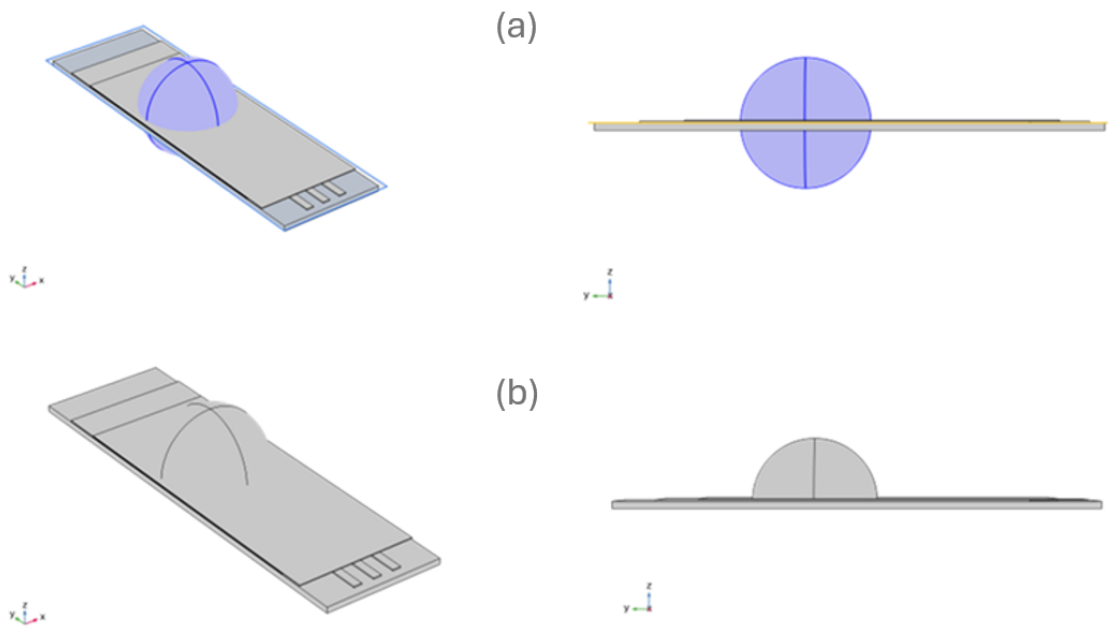

Figure 4.3: Creation of the spherical domain and truncation to a hemisphere Image (a) is showing the creation of a spherical chamber, both isometric and side views while image (b) shows the reduction of the sphere to a hemispherical shape, both isometric and side views.

was introduced to slice through the substrate, as shown in Figure 4.4a. The unwanted substrate and contact pads were then deleted (Figure 4.4b). Finally, the remaining electrode and substrate layer was subtracted from the hemispherical domain, leaving only the electrode-electrolyte interface for simulating mass transport and reaction kinetics, without electric current and potential distribution within the bulk electrode material (Figure 4.4c).

Model Material Properties

In the model, water was chosen as the primary material for the computational domain. This is representative of the electrolyte medium consisting of 3 mM ferri/ferrocyanide in PBS solution in which the reaction occurs. The key properties of water used in the simulating model are density ($\rho = 1000 kg/m^3$), dynamic viscosity $\mu = 8.9 \times 10^{-4} Pa \cdot s$, relative permittivity $\epsilon = 80$.

Electroanalysis Physics

To simulate the CV of ferri/ferrocyanide redox reaction, the Electroanalysis physics was selected as this is the interface specifically designed for electrochemical processes in COMSOL Multiphysics®, allowing the incorporation of reaction kinetics,

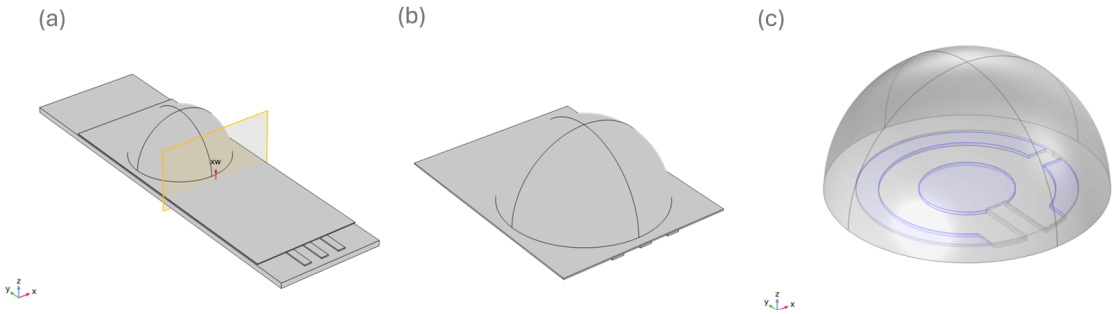

Figure 4.4: Electrode Final Geometry Model. Image (a) shows the creation of a z-x work-plane to partition the biosensor domain while image (b) illustrates the cut. Image (c) shows the final domain of the biosensor showing the electrodes that are contained in a hemispherical reaction chamber.

mass transport (via diffusion and, if needed, convection), and the applied potential sweep.

In this model, the **no potential gradient** setting was selected as this implies that no explicit solution for the potential gradient in the bulk solution is required as the focus is on the mass transport of redox species at the electrode-electrolyte interface during CV.

Dependent Variables and Ionic Transport Settings

For the redox species, two dependent variables cA and cB were defined to represent the oxidised ferricyanide and reduced ferrocyanide. In the absence of fluid flow, the electrolyte velocity field was set to zero metres per second in all directions. Both species were assigned a diffusion coefficient of $7 \times 10^{-10} m^2/s$, which aligns with reported experimental data on ferricyanide and ferrocyanide in PBS [70].

Boundary Conditions Settings

For the initial values of the whole domain, the bulk concentration C_bulk was specified for the oxidising species (ferricyanide, $Fe(CN)_6^{3-}$), while the reducing species ((ferricyanide, $Fe(CN)_6^{4-}$) is set at zero. At the upper boundary of the electrolyte domain, the bulk concentration was applied to the main supply of reactants. Although electroneutrality had been imposed, the imposition of this boundary condition helps to improve numerical stability and accelerates convergence during the simulation.

Working Electrode Boundary. Here, the CV option was selected to impose the applied potentials at the WE, sweeping from -0.3 V to 0.6 V at a fixed scan rate of 100 mV/s, unless a sweep of parameters was performed. The *Electrode Reaction* option was then activated to define the redox reaction kinetics. A single-electron transfer was selected as the ferri/ferrocyanide couple undergoes a one-electron exchange. The stoichiomet-

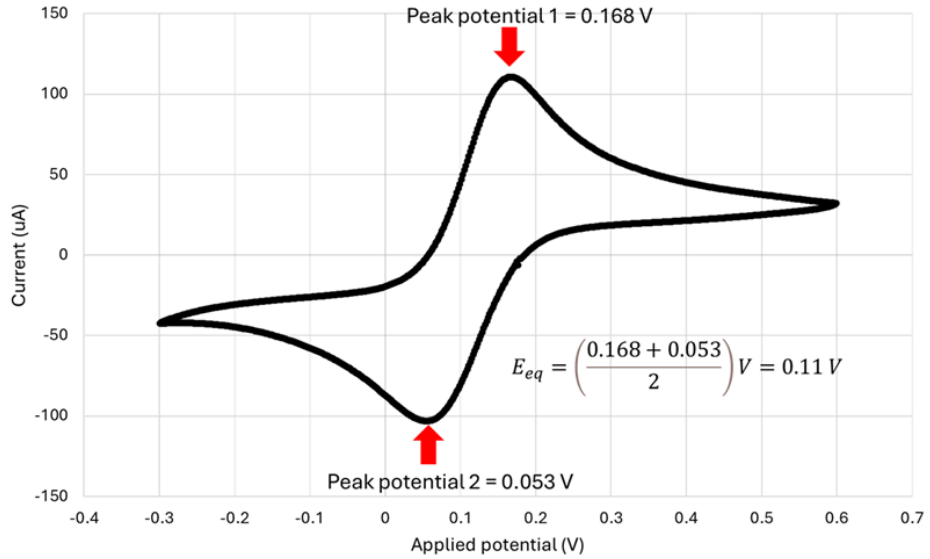

Figure 4.5: Experimental Cyclic Voltammogram of a Bare Gold Electrode in a Ferri/Ferrocyanide Solution. The is a voltammogram showing the oxidation and reduction curve peaks for a 3 mM ferri/ferrocyanide system in PBS, measured at a bare Au WE. Red arrows indicate the sweep direction, and the midpoint potential (marked by parentheses) represents the equilibrium potential for the redox couple.

ric coefficients were set to +1 for ferricyanide and -1 for ferrocyanide, ensuring mass balance.

The equilibrium potential, E_{eq}, was derived from the experimental cyclic voltammograms by identifying the midpoint between the oxidation and reduction peaks as shown in Figure 4.5. The equilibrium potential for the redox reaction was determined from the cyclic voltammogram to be 110 mV.

For the exchange current density field, the Butler-Volmer equation was selected from the option as the reaction kinetics, while the reference value i_0 was coupled to $i_0 = nFkC_{bulk}$ for the bare Au electrode case, and $k_eff = k_0 \exp(-\gamma[c_A B])$ for the case of electrode functionalised with MUA layer, enzymes, and antibody.

Working Electrode The appropriate equations that model the cyclic voltammetry processes at the WEs are presented here. These processes include charge-transfer kinetics, overpotential and interfacial capacitance. The CV is modelled in the form of a time-dependent potential sweep, where potential within the oxidation and reduction windows are applied to the WE at a specified time range defined by the scan rate. This is formulated as:

$$E(t) = E_{init} + vt, \tag{4.1}$$

where $E(t)$ is the potential applied at a given time t, E_{init} is the initial potential,

and v is the scan rate in (mV/s). For a reversible reaction, the potential is imposed linearly between vertex potentials E_{vertex}, where a reversal occurs right after a vertex potential is attained. E_{vertex} can be directly inferred experimentally measured cyclic voltammograms from the potential at the extreme ends of a CV curve.

At the electrode surface, the flux of ionic species is related to the local current i at the electrode-electrolyte that is driven by the reaction kinetics as described by the Butler-Volmer equation given in Equation 2.23.

The equilibrium potential for the bare gold electrode case is based on the Nernst equation because the redox reaction is reversible. It is defined as:

$$E_eq = E_0 + \frac{RT}{nF} \ln \frac{c_O}{c_R} \tag{4.2}$$

The exchange current i_0 is formulated using the mass action law, as it is related to the rate constant k by:

$$i_0 = nFkc_bulk \tag{4.3}$$

Self-Assembled Monolayers on the WE The introduction of SAMs, enzymes and antibodies on the bare Au electrode will impact the electron transfer, reaction kinetics and diffusion of reactive species at the electrode surface. This is implemented in the model by modulating the exchange current density via the reaction rate constant. The additional barrier posed by the antibody to electron transfer is specified using a modified rate constant k_{eff}, expressed as:

$$k_{eff} = k_0 \exp(-\gamma[c_{AB}]) \tag{4.4}$$

where k_0 is the reaction rate constant without the antibody layer, c_{AB} is the concentration of antibodies, and γ is a fitting parameter that represents the sensitivity of k_0 to c_{AB}.

Consequently, exchange current density Equation 4.3 becomes:

$$i_0 = Fk_{eff}[HRP]c_{bulk} \tag{4.5}$$

Where [HRP] is the enzyme antibody dilution factor.

Counter Electrode Boundary. For the Au CE, no reaction kinetics were applied because it completes the circuit with the working electrode, serving as a current-supplying electrode rather than a reactive surface. For this reason, only the double layer capacitance boundary condition was applied to account for charge capacitance storage at the electrode-electrolyte interface. This approach guarantees that the current response at the counter electrode is purely capacitive i_{captn} and non-faradaic in nature. The capacitance current and the double layer capacitance C_{dl} are presented in equations Equation 2.25 and Equation 2.26. The prescription of the double layer

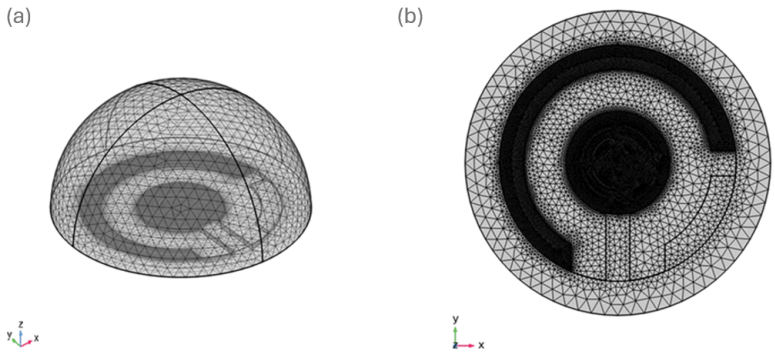

Figure 4.6: Meshing of the electrodes. Image (a) show the meshing of the 3D computational domain while image (b) shows the refinement of the meshing at the electrode region.

capacitance as a boundary is directly applied to the CE in the absence of a faradaic reaction on the CE in the same way as the WE described above.

EIS Fitting

EIS data that were obtained experimentally were plotted in the form of Nyquist plots. These plots were then fitted to an appropriate equivalent circuit model to extract key parameters that characterise the electrode system. The fitting procedure was performed using the PSTrace software from PalmSens and the open source software FitMyEIS. From this, the double-layer capacitance was determined and applied to the model.

Meshing

The computational domain is discretised using about 22.316 tetrahedral elements, which are well-suited for complex 3D geometries and 4.826 triangular elements. This is shown in Figure 4.6a and b. To ensure accurate resolution of key electrochemical processes, finer mesh refinements are applied at the electrode surface and the electrode-electrolyte interface. This refinement was necessary to accurately capture transport phenomena, ionic species diffusion, and reaction kinetics, which occur predominantly at these interfaces, leading to more accurate and stable numerical solutions. The minimum element quality is 0.1987, while the average element quality is 0.642, indicating a reasonably well-shaped mesh suitable for numerical convergence.

Solver Settings and Simulation

A time-dependent solver was used in COMSOL Multiphysics® to simulate the electrochemical process. This approach is necessary for the transient mode of the CV test,

where the applied potential is varied with respect to time, which impacts reaction kinetics and diffusive transport, where concentration and reactions may evolve. A direct and fully coupled solver is selected to solve the algebraic system of the equations due to its robustness in handling the stiff nature of the electrochemical problem. The fully coupled approach is used in solving all the dependent variables namely, concentration and electric potential simultaneously to obtain stable and accurate solution.
For the numerical time-stepping, the backward differentiation formula (BDF) method is selected. These numerical simulation setting were specifically chosen to ensure numerical stability and accuracy of the transient simulation as well as an efficient resolution of the stiff differential equations that may arise during the diffusion of ionic species. In this Table 4.8, the list of parameters applied in simulations can be seen.

Table 4.8: Input parameters and their notation in COMSOL Multiphysics.

Input parameter	Value	Note
Substrate length	34 mm	Length of substrate
Substrate width	10 mm	Width of substrate
Substrate thickness	0.5 mm	Thickness of substrate
Electrode thickness	0.1 mm	Thickness of electrodes
WE diameter	4 mm	Diameter of working electrode
CE width	0.7 mm	Width of counter electrode
Drop diameter	4.45 mm	Diameter of droplet
Diffusion coefficient	7e-10 m^2/s	D_o
Charge transfer coefficient	0.5	α_a and α_c
CV vertex potential 1	-0.3 V	$E_{\text{vertex-1}}$
CV vertex potential 2	0.6 V	$E_{\text{vertex-2}}$
Scan rate	100 mV	SR comparable to experiments
Equilibrium potential	110 mV	E_0
Conductivity	1.6 S/m	$Cond$
Electrolyte concentration	3 mM	C_{bulk}
Double layer capacitance	0.1 - 0.2281 F/m^2	C_{dl}
Number of electrons	1	No of electrons transfer
Reaction rate constant	0.03 m/s	K_o

5 Results & Discussion

In this chapter, all the relevant results obtained throughout the project are presented and discussed. The chapter is divided into four sections, where sections 5.1, 5.2, and 5.3 are from the experimental part and section 5.4 is from the computational part. The results for each section are presented and discussed before moving to the next section.

5.1 Method 1: MUA, HRP, & Strep-HRP

In the first method, the goal was to successfully functionalise the SPGE surface with a SAM of MUA, followed by the detection of HRP and Strep-HRP. In order to test how low a concentration the sensor could detect, varying concentrations of HRP/Strep-HRP were tested, i.e. from high to low concentrations. However, since all the electrodes utilised throughout the project were previously used, it was imperative to clean them before running the functionalisation and detection tests. Hence, the results from the cleaning process are presented and discussed first, followed by the functionalisation and detection results.

5.1.1 Electrode Cleaning Process

The initial cleaning procedure consists of only electrochemical cleaning with Step 1 and Step 2. In **Step 1**, the electrodes were cleaned by using 150 mM PBS and underwent CA for 30 s (at $V = 1.4V$), while in **Step 2**, 50 mM sulfuric acid was added onto electrodes followed by 10 cycles of CV (potential sweep: $1.4V$ to $-0.1V$). Further details can be found in section 4.2.2. After each cleaning step, CV was measured to verify the cleanliness of the electrode surface. The voltammogram from CV conducted after Step 1 cleaning can be seen in Figure 5.1 (top), while the voltammogram from CV after Step 1 and 2 can be seen in Figure 5.1 (bottom). The verifying CV was conducted with the following settings: potential sweep: $0.6V$ to $-0.3V$, potential step: $0.002V$, no. of scans: 5, and scan rate: $0.1V \cdot s^{-1}$. In Figure 5.1 (top), the CV plots for three different electrodes (E1, E2, and E3) are shown, before (dashed lines) and after (dotted lines) undergoing the first step of the electrochemical cleaning process.

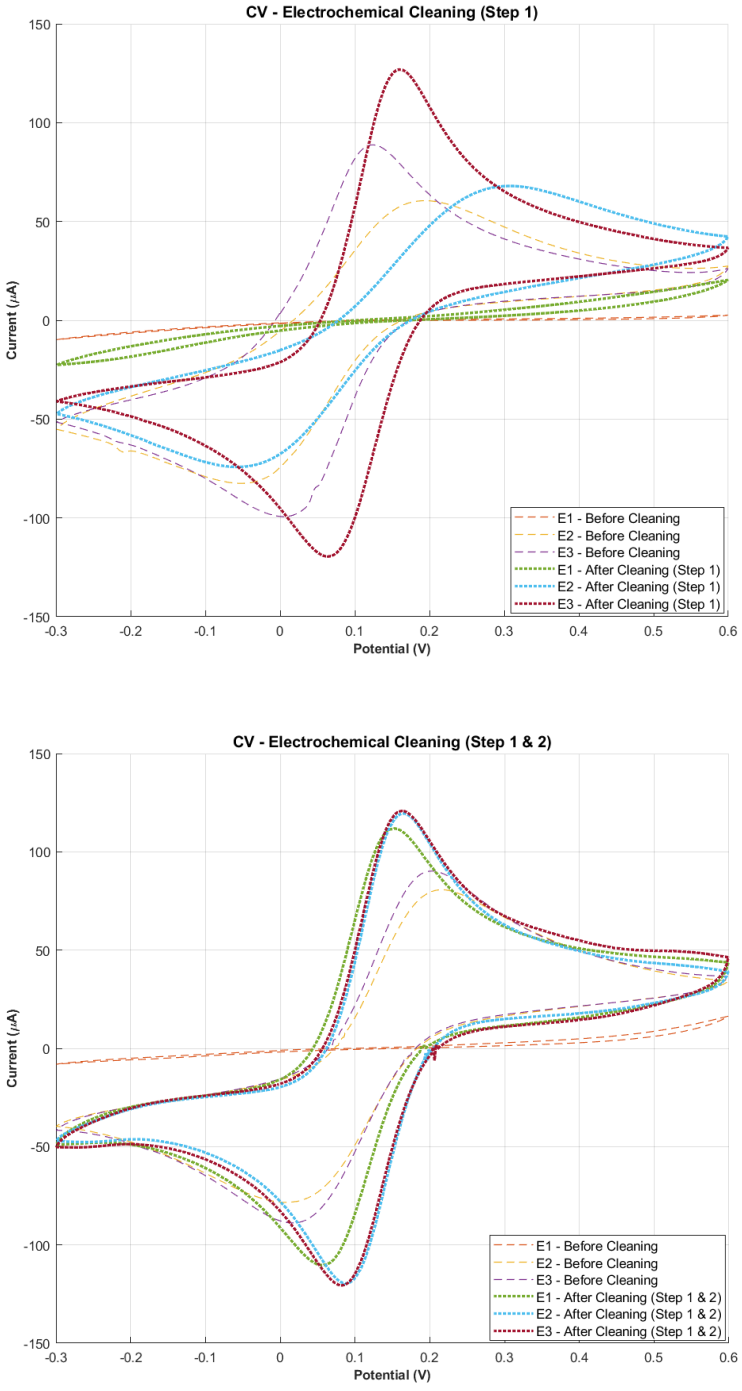

Figure 5.1: CV Measurements of Initial Electrode Cleaning (Step 1-2). Potential sweep: 0.6 V to -0.3 V, Potential step: 0.002 V, Scan rate: $0.1V \cdot s^{-1}$, No. of scan: 5. **Top:** Before and after electrochemical cleaning (Step 1). **Bottom:** Before and after electrochemical cleaning (Step 1 & Step 2). Dashed lines represent before cleaning, while dotted lines represent after cleaning.

Although all three electrodes follow a similar trend, their magnitudes and exact peak positions vary. This could be due to inherent differences in electrode composition, initial contamination levels, or surface morphology (e.g. surface roughness like physical scratches on the surface). Comparing the dashed plots with the dotted plots of all three electrodes, E3 (purple and brown, respectively) shows the most pronounced shift after cleaning, with a large positive peak near $+0.15$ V to $+0.20$ V (reaching around +120 μA) and a corresponding negative sweep dipping near -120μA. This could suggest that Step 1 cleaning can significantly alter surface reactions by removing contaminants and exposing more active sites. E2 (yellow and blue) likewise shows a visible increase in current response after cleaning, although not as large as E3. The shift in peak potentials could highly indicate changes in oxidation/reduction processes. E1 (red and green) shows a more moderate, but noticeable, increase in peak current indicating the electrode surface has been renewed to some extent.

The most impact, however, is seen after the second step of the electrochemical cleaning process. In Figure 5.1(bottom), the CV plots for three different electrodes before and after undergoing both (electrochemical) cleaning steps are shown. Once again, enhanced peak currents and shifted peak positions are observed, although much more pronounced in this case. Comparing the dashed plots (before cleaning) with the dotted plots (after cleaning), it is evident that the electrodes have been significantly cleaned. E1 (dashed red and dotted green) exhibits the highest shift in oxidation and reduction currents, as the anodic and cathodic peak currents increase significantly after electrochemical cleaning (from $\sim \pm 10\mu$A to $\sim \pm 110\mu$A). The peak separation also becomes smaller, indicating improved electron transfer kinetics. This suggests that cleaning has effectively removed surface contaminants, enhancing the electrochemical activity of the electrode. Compared to E2 (dashed yellow and dotted blue) and E3 (dashed purple and dotted red), the changes in E1 are more pronounced, implying that this electrode had more significant surface passivation or fouling prior to cleaning. The overall improvement in current response and peak sharpness once again validates the need for a cleaning process to regain electrode performance.

However, despite undergoing electrochemical cleaning, it was found that the electrodes were not cleaned to satisfaction. Consequently, a second cleaning method, i.e. mechanical cleaning, was implemented. This cleaning method involved polishing the electrode surface with 0.3 μm grain size alumina polishing powder, as described in section 4.2.2. By combining these two cleaning methods, electrochemical cleaning and mechanical cleaning, a significant improvement in electrode performance was observed. The CV profiles of six different electrodes that underwent different cleaning processes can be seen in Figure 5.2. The three electrodes that underwent both mechanical

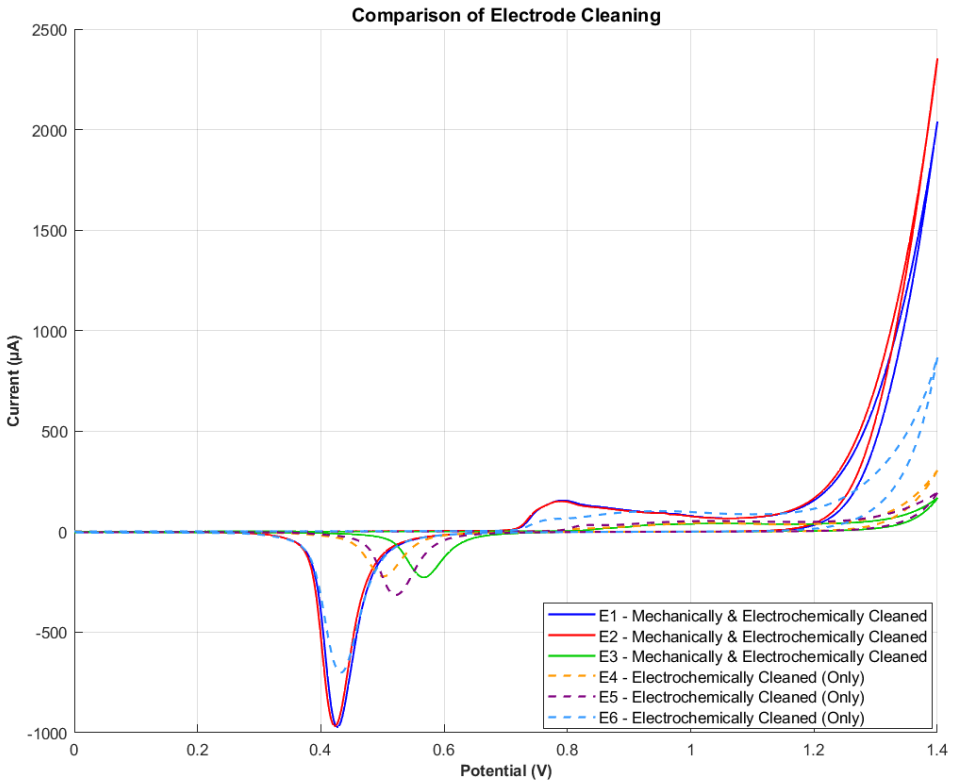

Figure 5.2: Comparison of Electrode Cleaning Methods. The x-axis represents potential (V), while the y-axis represents current (μA). These CV voltammograms compare the electrochemical behaviour of electrodes subjected to different cleaning methods. The solid lines represent electrodes that underwent both mechanical and electrochemical cleaning (E1 = blue, E2 = red, E3 = green), while the dashed lines correspond to electrodes that were only electrochemically cleaned (E4, E5, E6). Electrodes that underwent both mechanical and electrochemical cleaning (blue, red, and green lines) show higher current responses and better distinct redox peaks. In contrast, electrodes that were only electrochemically cleaned (purple, orange, and light blue lines) show relatively lower currents and broader peaks, suggesting incomplete removal of contaminants or a less active surface.

and electrochemical cleaning (solid lines) exhibited significantly higher current responses compared to the three electrodes that underwent electrochemical cleaning (dashed lines) only. This suggests that mechanical cleaning effectively removed residual contaminants that electrochemical cleaning alone could not, causing enhanced electrochemical activity and improved reproducibility. This is also in alignment with the literature, as many groups have successfully used combinations of electrochemical and mechanical cleaning procedures to enhance electrode performance (in particular SPEs) [76], [77].

In certain cases, despite utilising both mechanical and electrochemical cleaning methods, the electrochemical performance of the electrodes did not improve signifi-

cantly as expected. For instance, E3 (electrode 3) in Figure 5.2 exhibited worse performance than electrodes E5 and E6 (both underwent electrochemical cleaning only). A possible cause to this could be the electrode topography, as all the SPEs utilised in this project were used previously by other groups. Consistent repeated use (including different electrochemical measurements, various functionalisation processes, and cleaning methods) leads to significantly higher surface roughness (e.g. defects)[45], which means the actual surface area of the SPEs are much bigger. This could lead to the adsorption or entrapment of contaminants or residual species, which are not efficiently removed by either cleaning methods, thus reducing the accessibility of active sites for redox reactions and eventually leading to reduced electron transfer kinetics [78]. Furthermore, it has been found in previous studies, that when conducting faradaic EIS experiments using ferri/ferrocyanide with Au electrodes (such as in this case), the electrode surface is severely damaged over time- even under optimal conditions. This happens due to the Au atoms at the surface being etched by cyanide ions from the solution, leading to the Au surface being degraded over time. Consequently, surface defects and/or increased roughness is created, which, in turn, causes the electrochemical performance and reliability of the electrode to significantly decrease. This effect has also been seen for Au electrodes with SAMs, despite the latter being known for stabilising and enhancing electrode performance. The degradation of the Au surface, and thereby also any consequences of this (e.g. defects), causes the SAM structure to become unstable and non-uniform, eventually leading to unreliable measurements [45].

5.1.2 Functionalisation and Detection Tests

After the cleaning step, the SPGEs were functionalised with a SAM of MUA, followed by activation via EDC/NHS chemistry and the addition of HRP and Streptavidin-HRP (Strep-HRP), respectively. Here, three different enzyme concentrations were tested for two reasons: 1) in order to see if and how different concentrations of enzymes would affect the electrochemical performance of the SPGEs and 2) the limit of detection of enzymes (i.e.: how small concentrations can be reliably and successfully detected by the SPGE?). The respective enzymes were diluted in 1:20, 1:100, and 1:500 ratios. At this step, however, it was not deemed relevant to include the CV profiles of the 1:100 and 1:500 dilutions, as the point with this verification step was to merely confirm the successful immobilisation of MUA and enzymes on the SPGEs. In order to verify that each layer (MUA and HRP/Strep-HRP) was indeed anchored to the electrode surface, CV measurements were conducted using the redox couple ferri/ferrocyanide. The voltammograms with the CV profiles of each functionalisation step are shown in Figure 5.3 (top).

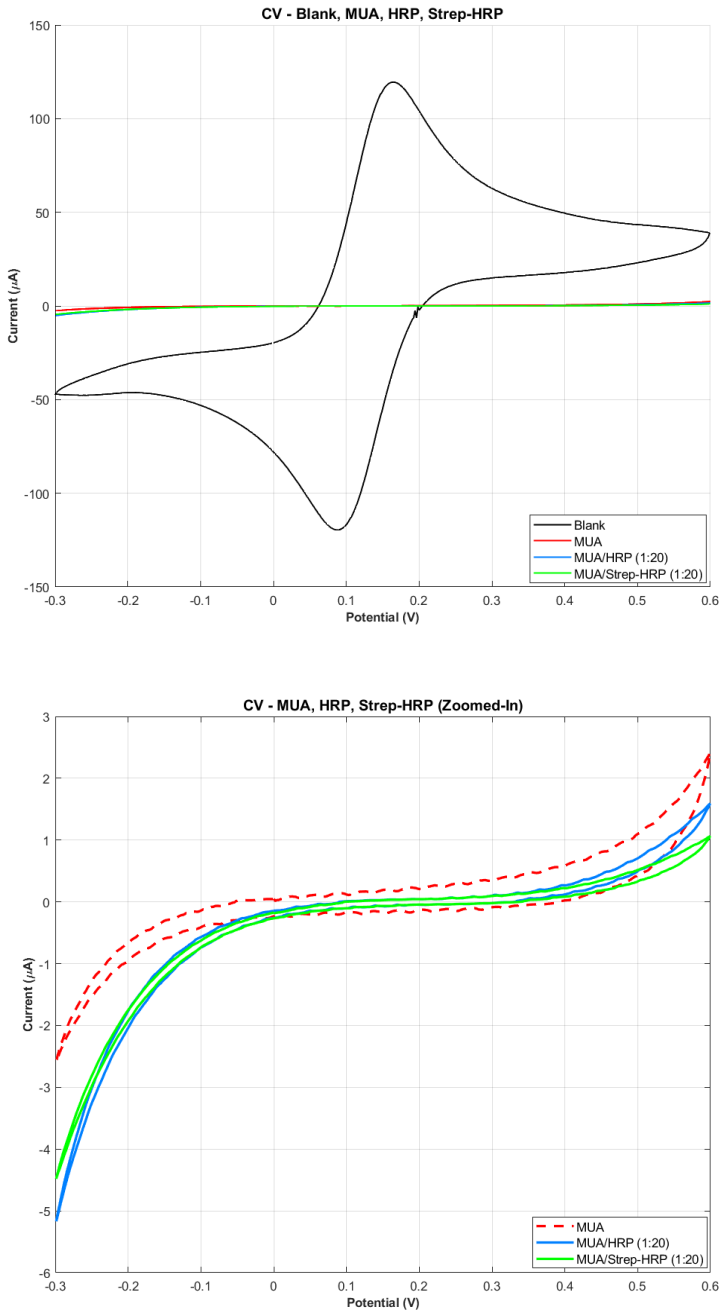

Figure 5.3: Voltammograms from CV Measurements on SPGE after Functionalisation with MUA and Enzymes. Settings: potential sweep: 0.6 V to -0.3 V, potential step: 0.002 V, scan rate: 0.1 $V \cdot s^{-1}$, number of scans: 5. Ferri/ferrocyanide (3 mM) was utilised as the redox probe. **Top:** The CV voltammograms represent different stages of functionalisation; blank SPGE (black), SPGE/MUA (red), SPGE/MUA/HRP (1:20-blue), and SPGE/MUA/Strep-HRP (1:20-green). **Bottom:** A zoomed-in view of the above CV voltammogram.

The CV profile of the blank electrode exhibits a characteristic duck-shaped profile (with distinct redox peaks), which is to be expected due to the electrolytes freely interacting with the bare Au surface and exchanging electrons. In comparison, the CV profiles of MUA (red), MUA/HRP (blue), and MUA/Strep-HRP (green) are nearly flat. This confirms the successful immobilisation of the MUA layer and subsequent enzyme attachment, as the electrode surface is completely covered by the nearly insulating SAM structure and enzymes. This, in turn, renders the interaction of electrolytes with the electrode surface nearly impossible, resulting in almost negligible signals. Zooming in on the CV profiles of MUA and MUA/enzyme structures, Figure 5.3 (bottom), a small difference can be seen in the electrochemical activity of the MUA layer and the enzymes; i.e. the MUA layer (red) exhibits lower signals compared to the MUA/enzyme layers (blue and green). This is likely due to MUA for two reasons: 1) it (MUA) is acting as an almost impenetrable insulating layer, making it difficult for electrons to "shuttle" between the electrode and electrolyte, thus leading to reduced charge transfer, and 2) the negatively charged carboxylic acid group of MUA shields the electrode surface from ferri/ferrocyanide ions, effectively reducing charge transfer at the electrode/electrolyte interface. This electrostatic repulsion can be avoided by using another redox probe, where ferroscene is a good alternative. The MUA-functionalised electrodes with HRP enzymes attached (MUA/HRP and MUA/Strep-HRP), exhibit higher signals (reduction reactions in particular). This is due to HRP acting as an efficient redox mediator, facilitating the exchange of electrons between the electrolytes (ferri/ferrocyanide ions) and electrode, resulting in higher current responses.

The next step was to run EIS tests on the SPGEs at the different functionalisation steps. The EIS results are shown in Figure 5.4, where the top panel displays the Nyquist plots for MUA and MUA/HRP (1:20, 1:100, 1:500), and the bottom panel displays those of MUA and MUA/Strep-HRP (1:20, 1:100, 1:500). Immediately, the MUA plot (red) stands out in both cases, as they exhibit the largest semicircles and, consequently, the highest charge transfer resistance (R_{CT}). In the top panel, the next-highest resistance is displayed by the MUA/HRP (1:500-green) structure, followed by MUA/HRP (1:100-purple) and MUA/HRP (1:20-yellow), and the blank electrode (blue) showing the least resistance (inset showing a close-up of the blank electrode). The high resistance displayed by the MUA layer could be due to a number of reasons: 1) the terminal end of MUA layer shields the electrode surface from any ferri/ferrocyanide ions, thereby reducing charge transfer at the Au surface, 2) the electrodes are previously used, thus causing two factors at play: i) heightened surface roughness causing defects which, in turn, causes non-homogeneous SAM (MUA) formation [45], and ii) increased surface area causing the entrapment and adsorption of residual species or contaminants [78], both factors ultimately leading to increased R_{CT}. Finally, 3) high concentrations of MUA leads to densely packed SAM formation at the interface [79], which is further aided by the lack of proper washing/rinsing of the SPGE. This can lead to a blocking effect at the electrode surface, resulting in a significantly

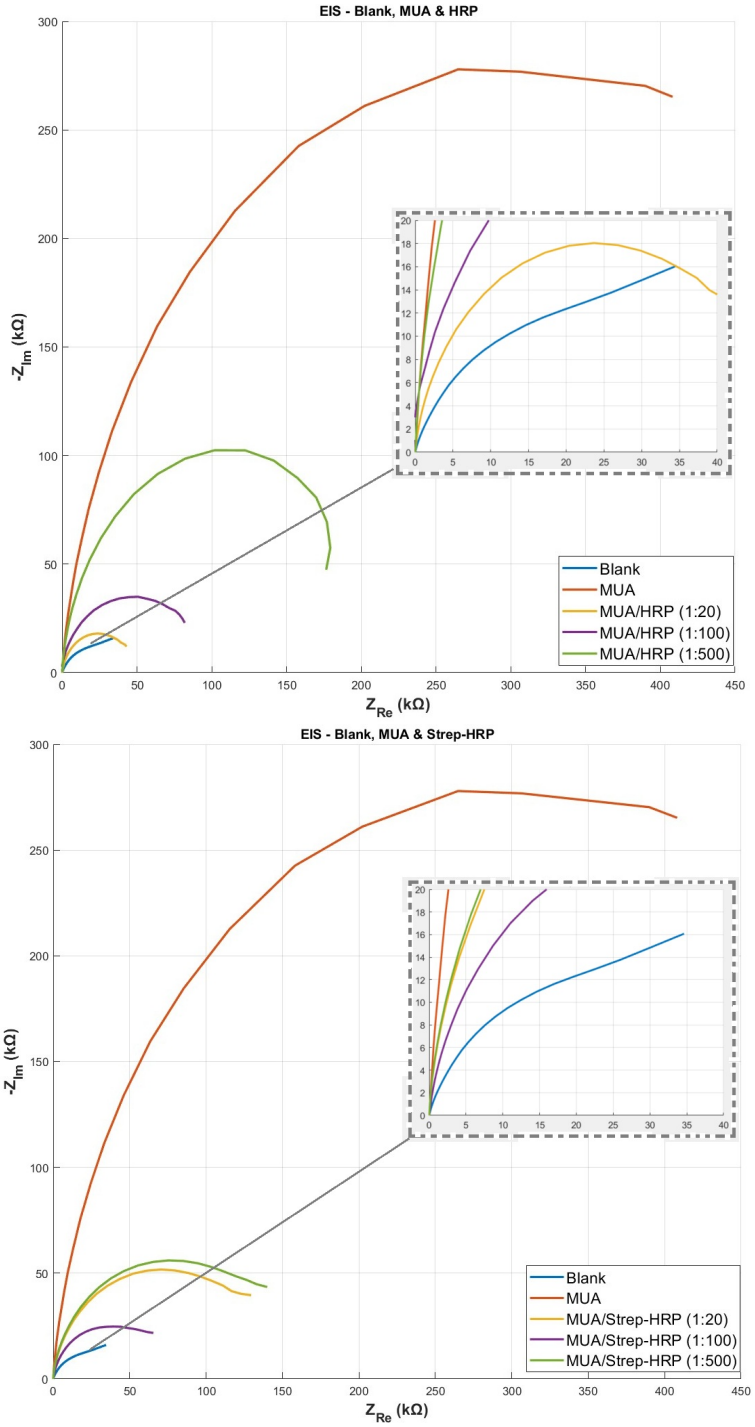

Figure 5.4: Nyquist Plots from EIS Measurements on SPGEs after Functionalisation with MUA and Enzymes. Settings: E(dc)=0.75 V, E(ac)=0.01 V, freq. range: 0.1 Hz to 100.000 Hz. Ferri/ferrocyanide (3 mM) was utilised as the redox probe. **Top:** Nyquist plots of blank SPGE (blue), SPGE/MUA (red), and SPGE/MUA/HRP (1:20-yellow), (1:100-purple), and (1:500-green). **Bottom:** Nyquist plots of SPGE (blue), SPGE/MUA (red), SPGE/MUA/Strep-HRP (1:20-yellow), (1:100-purple), and (1:500-green).

Table 5.1: The Charge Transfer Resistance at each Functionalisation Step. The values were extracted by fitting the experimental EIS data to Randles circuit model in the PSTrace v5.10 software from PalmSens.

Functionalisation Step	R_{CT} [kΩ]
Blank	0.306
MUA	3064
MUA/HRP (1:20)	22.92
MUA/HRP (1:100)	57.61
MUA/HRP (1:500)	154.5
MUA/Strep-HRP (1:20)	65.29
MUA/Strep-HRP (1:100)	24.05
MUA/Strep-HRP (1:500)	71.06

high R_{CT} [79]. The electrodes with MUA and HRP enzymes immobilised at the surface, however, show significantly less R_{CT}. This is likely due to an accumulation of the reasons for MUA displaying high R_{CT} and the redox-mediating nature of HRP; as already discussed above, the HRP enzyme is an excellent and efficient redox mediator. It interacts with the ferri/ferrocyanide ions in the solution, thereby causing a flow of electrons between the electrode and electrolytes, consequently displaying a relatively low R_{CT}. Contrary to expectations, however, the electrode with the highest enzyme dilution (and thus the lowest concentration) exhibits a higher R_{CT}. Conversely, the plot for the lowest enzyme dilution (and thus the highest concentration) shows the smallest R_{CT}. A possible explanation for this could be a direct consequence of the high R_{CT} of MUA. That is, the MUA concentration at the electrode surface is so high, that it overshadows any effect HRP has. Additionally, the negatively charged carboxylic acid groups completely cover the electrode surface and repel the majority of incoming electrolytes. Hence, when there is a high concentration of HRP at the electrode surface, such as the 1:20 dilution, the enzymes acts as a mask and shields the negatively charged carboxylic acid groups. As a result, the electrostatic repulsion at the surface is significantly reduced, allowing the electrolytes to interact with the electrode. Consequently, the R_{CT} is noticeably reduced, as is the case in Figure 5.4 (bottom). The same logic can be applied for the high R_{CT} of the 1:500 dilution; since there is less HRP enzyme present, the carboxylic acid groups cannot be sufficiently shielded and thus the electrode exhibits higher R_{CT}. In the bottom panel of Figure 5.4, a similar behaviour is observed for the SPGES with MUA/Strep-HRP immobilised on the electrode surface. Here, the 1:500 dilution still has the highest R_{CT}, followed by 1:20 with the next-highest R_{CT}, and the 1:100 with the lowest R_{CT}. This could be due to oversaturation of HRP enzymes at the electrode surface, leading to the opposite effect; the excess enzymes creates an insulating layer, thereby increasing the R_{CT} even further.

Similar to CV and EIS tests, CA tests were also run on the SPGEs at the different functionalisation steps. The CA results are shown in Figure 5.5, where the top panel

displays all the I-t plots for blank, MUA/HRP (1:20, 1:100, 1:500), and MUA/Strep-HRP (1:20, 1:100, 1:500), while the bottom panel is a zoomed-in view of the blank and MUA/Strep-HRP plots. Here, 1-Step™Turbo TMB-ELISA Substrate Solution was used as the redox mediator in the CA test, containing TMB and stabilised hydrogen peroxide. The TMB molecule is a redox-active chromogenic substrate, which undergoes HRP-catalysed oxidation in the presence of hydrogen peroxide [80], [81]. The oxidised product, TMB^+, is then electrochemically reduced back to TMB at the electrode surface, thus generating a measureable negative current (reduction current). Looking at the CA plots, the SPGE with a blank surface shows an almost non-existent signal. This aligns with expectations, since TMB cannot oxidise due to the lack of HRP present on the electrode surface. Electrodes immobilised with enzymes, however, exhibit reduction current generation to varying degrees. By comparing the I-t plots of HRP and Strep-HRP, however, it is clear that significantly more reduction current is generated at the electrode surface covered with HRP. Among the HRP dilutions, the 1:20 dilution (red) exhibits the highest generation of reduction current, the 1:100 dilution (green) exhibits intermediate current generation, while the 1:500 dilution exhibits the lowest current generation. This is in agreement with the corresponding EIS data for SPGE/-MUA/HRP in Figure 5.4 (top). That is, a high concentration of HRP (1:20) leads to higher surface coverage by the enzymes, as theorised for the EIS tests. As a direct consequence, since TMB oxidation is catalysed by HRP, the catalytic active sites are increased. This, in turn, leads to an in increase in reduction current generation, which is observed for the 1:20 (red) dilution in the CA test. Thus, the same logic can be applied for the two other HRP dilutions. That is, the 1:500 (orange) HRP dilution has the lowest enzyme concentration and a corresponding Nyquist plot showing the highest R_{CT}. This likely means the surface coverage is greatly reduced, causing a reduction in catalytic active sites for TMB and, ultimately, a lower reduction current.

The Strep-HRP-immobilised electrodes (dashed lines) follows the same trend, albeit with significantly lower current generation. The lower reduction currents could be due to a number of things such as 1) increased steric hindrance of the HRP enzymes due to the sheer size of the two biomolecules (Streptavidin $\sim$60 kDa, HRP $\sim$44 kDa), causing significant limitations to the TMB diffusion at the electrode interface, 2) random covalent attachment of the conjugate (EDC/NHS-activated MUA layer targets primary amines on the conjugate, leading to random covalent attachment and thus random and potentially non-optimal orientation of the enzyme), 3) due to the larger Streptavidin attachment, the electron transfer pathway from HRP to the electrode surface is significantly extended (long distance $\rightarrow$ reduced TMB^+ reduction rate $\rightarrow$ slow electron transfer $\rightarrow$ electron accumulation at the interface/double-layer region $\rightarrow$ excess charge storage instead of a smooth electron transfer flow $\rightarrow$ capacitive effect), 4) the larger conjugate occupies a larger surface area compared to HRP, greatly reducing the effective enzyme density at the electrode surface (even at the same dilution), and 5) the streptavidin molecule is non-conductive and could very likely block the electron

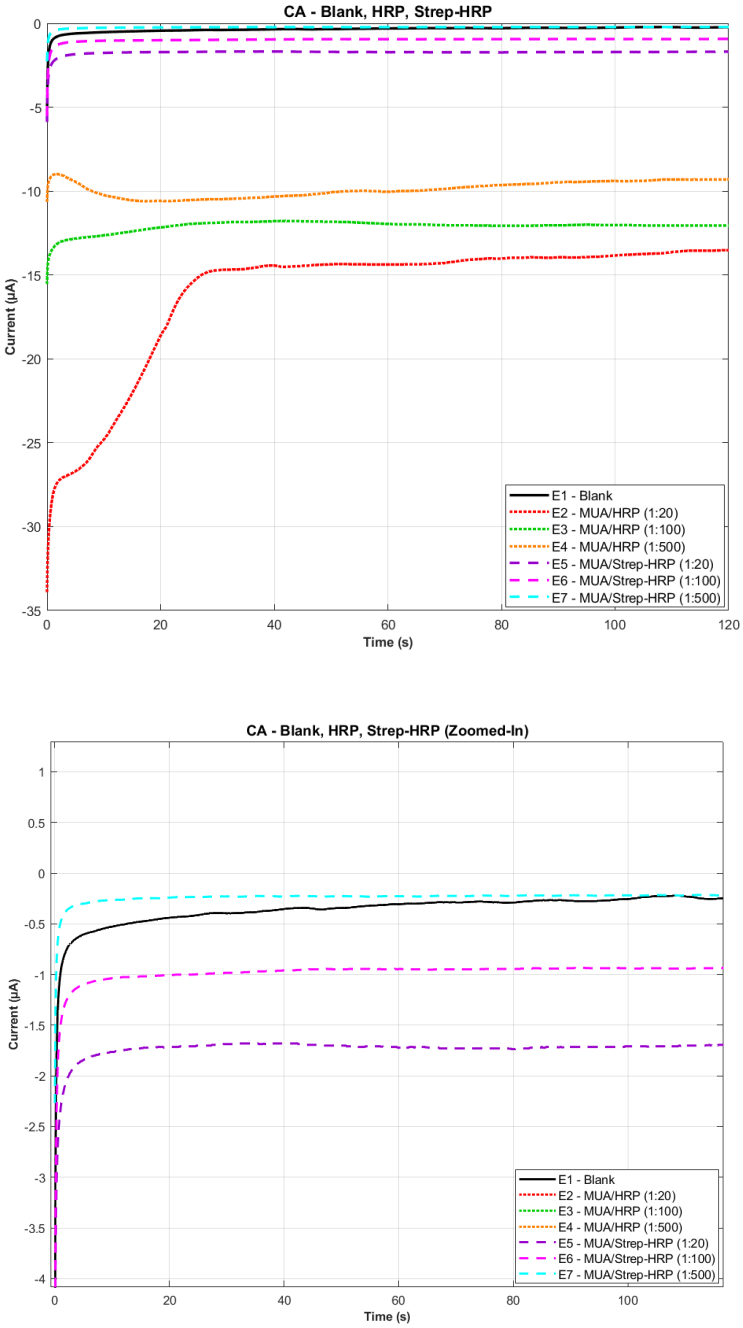

Figure 5.5: Current vs. time Plots From CA Measurements on SPGEs Functionalised with MUA and Enzymes. Settings: t. eq.=0 s, E(dc)=0.0 V, t.interval=0.1 s, t.run=120 s. 1-Step™Turbo TMB-ELISA Substrate Solution was used as the redox mediator. **Top:** purple: SPGE/MUA/Strep-HRP (1:20), pink: SPGE/MUA/Strep-HRP (1:100), blue: SPGE/MUA/Strep-HRP (1:500), red: SPGE/MUA/HRP layers (1:20), green: SPGE/MUA/Strep-HRP (1:100), orange: SPGE/MUA/Strep-HRP (1:500), black: blank SPGE. **Bottom:** A zoomed-in view of the above CA plots.

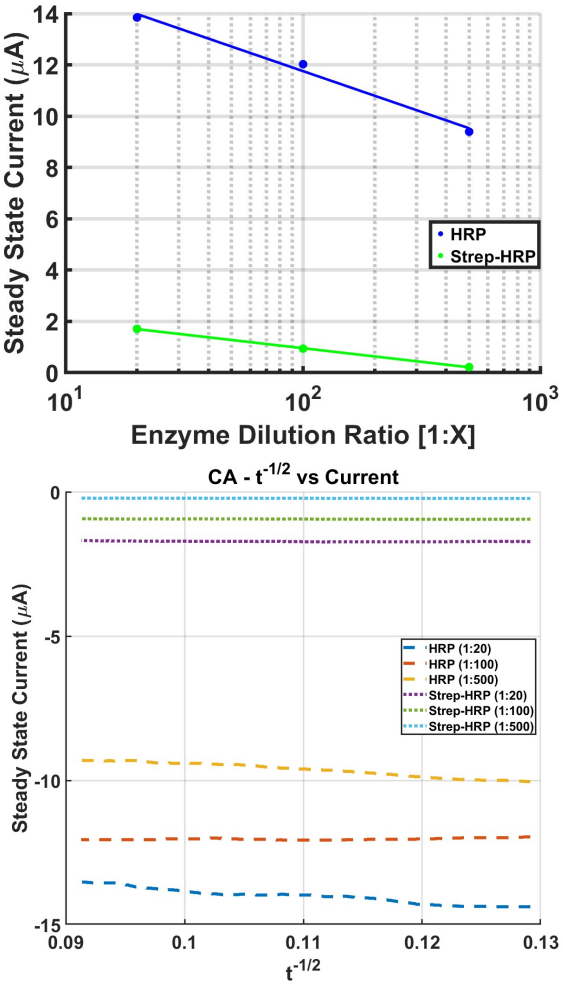

Figure 5.6: Log-Linear Plot of Steady State Current vs. Enzyme Dilution Ratio (top) and Steady State Current vs. $t^{-1/2}$ Plot (bottom). The plotted data was extracted from the CA data displayed in Figure 5.5. **Top:** Log-linear plots of HRP and Strep-HRP. Three data points were extracted for each enzyme dilution. The electrodes with HRP immobilised (blue) show higher reduction currents compared to those with Strep-HRP (green). **Bottom:** Current vs. $t^{-1/2}$ plot of all the enzyme dilutions. Dashed lines represent HRP, while dotted lines represent Strep-HRP. The HRP dilutions once again show superior current generation.

transfer pathways, consequently causing increased R_{CT}. This was also observed from the Nyquist plots, where the 1:20 dilution of Strep-HRP exhibits a much larger (almost 3-fold) charge transfer resistance ($R_{CT} = 65.29\ k\Omega$) compared to the 1:20 dilution of HRP ($R_{CT} = 22.92\ k\Omega$) (see Table 5.1). In Figure 5.6 (top), a log-linear plot of the steady state current vs. the enzyme dilution ratio is shown. From this plot, a linear dependence between the reduction current, and thus the electrochemical signals of TMB, and the enzyme dilution ratio can be seen. The higher the dilution ratio be-

comes, i.e. the enzyme concentration, the lower the electrochemical signals become (i.e. the reduction current). Both HRP and Strep-HRP-immobilised electrodes exhibit a decreasing current generation with decreasing concentration. This finding further verifies the successful formation of the different functionalisation steps. Additionally, by plotting the steady state currents of all the enzyme dilutions against $t^{-1/2}$, an almost constant trend is seen, which is in contrast with the Cottrell trend (a decreasing trend). This suggests that the redox reactions at the electrode-solution interface are not diffusion-controlled, but rather kinetically-controlled. This is also in accordance with the Nyquist plots, where the characteristic tail at the high frequency region (Warburg impedance region) is missing and only quarter-and semicircles are present, indicating that the electrochemical activity at the electrode-electrolyte interface is dependent on electron transfer kinetics and the capacitive double-layer effect [79].

5.2 Method 2: MUA, Antibody, & Strep-HRP

In this method, an additional layer of antibody (BAM1676) was incorporated into the functionalisation process to enhance the specificity of the biosensor compared to Method 1. The primary objective of Method 2 was to improve the selectivity of the biosensor by introducing a targeted antibody layer, allowing for more precise analyte detection. Here, a SAM of MUA was activated by EDC/NHS chemistry immediately followed by the immobilisation of an antibody monolayer. Lastly, Strep-HRP enzymes were added to the functionalised electrodes and electrochemical tests were conducted. This modification was expected to improve the specificity of the biosensor, as the enzyme would only bind to the biotinylated antibodies rather than non-specifically interacting with the SAM surface. Moreover, in order to asses the influence of antibody concentration on sensor performance and identify the optimal concentration, four different concentrations were prepared: 1 μg/mL, 5 μg/mL, 10 μg/mL, and 20 μg/mL. Similar to Method 1, three different Strep-HRP dilutions were tested: 1:20, 1:100, and 1:500. Each of the four antibody concentrations was systematically tested with all three Strep-HRP dilutions to evaluate their combined effect on electrochemical response.

Finally, it was found in Method 1 that to achieve better electrode cleanliness, a three-step cleaning process was required prior to testing: one mechanical step and two electrochemical steps. Thus, all electrodes utilised in Method 2 are cleaned following the three-step cleaning process.

5.2.1 Functionalisation and Detection Tests

The first step was to functionalise and activate the SPGEs with a SAM of MUA, followed by the immobilisation of antibodies onto the MUA layer. The presence of each

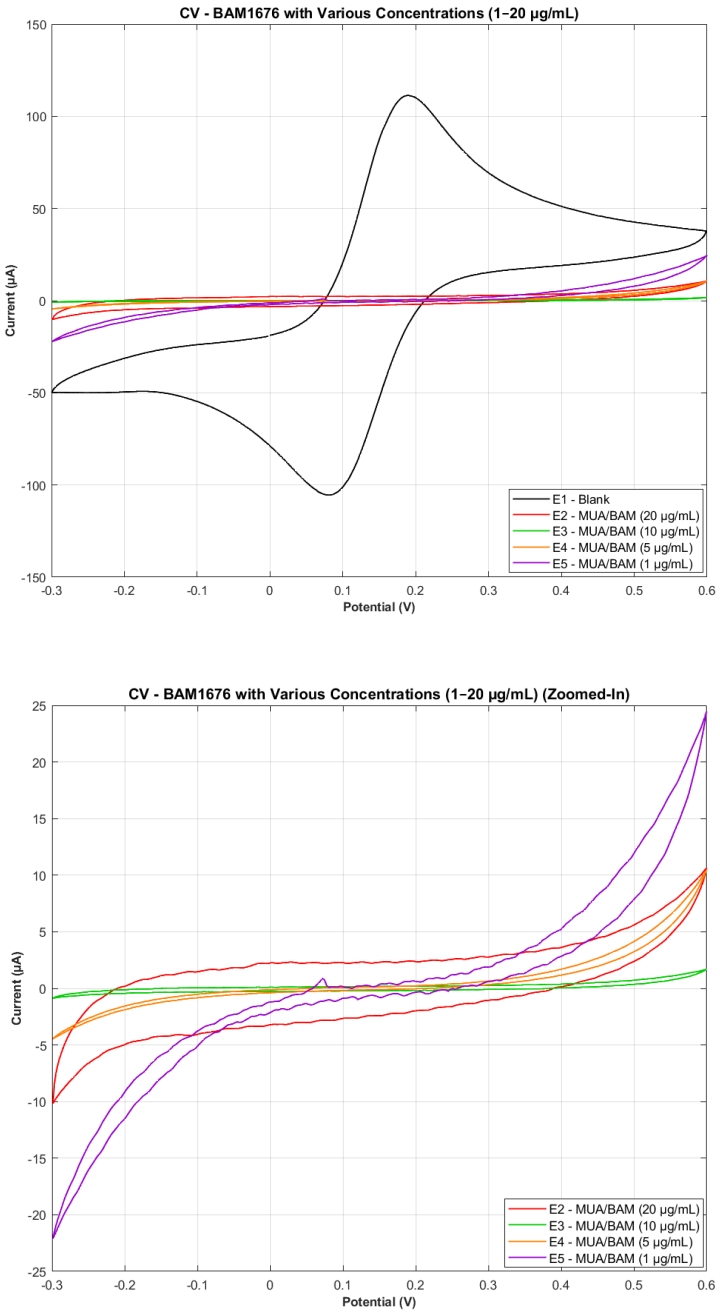

Figure 5.7: Voltammogram from CV Test on MUA-functionalised SPGEs after BAM1676-Immobilisation at Various Concentrations (Before Strep-HRP). Settings: potential sweep: 0.6 V to -0.3 V, potential step: 0.002 V, scan rate: $0.1\,V \cdot s^{-1}$, number of scans: 5. Ferri/ferrocyanide (3 mM) was utilised as the redox probe. The CV voltammogram represents CV profiles of BAM-modified SPGEs with various antibody concentrations. Black: blank SPGE, purple: SPGE/MUA/BAM (1 μg/mL), orange: SPGE/MUA/BAM (5 μg/mL), green: SPGE/MUA/BAM (10 μg/mL), and red: SPGE/MUA/BAM (20 μg/mL). **Bottom:** A zoomed-in view of the above CV.

layer was subsequently verified by conducting CV tests with the same settings and conditions as in Method 1. From the CV voltammogram in Figure 5.7(top), the blank SPGE (black) displays a characteristic duck-shaped CV profile with distinct redox peaks. This aligns with expectations, as the blank electrode surface can freely interact with the ferri/ferrocyanide ions in the solution. The electrodes with MUA/BAM functionalised surfaces, show very flat CV profiles, even at low concentrations. However, when looking closely at the CV curves in Figure 5.7(bottom), a trend can be observed where higher antibody concentrations result in increasingly decreased redox activity, as can be seen from the CV profiles of MUA/BAM with 20μg/mL (red) and 10μg/m (geen). In contrast, lower antibody concentrations, MUA/BAM with 1μg/mL (purple) in particular, exhibits slightly higher current responses. The CV response of the electrode functionalised with 1 μg/mL (purple) exhibits a higher peak current, reaching approximately -22μA. In contrast, electrodes with higher BAM concentrations, such as MUA/BAM 20μg/mL) and MUA/BAM (10μg/mL), show significantly lower peak currents down to values around -10 μA and -1 μA, respectively, as can be seen in the zoomed-in image. The overall small current responses are to be expected, since the addition of MUA alone adds a significant insulating effect on the electrode surface, as discussed extensively in Method 1. Moreover, antibodies, much like Streptavidin, are bulky structures with no intrinsic conductive pathways (as opposed to e.g. HRP enzymes, which have heme centres that render the enzymes intrinsically conductive). Consequently, the antibodies act as an extra insulating layer[82] (albeit at a smaller scale), hindering electron transfer further. Possible reasons for this could be 1) their bulky structure results in the extension of the electron tunnelling pathway, 2) their sheer size renders it difficult for redox probes to access the electrode surface, and 3) high concentrations of antibodies can create an extra insulating layer consisting of densely packed antibodies, making it almost impossible to pass electrons to and from the electrode surface. However, due to the high specificity nature of antibodies, in the presence of its antigen or a redox mediator (e.g. Streptavidin-HRP conjugate), the immobilised antibody can contribute to the current generation. This aligns well with the voltammogram, where, in the absence of Strep-HRP (redox mediator), the CV profiles of the BAM-modified electrodes remain flat, indicating a lack of electrochemical activity.

Following the CV verification of successful SAM formation and binding of antibodies, EIS tests were conducted to further investigate the charge transfer kinetics of the system. The EIS test conditions and settings were the same as in Method 1. Figure 5.8 shows the Nyquist plots from the EIS test, while Table 5.2 shows the corresponding R_{CT} values. Similar to the Nyquist plots of Method 1 (Figure 5.4), the electrodes with a SAM of MUA exhibit remarkable R_{CT} compared to the electrodes with MUA and BAM. This further supports the overall trend seen throughout this project, that the MUA layer causes an outstanding increase in R_{CT} experienced by the electrode. This is also clear from Table 5.2, where the charge transfer resistance of the MUA step is

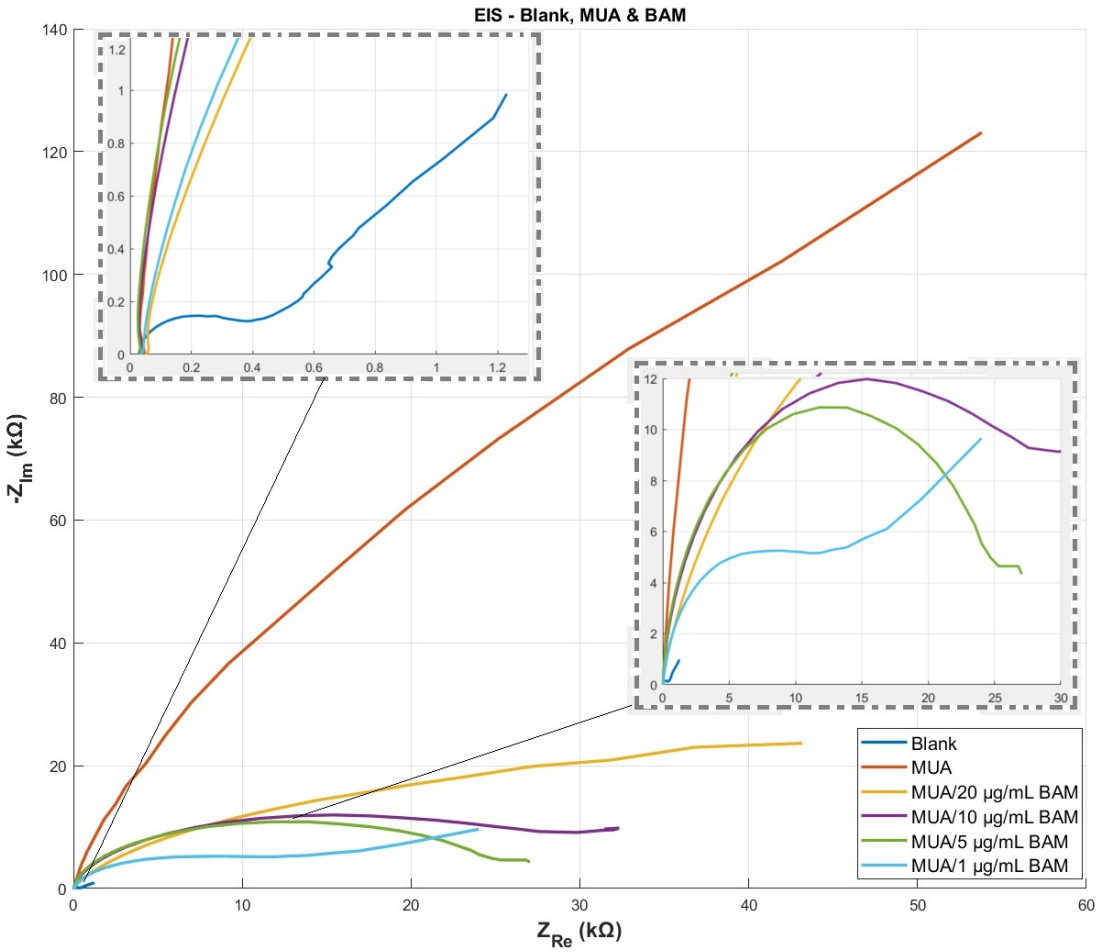

Figure 5.8: Nyquist Plot from EIS Measurements on SPGEs after Functionalisation with MUA and BAM1676 at Four Different Concentrations. Settings: E(dc)=0.75 V, E(ac)=0.01 V, freq. range: 0.1 Hz to 100.000 Hz. **Left insert:** zoom-in of blank SPGE. **Right insert:** zoom-in of SPGE/MUA/BAM (1 μg/mL). The measurements were done in 3 mM ferri/ferrocyanide. Blue: blank SPGE, red: SPGE/MUA, yellow: SPGE/MUA/BAM (20 μg/mL), purple: SPGE/MUA/BAM (10 μg/mL), green: SPGE/MUA/BAM (5 μg/mL), and cyan: SPGE/MUA/BAM (1 μg/mL).

Table 5.2: The Charge Transfer Resistance at each Functionalisation Step. The values were extracted by fitting the experimental EIS data to Randles circuit model in the PSTrace v5.10 software from PalmSens.

Functionalisation Step	R_{CT} [kΩ]
Blank	0.306
MUA	3064
MUA/BAM (1 μg/mL)	11.08
MUA/BAM (5 μg/mL)	22.57
MUA/BAM (10 μg/mL)	26.59
MUA/BAM (20 μg/mL)	24.93

almost 100x bigger than those of the BAM-modified electrodes. Next, by comparing the Nyquist plots of the four electrodes with varying antibody concentration, it can be seen that the impedance increases with increasing antibody concentration, which is in accordance with the CV test results seen above (Figure 5.7). This is reasonable, considering higher concentrations of antibodies at the electrode surface can create an insulating layer (in addition to the SAM layer) for the reasons presented earlier. Consequently, the charge transfer resistance experienced by the electrode increases as well.

Finally, when comparing EIS data from Method 1 (Figure 5.4 and Table 5.1) with the EIS data from Method 2 (Figure 5.8 and Table 5.2), taking into consideration that all three biomolecules are (ideally) covalently attached to the MUA layer, it is observed that the BAM-modified electrodes experience less R_{CT} relative to both the HRP-modified electrodes and Strep-HRP-modified electrodes . In Method 1, it was found that for enzyme-modified electrodes, higher concentrations (and thus lower dilutions, e.g. 1:20 dilution) result in lower impedance, which was contrary to expectations. This could be due to a number of reasons: as already discussed earlier, very high concentrations of MUA, can cause increased insulating effects on the electrode surface, leading to increased R_{CT}. Adding to this a poor conductive redox system, or low concentrations of these, results in slow electron transfer and eventually electron build-up at the interface and increased R_{CT}. In Method 2, however, the opposite is true for BAM-modified electrodes, where higher concentrations result in higher impedance. This is in accordance with expectations, and is a trend that is also observed in the study by Pedersen et al.[5]. However, the lower R_{CT} values seen for BAM-modified electrodes compared to HRP-and Strep-HRP- electrodes does not align with expectations. Owing to the structural and intrinsic properties of the antibodies (e.g. steric hindrance and non-conductive nature) and the enzymes (HRP conductive and less bulky), it would be expected that the enzyme-modified electrodes would experience less R_{CT} as it would have higher current responses. One possible reason could be insufficient washing/rinsing between each functionalisation step in Method 1, leading to higher concentrations of surface species and thus higher impedance signals. This was rectified in Method 2, where the electrode surfaces was rinsed thoroughly between each functionalisation step, which could potentially have resulted in lower impedance signals due to less crowding at the electrode surface (i.e. removal of excess/unbound species). Lastly, from the EIS data in Method 2, it is evident that the electrochemical activity at the electrode-electrolyte interface is governed by electron transfer kinetics, as was also observed in Method 1.

After running the EIS tests, Strep-HRP was added to the electrodes and a second CV test was performed. The resulting voltammograms presented in Figure 5.9 exhibit a sigmoidal shape, consistent with previous observations and distinct from the blank electrode. A comparison of the CV curves before (Figure 5.7) and after (Figure 5.9) the addition of Strep-HRP reveals a slight decrease in current response across all concen-

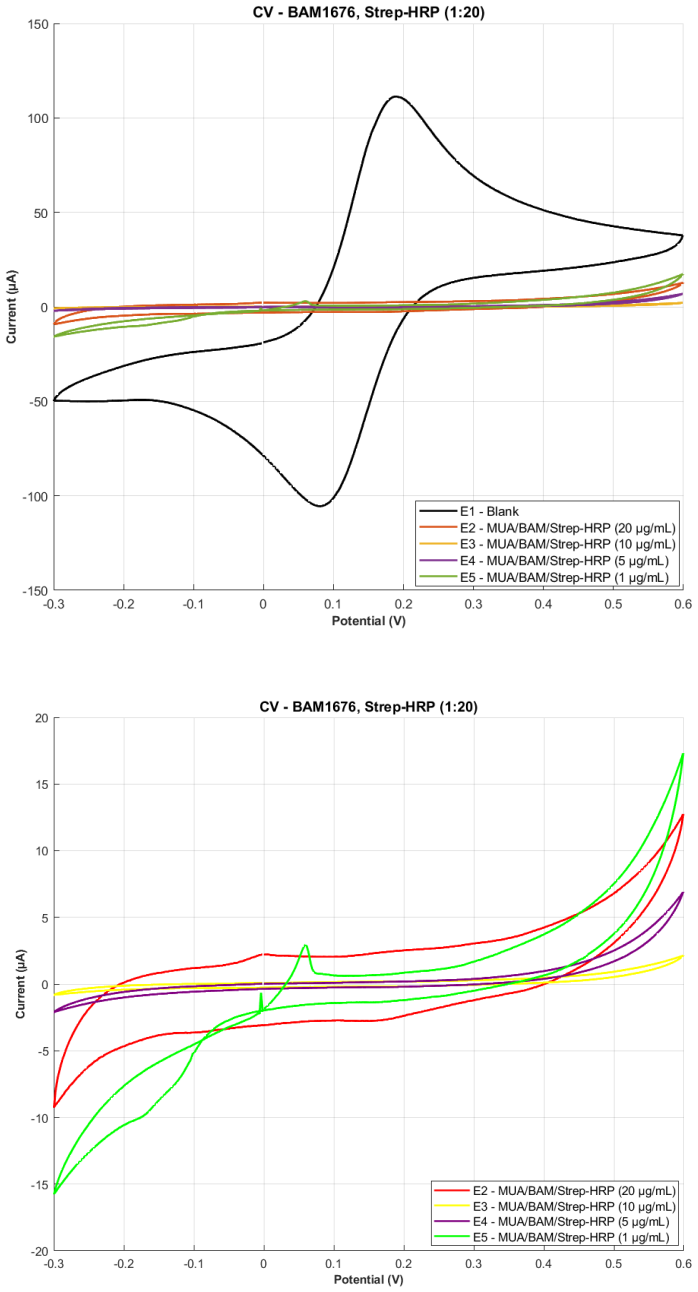

Figure 5.9: Voltammogram from CV Measurements on MUA-functionalised SPGEs after BAM1676-Immobilisation at Various Concentrations (After Strep-HRP). Settings: potential sweep: 0.6 V to -0.3 V, potential step: 0.002 V, scan rate: $0.1\,V \cdot s^{-1}$, number of scans: 5. Ferri/ferrocyanide (3 mM) was utilised as the redox probe. The CV voltammogram represents CV profiles of BAM-modified SPGEs with various antibody concentrations. Black: blank SPGE, green: SPGE/MUA/BAM (1 μg/mL), purple: SPGE/MUA/BAM (5 μg/mL), yellow: SPGE/MUA/BAM (10 μg/mL), and red: SPGE/MUA/BAM (20 μg/mL).**Bottom:** A zoomed-in view of the above CV.

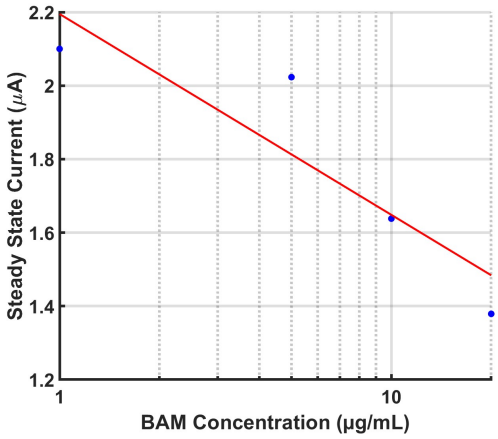

Figure 5.10: Log Linear Plot of Steady State Current vs. Antibody Concentration.

trations as seen in the zoomed-in image. This reduction suggests that BAM is effectively immobilised, as the current decreases further following the introduction of Strep-HRP.

As the last step in Method 2, CA tests were conducted to investigate the antibody specificity and the relationship between antibody concentration and electrochemical response of the system. Thus, two CA tests were conducted: one before adding Strep-HRP and the other after adding Strep-HRP. The I-t plots from the CA tests can be seen in Figure 5.11, where the top panel shows the CA measurements before the addition of Strep-HRP, while the bottom panel shows the measurements after its addition. A comparison of these two plots shows that the addition of Strep-HRP significantly influences the current response of the functionalised SPGEs. Before the introduction of Strep-HRP, as shown in the top panel, the current response remains relatively low across all BAM concentrations, with the MUA/BAM (20μg/mL electrode having the highest current response. In contrast, after introducing Strep-HRP (bottom panel), a notable increase in current is observed for all BAM-modified SPGEs, which demonstrate the catalytic effect of the enzyme. A more negative current (and thus reduction of the electrode) indicates that a greater amount of TMB is being oxidised by Strep-HRP, leading to enhanced electron transfer. This suggests that the enzymatic reaction is proceeding efficiently, with higher oxidation of TMB resulting in a stronger negative current response. Furthermore, the blank electrode exhibits the lowest current response, while the BAM-modified SPGEs display a concentration-dependent trend.

Specifically, as the concentration of BAM decreases, the current response also diminishes. This suggests that lower BAM concentrations result in reduced Strep-HRP binding and, consequently, a lower current response. This trend confirms the successful binding between BAM antibodies and Strep-HRP, where the observed current response is directly correlated to the concentration of enzymes. This concentration-

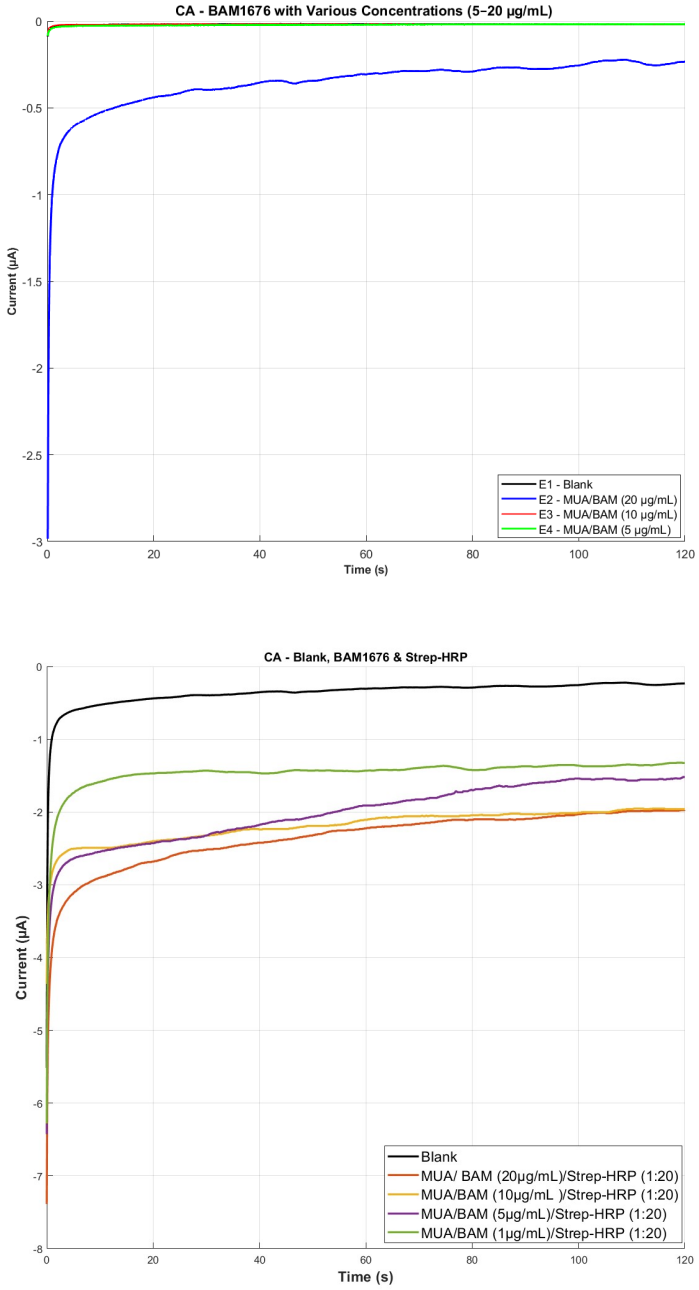

Figure 5.11: Current vs. time Plots From CA Measurements on SPGEs Functionalised with MUA, BAM1676, and Strep-HRP (1:20). Settings: t. eq.=0 s, E(dc)=0.0 V, t.interval=0.1 s, t.run=120 s. 1-Step™Turbo TMB-ELISA Substrate Solution was used as the redox mediator. **Top:** Before addition of Strep-HRP. Black: blank SPGE, blue: SPGE/MUA/BAM(20μg/mL), red: SPGE/MUA/BAM(10μg/mL), green: SPGE/MUA/BAM(5μg/mL). **Bottom:** After addition of Strep-HRP. Red: MUA/BAM(20μg/mL)/Strep-HRP, yellow: MUA/BAM (10μg/mL)/Strep-HRP, purple: MUA/BAM(5μg/mL)/Strep-HRP, and green: MUA/BAM(1μg/mL)/Strep-HRP.

dependent trend also shows that adding Strep-HRP makes the biosensor more specific due to the strong binding affinity between Streptavidin and biotin. Based on this, the reliability and specificity of the biosensor setup in Method 2 is greatly enhanced. The concentration-dependence of this biosensor setup is further confirmed by Figure 5.10, where a log-linear plot of steady state current vs BAM concentration (in μg/mL) is shown. Here, the x-axis represents the BAM concentration on a logarithmic scale (ranging from 1 to 20 μg/mL), while the y-axis corresponds to the steady state current (in μA). The data points in the log plot are extracted from the steady state region of the CA plot. The plot shows a negative linear trend, indicating that as the concentration of BAM increases, the measured steady state current decreases.

5.3 Method 3: Click Chemistry

In this method, the click chemistry technique was conducted. For this purpose, a novel protocol was developed and can be seen in Appendix A. Here, SPGEs were once again functionalised with a MUA SAM and subsequently activated by EDC/NHS chemistry. Next, alkynes were immobilised onto the MUA layer through covalent bonds (amide bond), followed by the addition of azide-antibody (biotinylated) conjugates. This last addition completes the click reaction, forming the alkyne-azide bond through the formation of a triazole ring. The click reaction was further catalysed by Cu(I) ions generated by the electrochemical reduction of $CuSO_4$. A schematic overview of this method can be seen in Figure 3.1. Furthermore, all electrodes were cleaned with all three cleaning steps (one mechanical step and two electrochemical steps) prior to testing.

By extension, it should also be noted that throughout the entire project period, the same electrodes were extensively and continuously employed, having already been used prior to this project. By the final experiments, their repeated usage, including multiple cycles of functionalisation, cleaning, and testing, resulted in diminished electrochemical performance. This can be seen from the CV voltammograms presented in Figure 5.12, where the top panel shows the CV curves of electrodes post-cleaning steps (1-3) from Method 1, and the bottom panel shows the electrodes post-cleaning steps (1-3) right before Method 3 experiments. Reading the CV plots from Method 1 (A), the average (reduction) current response spans from $\sim$600 μA to $\sim$600 μA. Comparing this with the CV plots obtained right before Method 3 experiments (B), the current response is almost halved; on average, the current response spans $\sim$200 μA to $\sim$400 μA. This is a significant decrease in current response, and consequently, the electrochemical performance of the SPGEs, potentially leading to distortions of measurements.

5.3.1 Functionalisation Tests

Given the novelty of this method and time constraints, the click reaction was performed only once. Consequently, it was not possible to run all three electrochemical

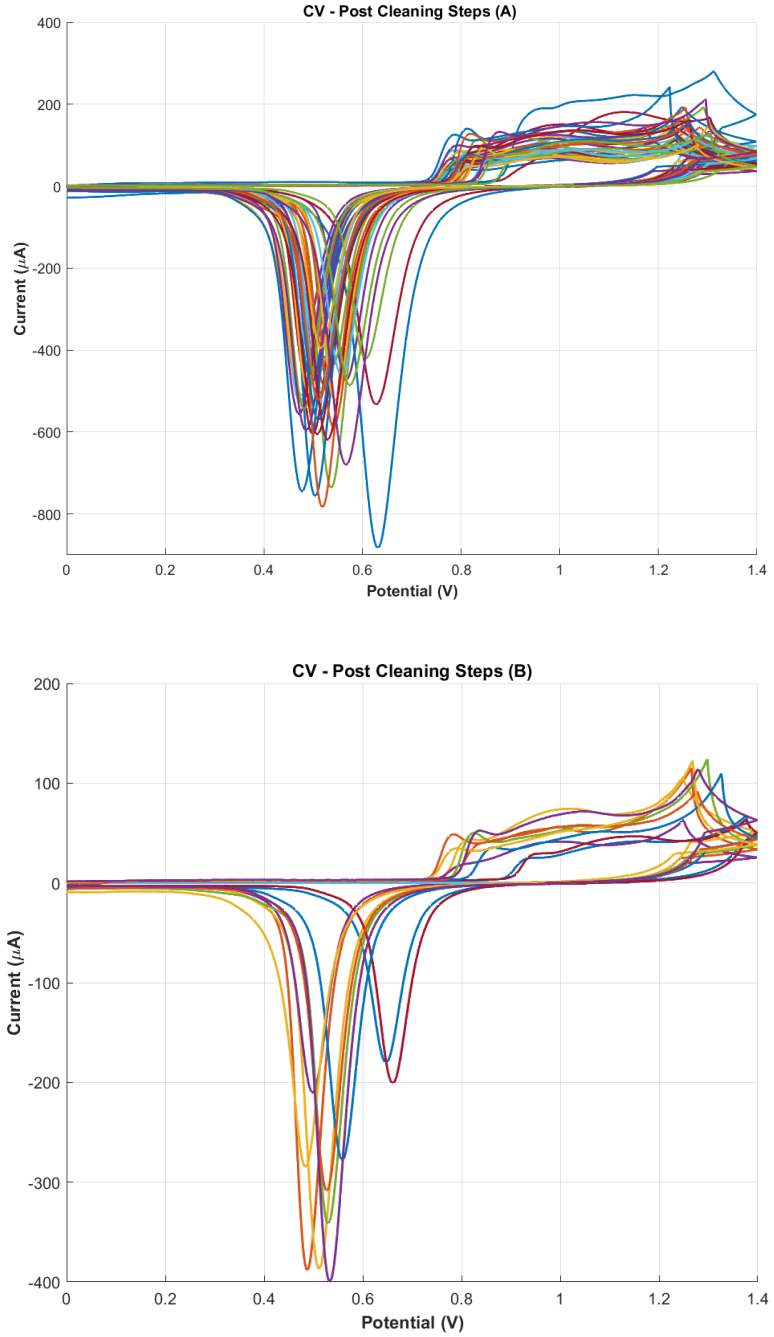

Figure 5.12: CV Measurements after Cleaning Steps (1-3) in Method 1 (top) Compared to Method 3 (bottom). These plots present the post-cleaning CV profiles of electrodes cleaned for Method 1 and Method 3. The first step of the cleaning procedure involved mechanical polishing with 3 μm grain size for 2 minutes, followed by a two-step electrochemical cleaning process (step 2 and 3). Step 2 was performed with CA at 1.4 V for 30 s, using 150 mM PBS, while Step 3 was performed with CV using 50 mM H_2SO_4 and scanning from 1.4 V to -0.1 V for 10 cycles at 100 mV/s.

tests (i.e. CV, EIS, and CA) for the functionalisation steps. Furthermore, Method 1 and 2 served as test runs and laid the foundation for Method 3, both in terms of investigating the electrochemical performance of the SPGEs and the effect of different parameters during the electrochemical tests. Conducting Method 1 and 2 was therefore crucial, to establish a good foundation and understanding of the process for Method 3. The objective in Method 3 was to develop and optimise a novel protocol for a CuAAC-based immunosensor. In order to develop a working protocol for the electro-click reaction, a series of preliminary tests were carried out. These preliminary tests include: **Preliminary Test 1.** determining the optimal $CuSO_4$ concentration and reducing potential for generation of Cu(I) ions and **Preliminary Test 2.** determining the optimal time to generate the Cu(I) ions and adding the azide-antibody conjugate, respectively.

In **Preliminary Test 1**, six different concentrations (1 μM, 10 μM, 100 μM, 1 mM, 2 mM, and 10 mM) were tested in PBS, PBS with 10% DMSO, and 0.5 M NaCl. It was found that the optimal $CuSO_4$ concentration and solvent was 1 mM $CuSO_4$ in 0.5M NaCl. That is, at higher concentrations, 2 mM and 10 mM, high amounts of precipitation occurred on the electrode surface and was also difficult to dissolve in PBS or PBS with 10% DMSO. This is likely due to the formation of in-soluble $Cu_3(PO_4)_2$ ions. For these preliminary tests, it was desirable to start with the highest concentrations possible without disrupting or affecting the electrochemical activity. Based on this, the two highest concentrations (2 mM and 10 mM) and the three lowest concentrations (1 μM, 10 μM, and 100 μM,) were excluded. Next, CV measurements were performed to determine the optimal $CuSO_4$ reduction potential, which was found to be 160 mV in the the potential range of 0.6 V to -0.2 V. The CV settings for this measurement can be seen in Table 4.7.

In **Preliminary Test 2**, two distinct approaches were tested. In **Approach 1**, the electro-click reaction was performed via a two-step process. In the first step, Cu(I) ions was generated using the settings found in **Preliminary test 1** (1 mM $CuSO_4$ in 0.5 M NaCl, reduction potential of 160 mV). In the second step, the azide-antibody conjugate was added immediately and the electrochemical activity was measured via CA. In the second approach, **Approach 2**, the electro-click reaction was performed in the same step, followed by a CA measurement.

In Figure 5.13 (top), the CA measurements from both approaches are presented. The control experiment (black), where the azide-antibody conjugate was omitted, exhibits the lowest current response, whereas both functionalised electrodes (blue and red) demonstrate a more pronounced negative current response. This confirms that the click reaction has indeed occurred, as the increased negative current indicates that TMB has been oxidised, leading to the reduction of the electrode surface. As a result, more negative current is generated, demonstrating successful immobilisation of azide-antibody via the click reaction.

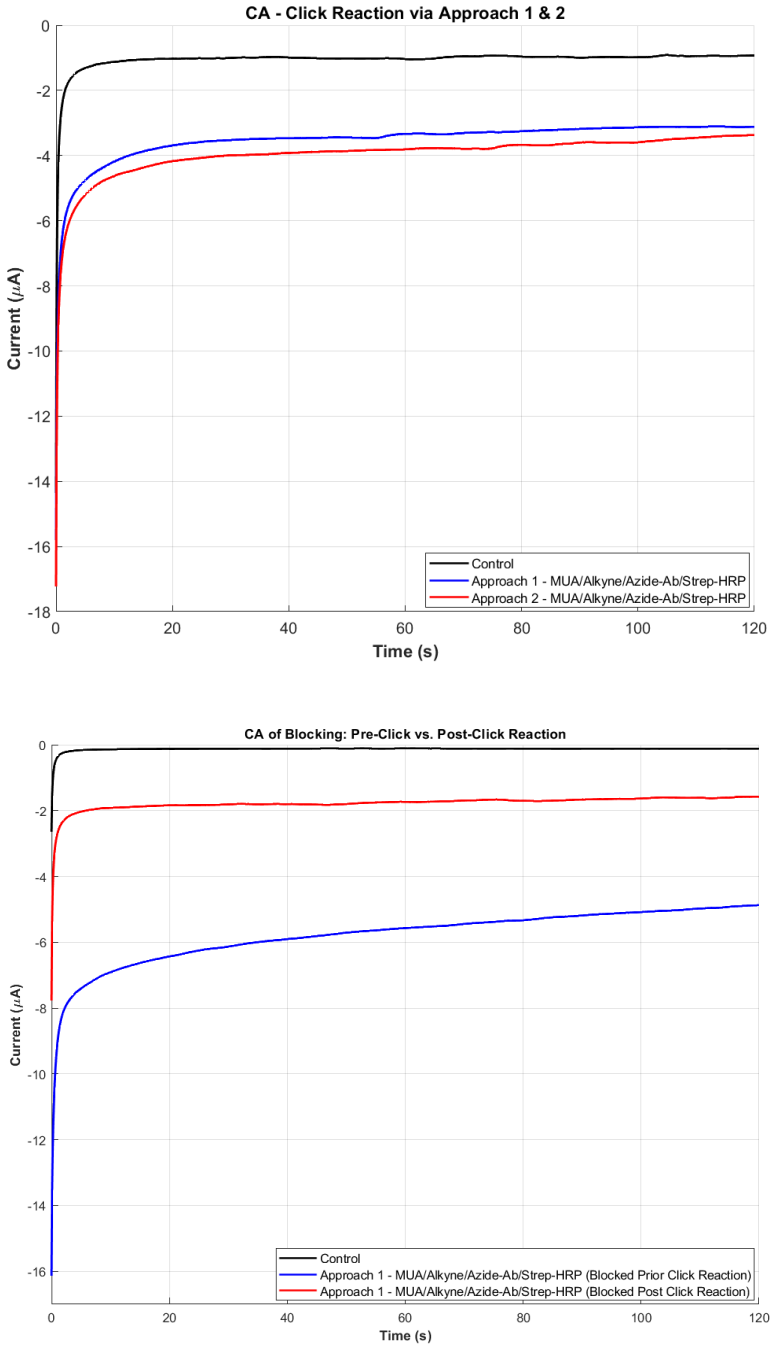

Figure 5.13: Current vs. time Plots From CA Measurements on CuAAC-based SPGEs Without (top) and With (bottom) Surface Blocking. Settings: t. eq.=0 s, E(dc)=0.0 V, t.interval=0.1 s, t.run=120 s. 1-Step™Turbo TMB-ELISA Substrate Solution was used as the redox mediator. Approach 1: electro-click reaction via a two-step process and Approach 2: electro-click reaction in one single step. **Top:** CA plots of the two approaches without surface blocking. Blue: Approach 1, red: Approach 2. **Bottom:** CA plots of Approach 1 with surface blocking before (blue) and after (red) electro-click reaction.

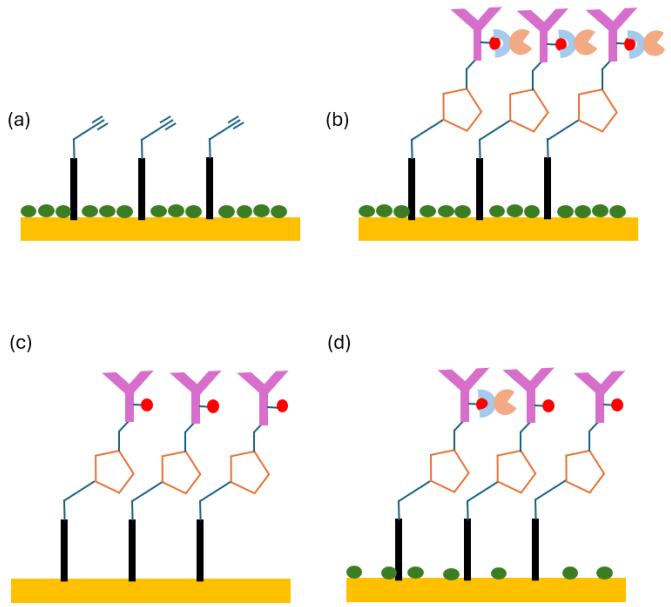

Figure 5.14: Illustration of Addition of Blocking Agents Prior/Post Click Reaction. Green circle: blocking agents, red circle: biotin, pentagons: alkyne-azide triazole ring, blue strucure: Streptavidin, orange structure: HRP. **a,b)** Here the blocking agents are added prior to click reaction, leading to enhanced specific binding and increased current response. **c,d)** blocking agents are added after click reaction, leading to more non-specific binding and lower current responses.

Morover, it can be seen from the plots for Approach 1 and 2 (blue and red), that the timing of Cu(I) generation has minimal impact on the electrochemical activity, as both approaches exhibit nearly identical current responses. This suggests that Cu(I) is effectively generated in both cases, allowing the click reaction to proceed efficiently, provided that the azide-antibody is added immediately after Cu(I) generation in Approach 1. The pronounced negative current in both approaches confirms catalytic activity, supporting the successful formation of the CuAAC-based electrodes.

Now that the occurrence of the click reaction has been confirmed, with both approaches yielding comparable current responses, the next step involved implementing a blocking step during the functionalisation process to minimise non-specific binding on the electrode surface and further enhance specificity. In this project, the electrode surface was blocked with cysteamine and 1% PEGDA with 0.05% Irgacure solution. The cysteamine binds to the Au surface through covalent thiol bonds, ensuring any spots not occupied by MUA are covered. Next, the PEGDA-Irgacure solution was added, forming a thin passivation layer initiated by Irgacure after UV-exposure. This creates an robust anti-fouling layer whichh prevents any un-specific interactions with the electrode surface. This ensures and enhances the specific binding between the click chemicals, i.e. the alkyne and the azide-antibody conjugate. To determine the optimal timing for introducing the blocking agent, either before or after the click reaction, an

additional experiment was conducted, and the results are presented in Figure 5.13. In the plot, the blue curve represents the current response when the blocking step was applied prior to the click reaction, specifically immediately after the deposition of the alkyne layer onto the electrode. Conversely, the red curve corresponds to the current response when the blocking step was introduced following the click reaction. The black curve serves as the control, representing measurements conducted without the addition of the azide-antibody.

From the plots, it can be seen that the blue curve, where blocking was performed before the click reaction, exhibits substantially more negative current compared to the red curve, where blocking was applied post-click reaction. This suggests that implementing the blocking step prior to the click reaction facilitates more efficient functionalisation, likely by preventing non-specific adsorption and ensuring improved attachment of the azide-antibody. In contrast, performing the blocking step after the click reaction may partially hinder reaction efficiency or reduce the availability of active sites, thereby resulting in a lower current response. A schematic representation of the two methods can be seen in Figure 5.14.

The next step was to investigate the effect of surface blocking on the concentration-dependent response of azide-antibody immobilisation. To achieve this, two experimental conditions were tested: one set of measurements was conducted without a blocking step, where the concentration of azide-antibody was varied, while another set included a blocking step after the click reaction. This approach allowed for the assessment of how surface blocking influences the current response and the efficiency of antibody immobilisation. These CA results are presented in Figure 5.15. Overall, both experimental conditions exhibit the same general trend: the current response increases with increasing azide-antibody concentration. A notable observation is the degree of separation between the current responses at different concentrations, which is less pronounced in the experiment without surface blocking. Apart from this, no significant differences are observed between the two plots. This outcome is likely attributed to the same factors identified in Figure 5.14, where post-click blocking was found to be less effective in preventing non-specific interactions.

Overall, the results from Method 3 show promising results, particularly due to the successful functionalisation of SPGEs using CuAAC. However, further experiments are required. This includes repeating the blocking step, but prior to click reaction. This would allow for a direct comparison of blocking efficiency and its impact on current response.

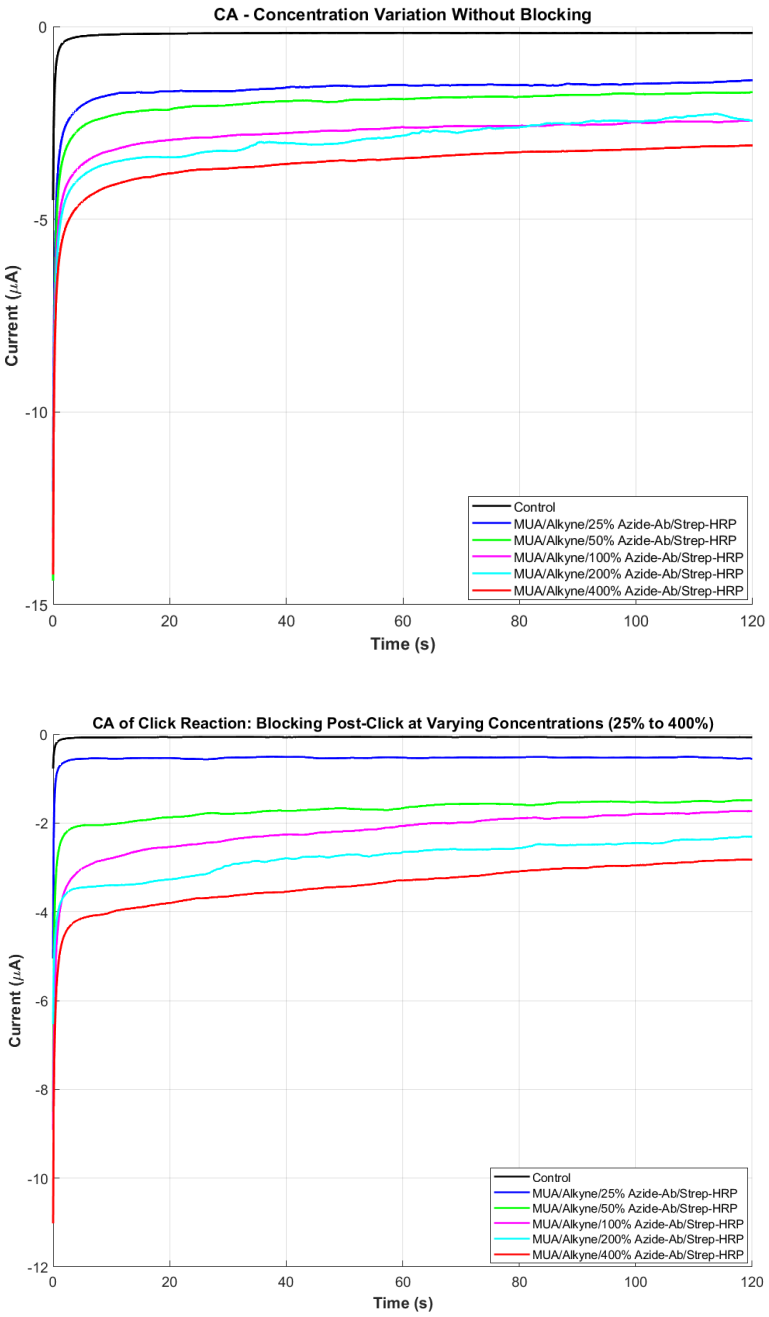

Figure 5.15: Current vs. time Plots From CA Measurements on CuAAC-based SPGEs Without (top) and With (bottom) Surface Blocking and Varying Azide Concentrations. Settings: t. eq.=0 s, E(dc)=0.0 V, t.interval=0.1 s, t.run=120 s. 1-Step™Turbo TMB-ELISA Substrate Solution was used as the redox mediator. Blue:25% azide, green: 50% azide, pink: 100% azide, cyan:200% azide, red: 400% azide. **Top:** CA plots of Approach 1 without surface blocking and with varying azide concentrations. **Bottom:** CA plots of Approach 1 with surface blocking after electro-click reaction and with varying azide concentrations.

5.4 Modelling of Biosensor System in COMSOL

In this project, one of the key objectives was to simulate the various stages of the functionalisation process of the biosensor platform to gain a deeper understanding of the system's behaviour. This was achieved by systematically investigating different aspects of the system using computational modelling. The proposed model integrates studies from the literature to develop a simulation framework using the latest add-in functionalities available in COMSOL Multiphysics®. The model studies CV carried out at SPEs in the presence of ferri/ferrocyanide ($Fe(CN)_6]^{3-/4-}$). Finite Element Analysis (FEA) is carried out using COMSOL Multiphysics®. The model can also be extended to more complex biosensors containing multiple working electrodes, aiding in the design and optimisation to prevent cross-contamination or cross-reactions, and enabling the detection of multiple species simultaneously. System-level simulations of the electrical responses of biosensors, such as CV, are complex to model. They require precise identification of dominating microscopic mechanisms, definitions of synergies in Multiphysics models, proper calibration of material-related parameters, and specific equivalent circuits for signal generation and conditioning, such as Potentiostats. In this project, the aim was to expand the understanding of electrochemical phenomenon modelling, emphasising the need for structured multiphysics to simulate the complexities of electrochemical sensor processes. A customised COMSOL Multiphysics® model is introduced for simulating CV in electrochemical biosensors. The proposed simulations consider the dominating chemical and electrical processes involved with a redox couple diluted in an electrolyte solution. The electrochemical reaction mechanism that occurs during the CV is described as:

$$[Fe(CN)_6]^{3-} + e^- \leftrightarrow [Fe(CN)_6]^{4-}$$

This is triggered by the application of an electric potential range on the WE, leading to a current generation during the transfer of electrons across the electrode-electrolyte interface.

The simulation model was replicated based on the 3D geometry of the actual electrode model used during the experimental part of the project, which is the Metrohm DropSens 220BT. The structure includes the substrate, three electrodes, metal interconnections, contact areas, and an isolation layer (to prevent short-circuiting during an electrochemical reaction). The solution drop is modelled as a semi-sphere with a 4 mm radius, and the electrodes have a thickness of 100 μm. There might be slight differences when compared to a physical biosensor since some parameters are estimated.

When a droplet of ferricyanide is applied to a SPE, a series of electrochemical processes unfold. Initially, the ferri/ferrocyanide droplet undergoes a redox reaction at the WE upon the application of a potential. This reaction generates a measurable current, indicative of the analyte's concentration. The RE plays a crucial role by providing a stable and consistent reference potential, ensuring the accuracy and reliability of the

measurement. Meanwhile, the CE facilitates the flow of current through the circuit, completing the electrochemical process. This coordinated setup enables the detection and quantification of various analytes based on their distinct electrochemical properties, making SPEs a valuable tool in analytical chemistry and biosensing application.

To simulate the electrochemical reaction involving a ferri/ferrocyanide droplet and the electrodes, a mesh was generated for both components. A triangular mesh was specifically applied to the top layer of the electrodes, as this layer is directly involved in the electrochemical reaction. The electrodes were designed with a minimum element size of 5.5×10^{-7} metres and an element growth rate of 1.1 in the initial model. The curvature factor and narrow region resolution were set to 0.2 and 1, respectively. For the ferri/ferrocyanide droplet, a standard tetrahedral mesh was utilised to ensure accurate discretisation. The electrodes were given a fine mesh to capture the details of the electrochemical reaction. The top layer of the electrodes, which plays a crucial role in the reaction, was given a triangular mesh for better accuracy. Meanwhile, the ferri/ferrocyanide droplet is discretised using a tetrahedral (3D triangular) mesh to model its behaviour effectively.

Several important assumptions are made when simulating CV in the COMSOL Electroanalysis module. It is assumed that the electrolyte contains a significant amount of inert supporting electrolyte, which helps maintain a constant ionic strength and minimises migration effects, focusing the analysis on diffusion and convection (Supporting Electrolyte). Ohmic losses, or the potential drop due to solution resistance, are considered negligible to ensure accurate measurements. The electrochemical kinetics at the electrode surface are often modelled using standard theories like Butler-Volmer kinetics. Mass transport of electroactive species is governed by the diffusion-convection equation, incorporating diffusion, migration (when coupled with an electric field), and convection (when coupled with fluid flow). The electrode surface is assumed to be uniform and well-defined, simplifying the modelling process. In some scenarios, steady-state conditions are assumed, meaning the system has reached a stable state where concentrations of species and current remain constant over time. These assumptions streamline the complex nature of electrochemical systems, making simulations more manageable while still providing valuable insights into the system's behaviour.

During the simulation, the properties of both the materials and the solutions are derived from pre-existing data sources. This involves taking known information about the chemical and physical characteristics of the substances involved and inputting it into the simulation. These properties may include parameters such as conductivity, diffusivity, viscosity, and other relevant factors that influence the behaviour of the materials and solutions under study. Additionally, the studies rely on several assumptions and simplifications, such as negligible ohmic losses and uniform electrode surfaces. These assumptions may not always hold true in real-world scenarios, potentially leading to inaccuracies in the simulation results. The electrochemical kinetics

at the electrode surface are often modelled using standard theories like Butler-Volmer kinetics, which may not fully capture the non-linear and transient nature of the reactions.

The mass transport of electroactive species is governed by the diffusion-convection equation, incorporating diffusion, migration, and convection. Setting appropriate boundary conditions for the electrodes and the electrolyte can be challenging, and incorrect boundary conditions can lead to inaccurate results and misinterpretation of the electrochemical behaviour. Parameter sensitivity is another limitation, as the accuracy of CV simulations depends heavily on input parameters such as diffusion coefficients, reaction rates, and electrode properties. Small errors or uncertainties in these parameters can significantly affect the simulation outcomes.

Multiple computational models were developed to simulate CV, each designed to capture different aspects of the electrochemical response. By systematically evaluating various modelling approaches, an optimised framework was established to simulate the CV response under different conditions to provide a better understanding of the underlying electrochemical processes. This was achieved by investigating key parameters influencing the biosensor performance, including the size of the WE (geometrical aspect), concentration, scan rate, exchange current density and reactant concentration. The modelling was conducted in stages. The first stage aimed to develop a model that simulates CV using the ferri/ferrocyanide redox couple on a bare electrode, providing a baseline for understanding the fundamental electrochemical response. In the second stage, the model was improved, optimised, and extended to simulate the behaviour of functionalised electrodes, incorporating the effects of surface modifications on charge transfer and mass transport processes. Hence, the following sections present the results of the CV simulations for the bare electrode, followed by the results obtained from the model simulating the functionalised electrodes.

5.4.1 CV Model of Bare Au Electrode

Figure 5.16 presents the first CV simulation results from the initial 3D model for the bare electrode. The top plot shows the total current as a function of applied electric potential, displaying the characteristic voltammetric response of a redox-active system. The anodic and cathodic peak currents increase with higher scan rates, and the peak separation widens. The overall shape of the voltammograms follows the expected behaviour of a reversible electrochemical reaction, with oxidation and reduction peaks symmetrically positioned around the formal potential. However, the current magnitude in these simulations appears significantly lower than typically observed in experimental results.

The bottom panel depicts the applied electric potential as a function of time, where a triangular waveform is observed, corresponding to the potential sweep applied during CV. The duration of each sweep is directly affected by the scan rate, with slower

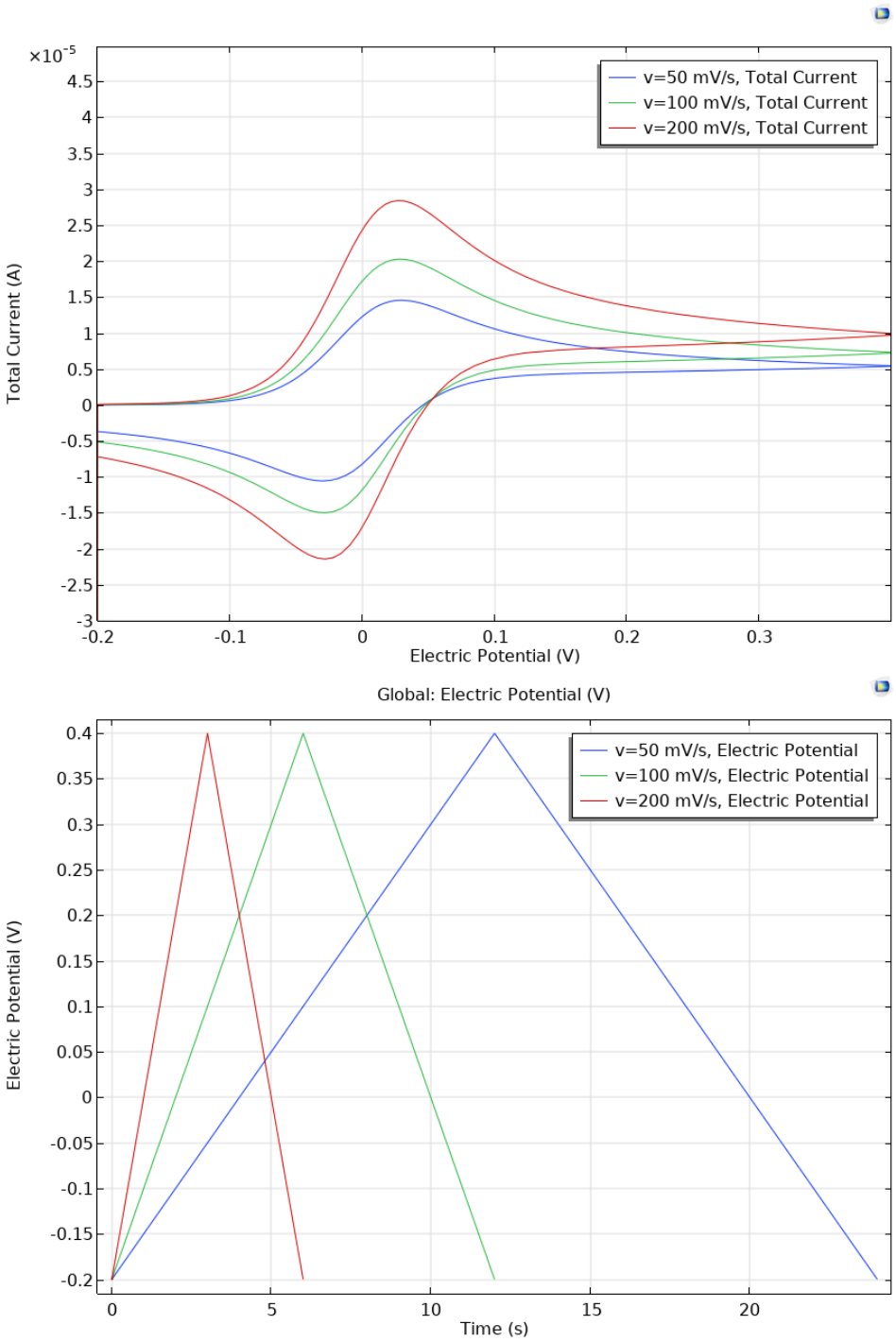

Figure 5.16: CV Simulation of a Bare Electrode. The plots show CV simulation results for a bare electrode at scan rates of 50 mV/s, 100 mV/s, and 200 mV/. The potential range is from is -0.2 V to 0.4 V. The top plot illustrates the simulated total current as a function of electric potential, displaying characteristic redox peaks. The lower plot represents the applied potential over time, showing a triangular waveform corresponding to the CV potential sweep.

scan rates (50 mV/s) taking longer to complete a full cycle, while higher scan rates (200 mV/s) result in faster potential reversals. This plot shows the direct relationship between scan rate and time, which confirms the correct implementation of the CV potential waveform in the simulation. These results clearly demonstrate that a redox reaction has occurred, as evidenced by the presence of well defined oxidation and reduction peaks in the voltammograms. To further investigate the impact of scan rate on the electrochemical system, a parametric sweep (50 mV/s, 100 mV/s, and 200 mV/s) was conducted on the bare electrode. However, the simulated signals are significantly lower than those observed in experimental data. The voltammograms at different scan rates, along with their corresponding potential sweeps, are shown in the plots. Although, the model capture the fundamental CV behaviour, the simulated current responses remain weaker than the experimentally obtained data. By systematically adjusting and optimising them one by one, the accuracy of the model can be improved. The initial simulation captures the overall trends of a CV response, indicating that the fundamental electrochemical behaviour is correctly represented.

To enhance the accuracy of the model and achieve a closer match with experimental data, further optimisations were performed by systematically analysing individual parameters to identify those with the greatest impact on the CV simulation. For these reasons, the methodology and data from previous studies, Bonaldo et al. [70] and Franchin et al. [9], were used as a reference to refine the simulation. These adjustments aimed to create a more realistic simulation of the biosensor behaviour. Several key parameters, including the diffusion coefficient, equilibrium potential, conductivity, electrolyte concentration, and C_{dl}, were incorporated to better represent experimental conditions. A series of parametric studies were conducted to assess the influence of each of these parameters on the CV response, revealing that the exchange current density, reactant concentration, scan rate, reaction rate constant had the most significant impact on the simulated voltammograms.

Figure 5.17 presents simulation results from an improved model, specifically analysing a potential sweep of concentration values. It demonstrates the CV response of a bare electrode interacting with the ferri/ferrocyanide redox couple $[Fe(CN)_6]^{3-/4-}$. The top panel displays the simulated CV curves alongside experimental data. The x-axis represents the applied potential in volts, ranging from -0.3 V to 0.6 V, while the y-axis shows the measured current, in microamperes, within the experimental range. Experimental data is depicted as black circular markers, while the simulated responses for different bulk concentrations of the redox species are represented by coloured lines: blue for 1 mM, green for 3.3 mM, and red for 5 mM. The characteristic oxidation and reduction peaks observed in these curves reflect the expected electrochemical behaviour of the system. Among the simulated results, the green curve (3.3 mM) aligns most closely with the experimental data which was performed at 3 mM, indicating that this concentration best represents the actual conditions of the experiment. The improved model effectively captures the electrochemical response, demonstrating its

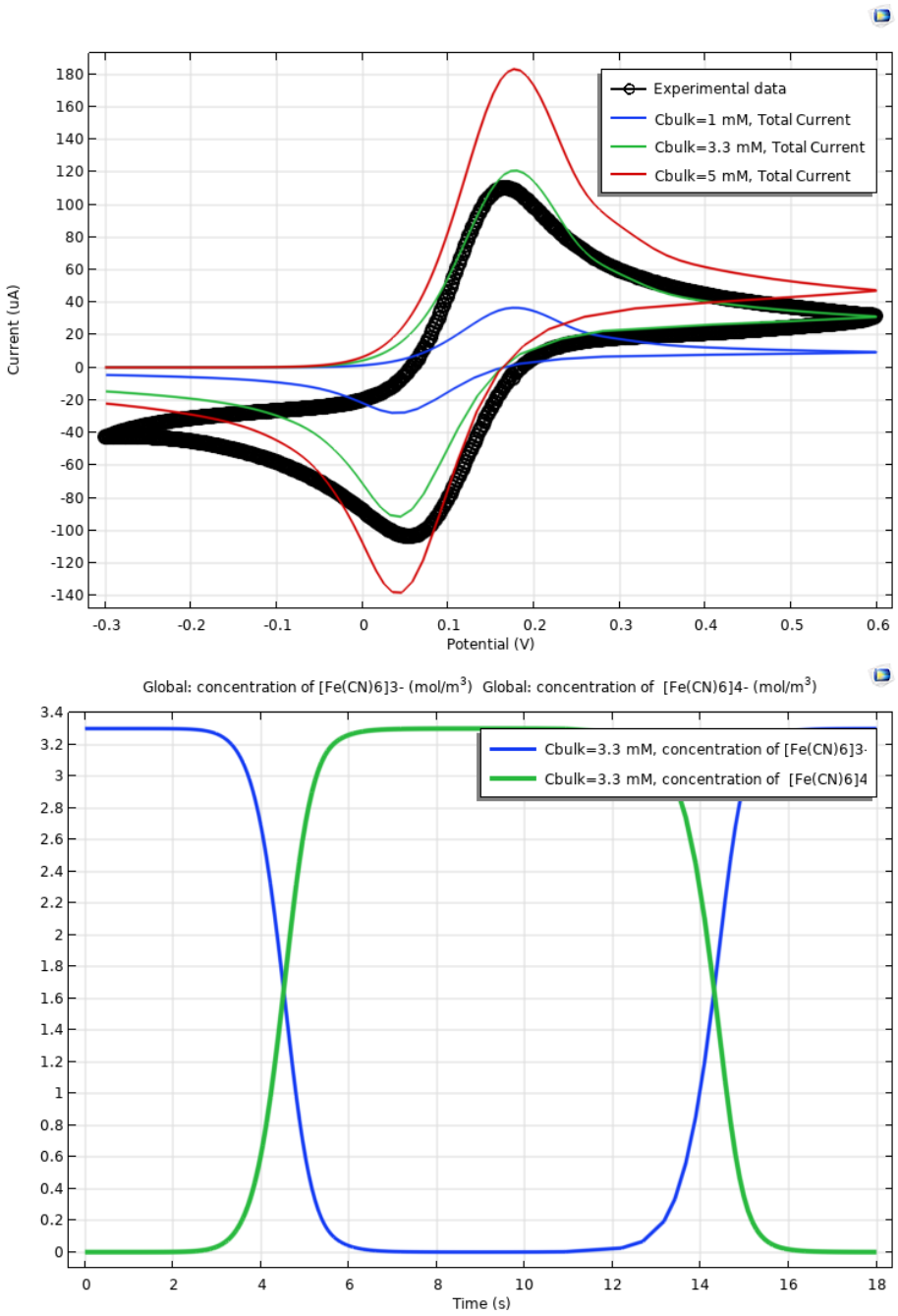

Figure 5.17: Concentration Variation of CV Simulation of a Bare Electrode. Simulation results from the improved model, showing the CV response of a bare electrode in the presence of the ferricyanide/ferrocyanide redox couple $[Fe(CN)_6]^{3-/4-}$. The concentration is varied from 1 mM up to 5 mM. The potential range extends from $-0.3V$ to $+0.6V$ at a scan rate of 100 mV/s. The applied parameters include an equilibrium potential of 110 mV, a double-layer capacitance $C_{dl} = 0.1\,(F/m^2)$, a standard heterogeneous rate constant $k_o = 0.01$, a transfer coefficient $\alpha = 5$, and a diffusion coefficient of $7 \times 10^{-6}\,(\mathrm{cm}^2/\mathrm{s})$. Bottom figure shows the time-dependent concentration variation of $[Fe(CN)_6]^{3-/4-}$.

accuracy in simulating the redox process. The bottom panel illustrates the time-dependent concentration variation of the redox species during the potential sweep. The x-axis represents time in seconds, spanning from 0 to approximately 18 seconds, while the y-axis shows the global concentration in mol/m^3. The blue curve corresponds to the concentration of $[Fe(CN)_6]^{3-}$, while the green curve represents $[Fe(CN)_6]^{4-}$. Initially, ferricyanide is present at a higher concentration, while ferrocyanide is nearly absent. As the potential is swept, ferricyanide undergoes reduction to ferrocyanide, leading to a decrease in its concentration and a corresponding increase in ferrocyanide concentration. This transition reverses as the potential sweeps back, completing the redox cycle. The improved model effectively captures these concentration fluctuations, confirming its accuracy in describing the electrochemical behaviour of the system.

The two concentration profiles shown in Figure 5.18 contain two graphs that illustrate the concentration variation of ferricyanide and ferrocyanide during the CV simulation of a bare electrode. The graphs show how the redox species interconvert at the WE over time, depending on different bulk concentrations. The top graph, titled "Concentration of Ferrocyanide produced during reduction," represents the change in ferrocyanide concentration at the WE over time as the reduction reaction progresses. The x-axis corresponds to time in seconds, ranging from 0 to 18 seconds, while the y-axis shows the concentration of ferrocyanide in mol/m^3. The graph shows three distinct curves, each corresponding to a different bulk concentration of the redox species: the blue curve represents a bulk concentration of 1 mM, the green curve corresponds to 3.3 mM, and the red curve represents 5 mM. The concentration of ferrocyanide increases sharply between 4 and 6 seconds, reaching a plateau where the reduction process is at its peak, and then begins to decrease between 14 and 16 seconds as oxidation takes over. This behaviour indicates that during the forward scan of the CV cycle, ferricyanide is reduced to ferrocyanide, and as the potential reverses, the oxidation reaction regenerates ferricyanide. The bottom panel, titled "Concentration of Ferricyanide consumed during Oxidation," displays the inverse process, showing how ferricyanide is depleted during reduction and regenerated during oxidation. The x-axis represents time in seconds, spanning from 0 to 18 seconds, while the y-axis represents the concentration of ferricyanide in mol/m^3. Similar to the top panel, the different curves correspond to different bulk concentrations. Here, at the beginning of the cycle, ferricyanide is at its highest concentration, and as reduction occurs, its concentration decreases sharply between 4 and 6 seconds, reaching a minimum where ferrocyanide formation is at its maximum. As oxidation begins around 14 seconds, the concentration of ferricyanide increases again, restoring the original balance of the redox couple.

The next set of parameter studies focused on the exchange current density (i_0) and the rate constant (k_0) as shown in Figure 5.19. These parameters influence the rate of electron transfer at the electrode interface and determine whether the reaction is more

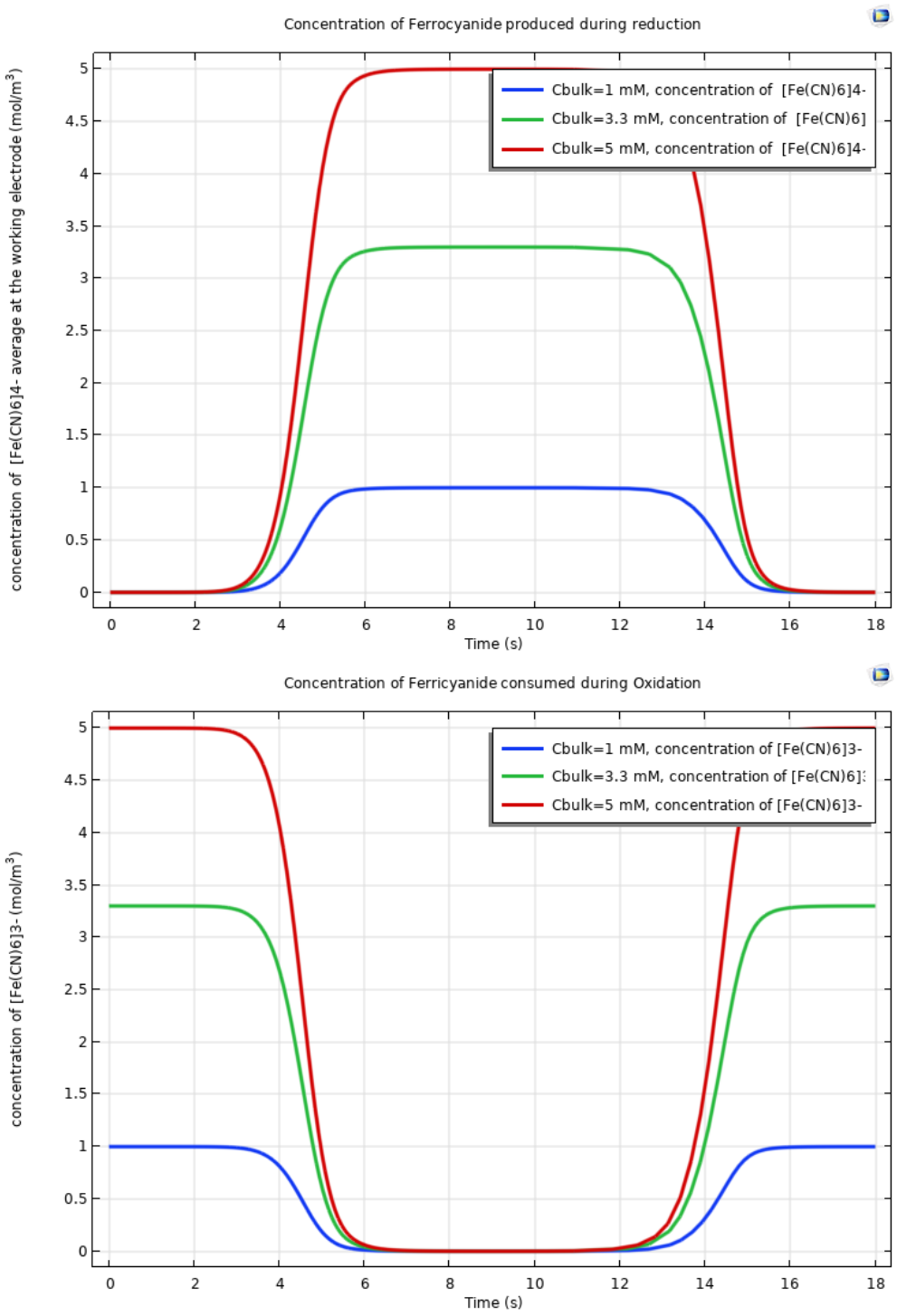

Figure 5.18: Concentration Variation Profile of CV Simulation of a Bare Electrode. The figures present the concentration profile over time, illustrating the dynamic changes in the reactants and products during the CV simulation of a bare electrode in the presence of the ferricyanide/ferrocyanide redox couple $[Fe(CN)_6]^{3-/4-}$. The concentration is varied from 1 mM to 5 mM.

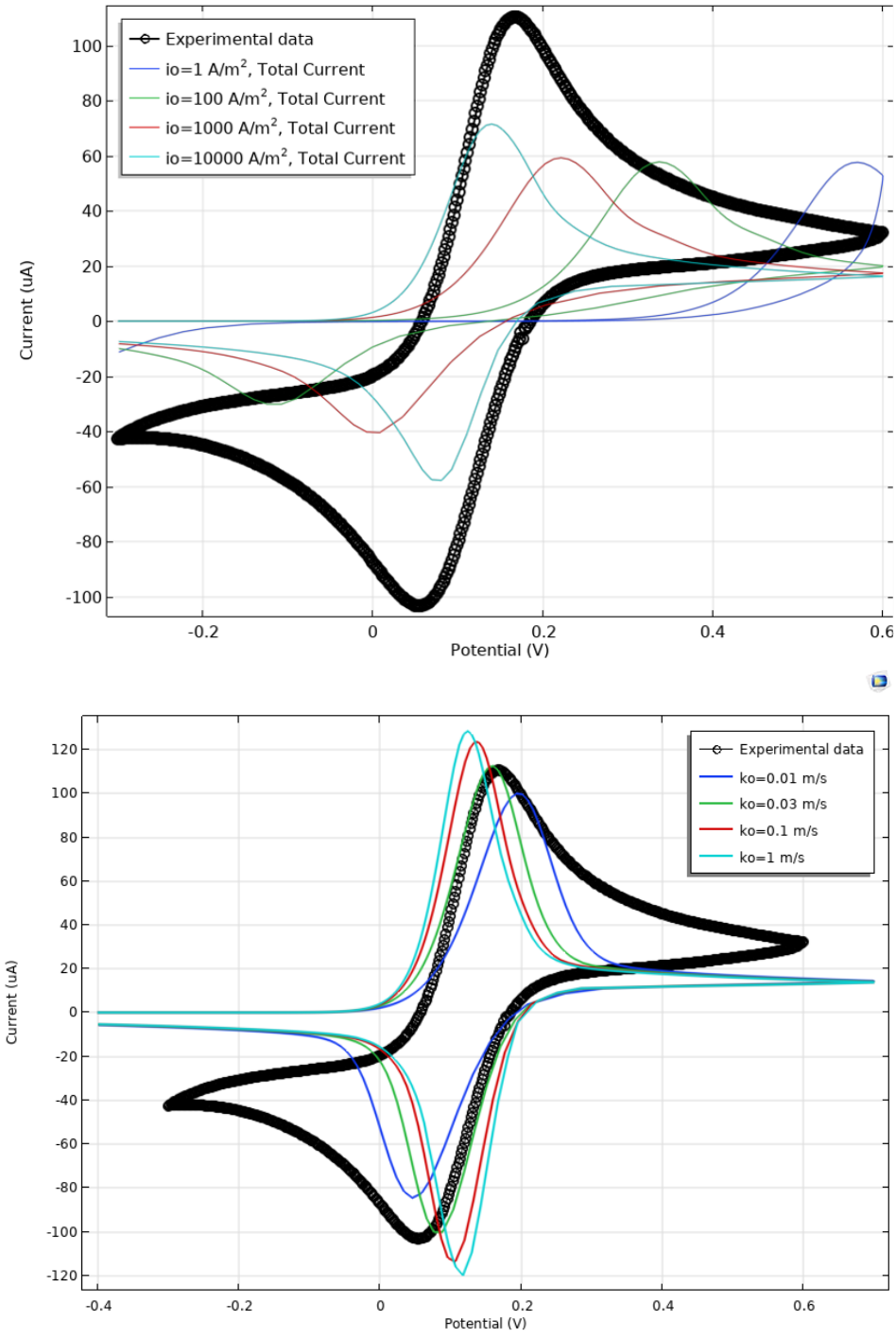

Figure 5.19: Variation of current exchange density (i_0) and rate constant (k_0). i_0 and k_0 Variation in CV Simulation of a Bare Electrode. The figures illustrate the effect of varying the exchange current density (i_0) and the rate constant (k_0) on the CV response of a bare electrode. The top figure presents the variation in i_0, with values ranging from $1\,A/m^2$ to $10000\,A/m^2$. The bottom figure shows the effect of varying k_0, with values from $0.01\,m/s$ to $1\,m/s$.

kinetically or diffusion-controlled. The top panel illustrates the effect of varying the exchange current density on CV response. The x-axis represents the applied potential in volts, ranging approximately from -0.3 V to 0.6 V, while the y-axis shows the measured current in microamperes. Experimental data is represented by black circular markers, and the simulated responses for different values of (i_0) are shown in coloured curves: 1 A/m^2, 100 A/m^2, 1000 A/m^2, and 10000 A/m^2. The exchange current density is a measure of the intrinsic electrochemical activity at equilibrium, affecting how easily electrons transfer between the electrode and the redox species. The results show that at low i_0 values, the CV curves exhibit significant peak separation and lower current responses, indicating sluggish electron transfer kinetics. As i_0 increases, the system becomes more reversible, with sharper peaks and reduced separation between oxidation and reduction.

At extremely high values ($i_0 = 10000 A/m^2$), the system approaches an idealised reversible behaviour. However, some deviation from the experimental data is still observed, which suggests that certain variations between the simulation and experimental results arise due to factors such as electrode surface contamination, surface roughness, material properties, and other inconsistencies. These factors are not explicitly accounted for in the model.

In Figure 5.19 (bottom panel), the impact of varying rate constant (k_0) is investigated. Here, the x-axis represents the applied potential, ranging from -0.4 V to 0.6 V, while the y-axis represents the current in μA. The experimental data is shown as black circular markers, while the simulated curves represent different values of k_0: $0.01 m/s$, $0.003 m/s$, $0.1 m/s$, and $1 m/s$. The rate constant dictates the speed of electron transfer across the electrode interface, influencing whether the reaction is kinetically or diffusion controlled. At low k_0 values, the CV response reaches $1 m/s$, leading to a highly symmetric CV response. This trend indicates that as electron transfer becomes faster, the redox reaction approaches ideal reversibility, with higher k_0 values providing better agreement with experimental data and showing improvement in the model accuracy

These parameter variations demonstrated how i_0 and k_0 influence the electrochemical response of the system. The observation from these is that increasing i_0 leads to higher current values and reduced peak separation, improving agreement with experimental data up to a certain threshold. Similarly, increasing k_0 results in a more reversible reaction, reducing kinetic limitations and improving the shape of the CV curve. These k_0-CV trends confirms strongly with classical Butler-Volmer kinetics effects, where reaction kinetics influences the overall electron transfer rate. The comparison of different values reveals that $k_0 = 0.03$ m/s aligns most closely with experimental data, confirming the ability of the numerical model to capture essential electrochemical behaviour of the bare Au electrode.

Here, one possible explanation for the remaining deviations is the assumption that the charge transfer coefficient (α_a, α_c) is set to 0.5 in the model. This value corre-

sponds to an ideally reversible reaction, yet the experimental voltammogram suggests a slight asymmetry in peak values, indicating that the reaction may not be fully reversible. The literature, including studies such Bonaldo et al.[10], [70] and Franchin et al. [9], also reports deviations between experimental and simulated data. Another explanation might be that the equilibrium potential for both the WE and CE in the experimental system also shows slight variations, suggesting that reaction kinetics at the two electrodes may differ. Adjusting the charge transfer coefficient could therefore improve the model accuracy. Another source of deviation could be mass transport limitations. The model assumes complete electroneutrality in the solution, meaning no bulk reactions occur in the electrolyte, as it is buffered with PBS. This assumption eliminates concentration gradients in the bulk region, which may not fully reflect real experimental conditions. A more relaxed constraint on electroneutrality might allow for better agreement with experimental data. Additionally, C_{dl} has been considered in the model, but at the bare electrode, it does not significantly impact the results. The same C_{dl} value has been applied for both the WE and CE, yet their surface areas are different, which might influence the accuracy of the simulation. Another possible source of deviation is the use of older, recycled electrodes, which could introduce inconsistencies in experimental results due to surface degradation or contamination.

The next parameter studied was the scan rate variation and its impact on the CV response of the bare electrode. The scan rate determines how quickly the applied potential is swept across the electrode surface, directly influencing the peak currents and overall shape of the voltammogram. The results from this simulation are shown in Figure 5.20. The top panel represents the voltammograms obtained at different scan rates, which shows the relationship between applied potential and measured current. The x-axis represents the applied potential in volts, ranging approximately from -0.4 V to 0.6 V, while the y-axis represents the current in μA. As before, the black curve correspond to the experimental data recorded at a scan rate of 100 mV/s (-0.3 V to 0.6 V), while the simulated CV responses at different scan rates are represented by coloured curves: 50 mV/s in blue, 100 mV/s in green, 500 mV/s in red, and 1000 mV/s in cyan. The results show that as the scan rate increases, the peak currents also increase, which is expected in CV experiments since a faster electron transfer process leads to higher current values. At lower scan rates, such as 50 and 100 mV/s, the CV curves exhibit smaller peak currents and broader peaks, suggesting slower reaction kinetics. At 100 mV/s, the simulated data closely matches the experimental results, validating the accuracy of the model at this moderate scan rate.

The bottom panel in Figure 5.20 illustrates how the applied potential varies over time for different scan rates. It visualises the potential sweep used in the simulations. The x-axis represents time in seconds, spanning from 0 to approximately 40 seconds, while the y-axis represents the electric potential in volts, covering the same range as in the CV plot. The different scan rates are represented by coloured curves, where red corresponds to 50 mV/s, green to 100 mV/s, blue to 500 mV/s, and cyan to 1000

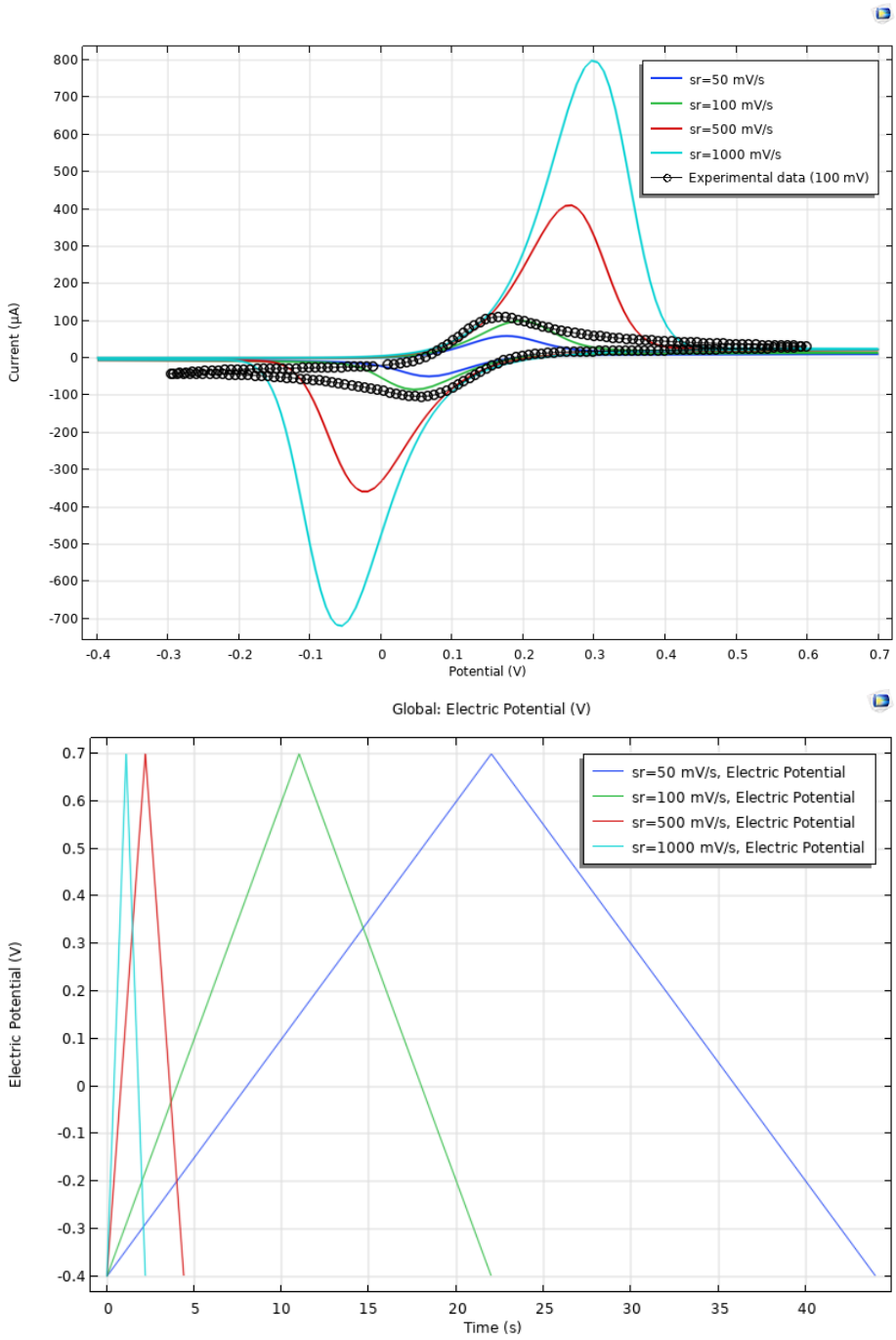

Figure 5.20: Scan Rate Variation in CV Simulation of a Bare Electrode. The figures illustrate the effect of scan rate variation on the CV response of a bare electrode. The top figure presents the CV response for different scan rates. The black curve represents experimental data recorded at a scan rate of 100 mV/s (from -0.3 to +0.6 potential range), while the coloured curves correspond to simulated scan rates of 50 mV/s, 100 mV/s, 500 mV/s, and 1000 mV/s. The bottom figure displays the time evolution of the applied potential for each scan rate.

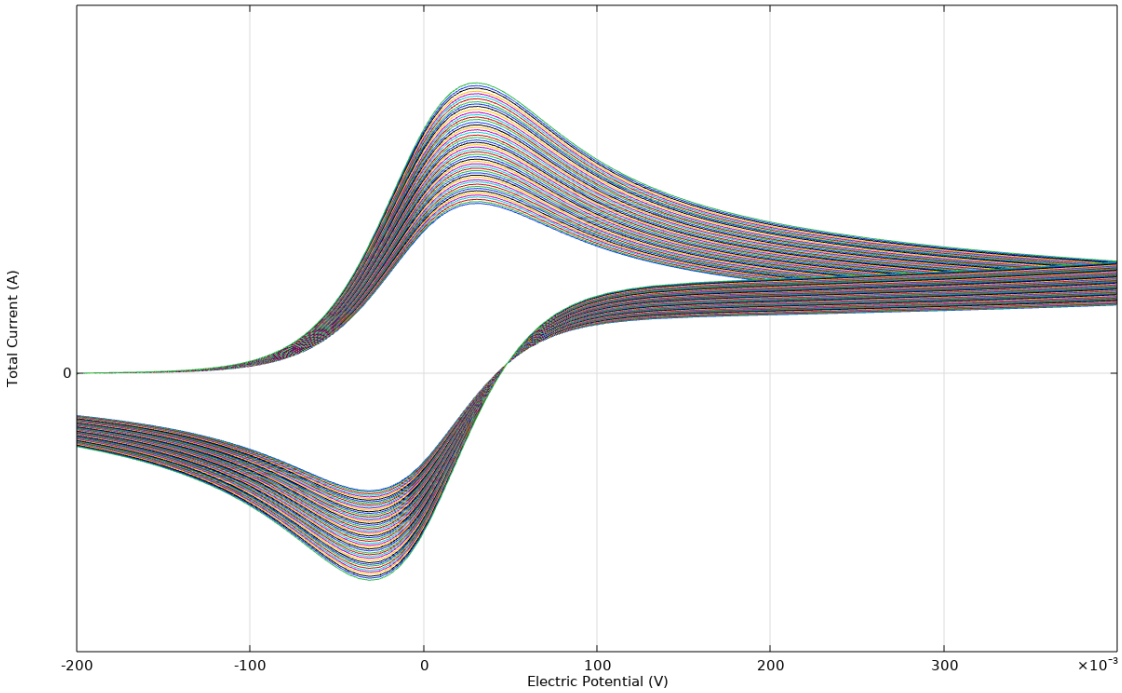

Figure 5.21: Simulated CV Response for Varying WE Size. The plot illustrates the results of a parametric sweep where the WE size was varied from 3 mm to 4 mm. The simulations were conducted within a potential range of 0.4 V to -0.02 V at a scan rate of 100 mV/s,

mV/s. The plot demonstrates a triangular waveform indicative of a CV process. This plot also confirms that the simulation imposes the required electric potentials that were bounded within the vertex potential. Furthermore, this plot confirms that at lower scan rates, such as 50 and 100 mV/s, the potential is swept more slowly, resulting in longer cycle durations, while at higher scan rates, such as 500 and 1000 mV/s, the potential changes more rapidly, leading to shorter cycle times. The blue and cyan curves clearly show that at high scan rates, the potential reaches its upper and lower limits much faster than at lower scan rates.

Another key aspect of this study involved conducting a parametric sweep by varying the WE size from 3 mm to 4 mm in steps of 0.01. This was done to study its effect on the overall CV response. As the WE size increases, the effective electrode surface area expands, leading to a direct impact on the magnitude of the current response. This occurs due to modifications in the diffusion layer, which governs mass transport dynamics, as well as alterations in the charge transfer process at the electrode-electrolyte interface. Larger electrode surfaces typically result in higher peak currents, as more electroactive species participate in the redox process. Additionally, variations in peak separation can provide insights into changes in electron transfer kinetics and potential shifts in the reversibility of the redox reaction. The parametric sweep, as visualised in Figure 5.21, which demonstrates how increasing the WE size systemati-

cally affects the CV response. It can clearly be seen that as the WE size increases the current increases as well.

The model and simulation for the bare electrodes were developed to replicate the CV responses of the system and were fine-tuned using the parameters shown in Table 5.3. Key parameters such as the equilibrium potential, reaction rate constant, scan rate, concentration of reactants, and exchange current density were carefully chosen to ensure the model accurately reflects the electrochemical behaviour. By adjusting these values, the simulation was optimised to better match experimental data, improving both its reliability and ability to predict system behaviour.

Table 5.3: Parameters List for Simulation of Bare Electrode. The table lists some of the key parameters applied in the modelling of the bare electrode. These include also the key parameters that were used to calibrate for model optimisation.

Parameter	Value
Diffusion coefficient	$7 \times 10^{-}10\ m^2/s$
Charger transfer coefficient	0.5
CV vertex potential 1	$[-0.2, -0.4]V$
CV vertex potential 2	$[0.6, 0.7]V$
Equilibrium potential	[105, 110] mV
Conductivity	1.6 S/m
Electrolyte concentration	3 mM
Reaction rate constant	0.03 m/s
Double layer capacitance	$0.1\ F/m^2$

5.4.2 CV Model of Functionalised Electrode

In the following section, the results from the functionalised electrode simulations will be presented.

Electrode Functionalised with SAM and Enzyme

This section presents the CV voltammograms for the electrode functionalised with a SAM of MUA and Strep-HRP conjugates, showing functionalisation affects electron transfer kinetics and alters the overall electrochemical behaviour. In Figure 5.22, the CV response of an electrode functionalised with a SAM and Strep-HRP enzymes,

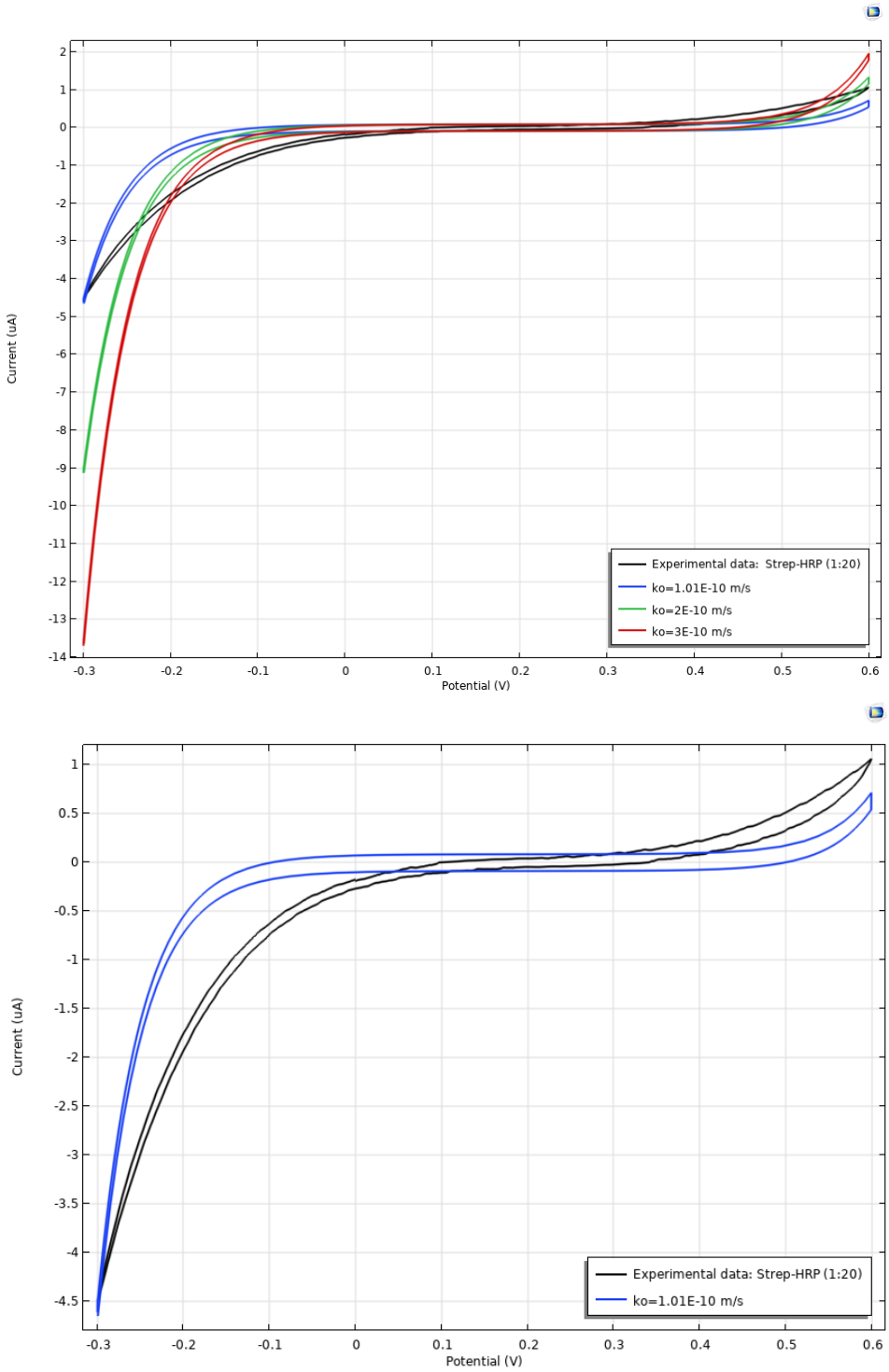

Figure 5.22: Electrode Functionalisation with SAM and Enzyme. The two plots shows the simulation of electrode functionalisation with SAM and Strep-HRP. The top plot shows the different k_0 values, while the bottom plot shows that the best fitted k_0 value is the blue curve with the 1.01×10^{-10} m/s

demonstrating the substantial impact of functionalisation on electron transfer kinetics and overall electrochemical behaviour. The modification of the electrode surface introduces additional R_{CT}, altering the redox process and shifting the electrochemical response away from that observed for a bare electrode. This is due to the insulating properties of SAM as it lowers the exchange current, thereby restricting direct electron exchange between the redox species in the solution and the electrode surface as was also observed from the experimental data.

The x-axis in both plots represents the applied potential in volts, covering a range of approximately -0.3 V to 0.6 V, while the y-axis represents the current response in μA. As observed from the plots, the different curves corresponds to various values of the reaction rate constant. The black curve represents experimental data from the Strep-HRP functionalised electrode as in Method 1, where the enzymes HRP and Strep-HRP were directly attached onto the MUA via EDC/NHS chemistry. The simulated responses are shown for $k_0 = 1.0\times^{-10}$ m/s (blue), $k_0 = 2.2\times^{-10}$ m/s (green), and $k_0 = 5.8\times^{-10}$ m/s (red). Compared to the CV of bare electrode seen in for example Figure 5.19, the functionalised electrode exhibits a more sigmoidal curve, characteristic of surface confined redox reactions. This behaviour change suggests that electron transfer is no longer as fast or direct as in the bare electrode case. The most significant observation is the drastic reduction in the reaction rate constant (k_0), indicating a much slower electron transfer process. While the bare Au electrode typically has a reaction rate constant of around 0.03 m/s, the functionalised electrode shows values in the range of 10^{-10} m/s, confirming that electron transfer is severely hindered by the presence of the SAM of MUA and the enzyme layers. This drastic reduction in k_0 can be attributed to several factors, including the SAM layer. This layer acts as an insulating barrier, forming a densely packed film on the electrode surface, which significantly increases R_{CT}, which was also seen in the experiments. This obstructs ion diffusion and slows down electron movement at the interface. The further introduction of Strep-HRP conjugates, creates a thick biomolecular layer which impairs electron transfer. Unlike the bare Au electrode where electron transfer is direct and rapid, the electrons are transferred via enzyme-mediated redox reactions for Strep-HRP, and are kinetically limited, hence the extreme reduction in reaction rate constant. The rate constant is used as a fitting parameter here in the simulations. The enzyme layer is incorporated into the system and is modelled as an additional factor affecting the exchange current density (i_0), which is mathematically defined as:

$$i_0 = nAFk_0C_{bulk}$$

where k_0 is the reaction rate, i_0 is the exchange current density, n denoting number of electrons transferred, A is the electrode surface area, F is Faraday's constant, and C_{bulk} represents the concentration of the redox species.
In the top panel of Figure 5.22, the black curve is representing the experimental data

as before. It provides a reference for determining which k_0 value best fits the actual electrochemical behaviour. Among the simulated curves, the blue curve ($k_0 = 1.0 \times 10^{-10}$m/s) fit the most with the experimental data, confirming that this value best represents the electron transfer kinetics in the functionalised system. The green and red curves, which correspond to higher k_0 value, deviate more from the experimental data. For this model simulation, several parameters were incorporated based on experimental data such as C_{dl}, exchange current density ($i_0 = RT/(nFR_{ct})$), R_{CT}, equilibrium constant to improve the model accuracy and better capture the biosensor behaviour. The list of some of the key parameters used in the simulation is shown in Table 5.3:

Table 5.4: Parameters List for Simulation of SAM and enzyme on Electrode. The table lists some of the key parameters applied in the modelling of the electrode with the SAM of MUA and Strep-HRP. These include also the key parameters that were used to calibrate for model optimisation as well.

Parameter	Value
Scan rate	100 mV
Diffusion coefficient	$7 \times 10^{-}10\ m^2/s$
Equilibrium potential	200 mV
Exchange current density	0.01 A/m^2
Charger transfer coefficient	0.5
CV vertex potential 1	-0.3 V
CV vertex potential 2	0.6 V
Conductivity	1.6 S/m
Electrolyte concentration	3 mM
Reaction rate constant	4.0×10^{-8} m/s
Double layer capacitance	0.1 F/m^2

Electrode Functionalised with SAM and Antibody

The simulation results from the functionalised electrodes with MUA, enzymes and antibodies at 20 μg/mL can be seen in Figure 5.23. These voltammograms illustrate how increasing the concentration of BAM antibodies affects electron transfer kinetics and charge transport at the electrode-electrolyte interface as it was seen with SAM and Strep-HRP functionalised electrodes.

The x-axis represents the applied potential (V), spanning approximately -0.3 V to 0.6 V, while the y-axis represents the measured current (μA). The black curve in both plots corresponds to the experimental data obtained for an electrode functionalised with 20 μg/mL BAM antibodies as well as Strep-HRP. The coloured curves represent simulated CV responses at different reaction rates (k_0), which influence the electron transfer process at the electrode surface. In the top panel, different k_0 values are tested to evaluate their impact on the electrochemical response. Here, the blue, green, and

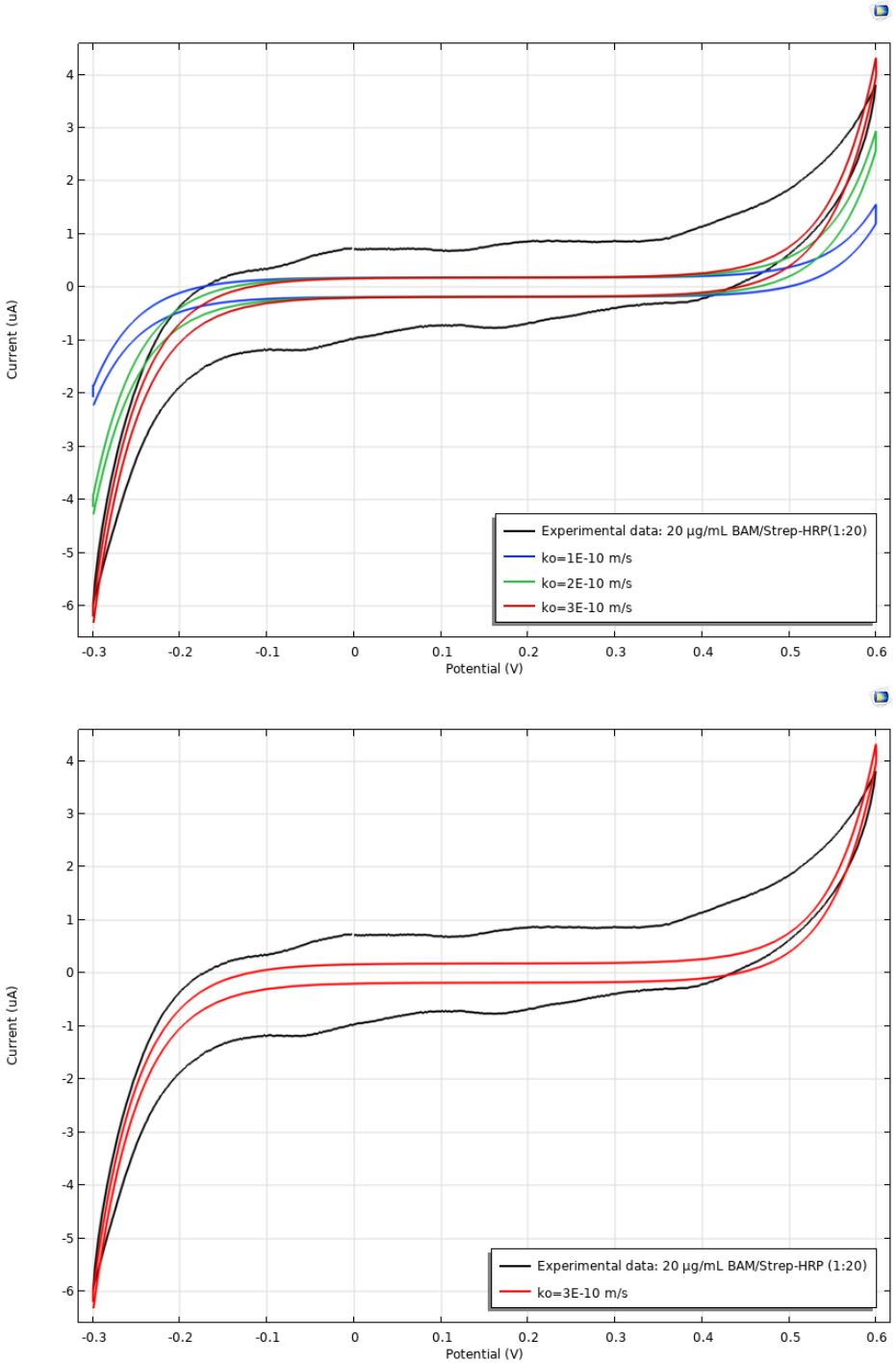

Figure 5.23: Electrode Functionalisation with SAM, Antibody, and Enzyme. The two plots illustrate the simulation results for electrode functionalisation with SAM, antibody, and Strep-HRP. The top plot presents the variation in k_0 values, while the bottom plot highlights the best fit to the experimental data (black curve). The optimal k_0 value, which aligns most closely with the experimental results, is represented by the red curve at 3.0×10^{-10} m/s.

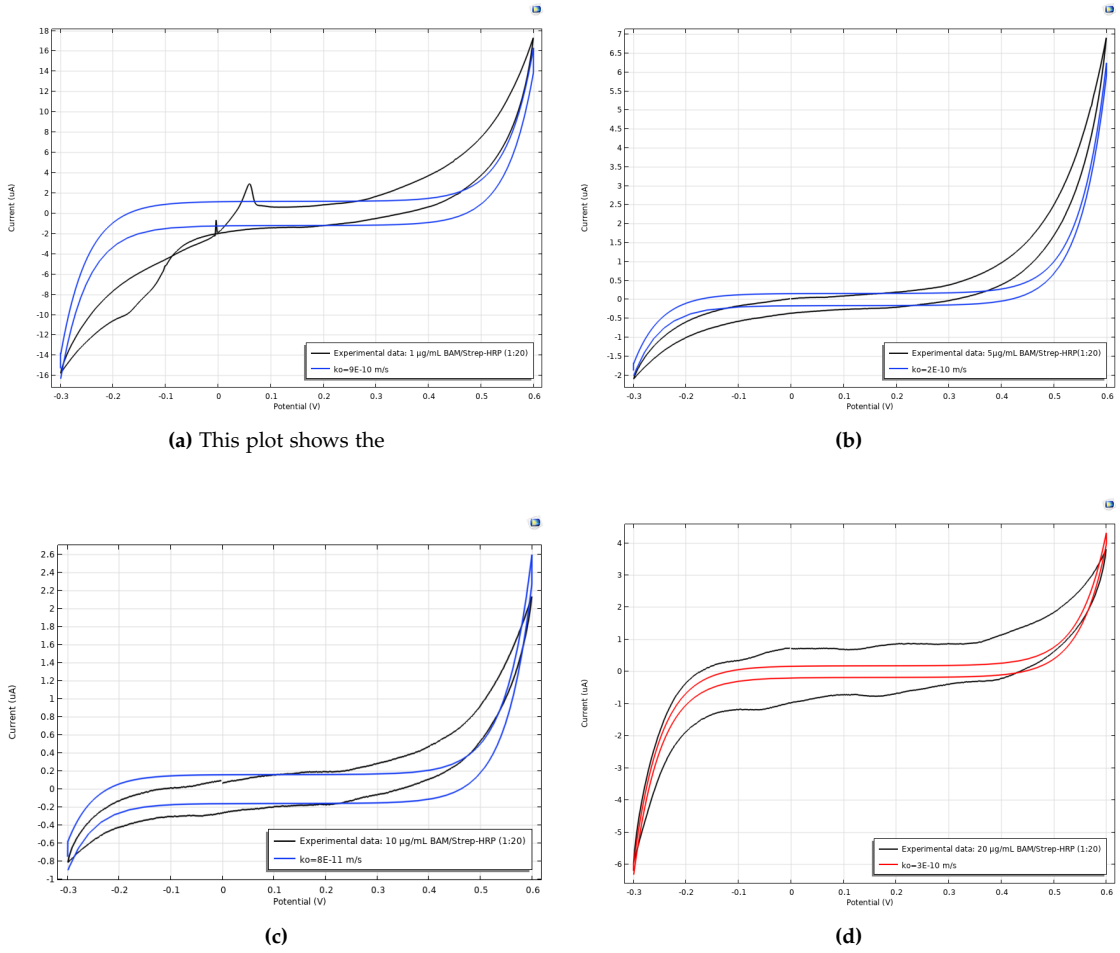

(a) This plot shows the **(b)** **(c)** **(d)**

Figure 5.24: Electrode Functionalisation with SAM, Antibody, and Enzyme. The four plots illustrate the simulated and experimental CV curves for electrodes functionalised with SAM, BAM, and Strep-HRP at different BAM concentrations: (a) 1 μg/mL, (b) 5 μg/mL, (c) 10 μg/mL, and (d) 20 μg/mL. The experimental data (black curves) are compared with simulated results at varying reaction rate constants k_0. As BAM concentration increases, electron transfer rate leading to a systematic reduction in k_0. The best-fitting k_0 values are 9.0×10^{-10} m/s for (a), 2.0×10^{-10} m/s for (b), 8.3×10^{-11} m/s for (c), and 3.0×10^{-10} m/s for (d).

red curves correspond to $k_0 = 1.0 \times 1^{-10}$ m/s, $k_0 = 2.0 \times 1^{-10}$ m/s, and $k_0 = 3.0 \times 1^{-10}$ m/s, respectively. As k_0 increases, the CV curves shift and the electron transfer kinetics improve slightly, affecting the peak current and the overall shape of the curve. The experimental CV curve is used as a reference to find the best fit. The bottom panel is showing the best fitted k_0 value by comparing the experimental data with the optimised simulation. In this situation, the red curve ($k_0 = 3.0 \times 1^{-10}$ m/s) shows the closest match to the experimental results, indicating that this value best represents the electron transfer rate of the biosensor. The agreement between the experimental and simulated data suggests that at this BAM concentration, electron transfer is

significantly hindered due to the insulating effect of the SAM layer.

In Figure 5.24, the simulated CV results for electrodes functionalised with varying concentrations ranging from 1 μg/mL to 20 μg/mL, are presented. The rate constant k_0, which directly impacts the electron transfer rate is varied from 1×10^{-10} to 1×10^{-11} m/s, with input parameters from the experimental EIS data, as well as the equilibrium potential that was calculated from each experimental CV curves. These parameters are presented in Table 5.5 below.

Table 5.5: The table presents the extracted values from the experimental EIS data. By fitting the EIS data to an equivalent circuit model, the double layer capacitance is determined for each. Additionally, the corresponding equilibrium potential for each dataset was determined and is listed accordingly.

BAM Concentration (μg/mL)	C_{dl} (F/m^2)	Equilibrium Potential (V)
1	1.5	0.15
5	0.201	0.12
10	0.2	0.12
20	0.22	0.16

These simulation results are compared and validated with the experimental CV curves. For the BAM concentration of 1 μg/mL in Figure 5.24a, the CV curve exhibits a sigmoidal shape. The rate constant of 1×10^{-10} m/s shows very good agreement with the experimental result, and suggests a relatively fast rate of electron transfer for low BAM concentrations. The good simulation and experimental fit also indicates that biomolecular interactions do not significantly hinder charge transfer at the electrode-electrolyte interface. In Figure 5.24b, the BAM concentration was set to 5 μg/mL, and shows a good fit with experimental data for $k0 = 2 \times 10^{-10}$ m/s. The decrease in the rate constant indicates that the increased BAM concentration insulates active areas of the electrode and exhibits some steric hindrances to the ionic transport, thereby blocking the access of redox species to the electrode surface. For the BAM concentration of 10 μg/mL in Figure 5.24c, the simulated data matches well with the experimental data at rate constants around $k_0 = 7 \times 10^{-11}$ m/s. The reaction kinetics is slowed down as a result and R_{CT} increases, while the increased antibody coverage further reduces the accessibility of ions to the electrode surface. For the BAM concentration of 20 μg/mL in Figure 5.24d, the simulated CV curve for $k_0 = 3 \times 10^{-10}$ m/s shows a very good match with the experimental results, in addition to the observed slow reaction kinetics, capacitive behaviour becomes more pronounced do to the increase in resistance at the electrode-electrolyte interface. All the key parameters that were optimised, were applied to simulate this functionalised electrode with SAM, BAM, and Strep-HRP. These key parameters can be seen in Table 5.6.

Table 5.6: Parameters List for the Simulation of EQCM Sensor. The table lists key parameters applied in the modeling of cyclic voltammetry of ferrocyanide/ferricyanide redox reaction in the EQCM sensor.

Parameter	**Value**
Reactant bulk concentration (C_{bulk})	3 mM
Conductivity	1.6 S/m
Current density (i_{oa})	0.01 A/m^2
Vertex potential 1	-0.3 V
Vertex potential 2	0.6 V
Scan rate	100 mV/s
Reference concentration (C_{ref})	C_{bulk}
Rate constant (k_o)	4×10^{-8} m/s
Exchange current density (i_o)	nFk_0C_{bulk}
io_2	(R_{const} * T) / (n * F_{const}) = 0.03072 A/m^2
Charge transfer resistance	8219 $\Omega \cdot cm^2$
Calculated rate constant (k_{calc})	1.0613 $\times 10^{-7}$ m/s
Calculated current density (i_{dcalc})	0.011578 A
Calculated current (i_{calc})	9.1874 $\times 10^{-8}$ A
Concentration of BAM antibodies (AB)	10 μg/mL (0.01 kg/m^3)
Sensitivity parameter (γ)	0.001 m^3/mol
Molecular weight of BAM (mw_{bam})	150,000 g/mol (150 kg/mol)
Antibody concentration (AB_{conc})	6.6667 $\times 10^{-5}$ mol/m^3
Dilution factor 1:100 ($df100$)	0.2
Dilution factor 1:500 ($df500$)	0.04
Effective rate constant (k_{eff})	$k_o \times e^{-\gamma_0 \times AB_{conc}}$
Effective current (i_{eff})	$F \times k_{eff} \times HRP \times C_{bulk}$

6 Conclusion

It can be concluded that the aim of the project has been successfully achieved. The project involved a computational part and an experimental part, where the latter was divided into three methods referred to as Method 1, Method 2, and Method 3, with each getting more advanced. A key aspect of all experiments was the reuse and recycling of SPGEs. For this reason, the electrode cleaning required both mechanical and electrochemical cleaning steps prior to each experiment. Through this process, it was found that repeated use of SPGEs led to electrode degradation. This was particularly evident in Method 3, where CV voltammograms showed that the electrochemical performance of the electrodes had decreased by nearly half from Method 1 to Method 3.

In Method 1, SPGEs were functionalised with MUA, HRP and Strep-HRP conjugates. From CV measurements, it was found that both biomolecules did indeed bind to the MUA layer. From the EIS data, MUA exhibited the highest charge transfer resistance. The HRP tests, however, showed increasing impedance with increasing dilution. A similar trend was seen for Strep-HRP, albeit at significantly lower impedance. The CA tests showed the current response increased with decreasing dilution ratios in both cases. Once again, the Strep-HRP exhibited lower electrochemical signals compared to HRP. It was found that, for biosensor purposes where reliability and specificity are essential, the approach used in this method is not ideal due to non-specific binding.

In Method 2, SPGEs were functionalised with a SAM of MUA onto which BAM1676 antibodies were covalently immobilised. Here, Strep-HRP was used as analyte. Different antibody concentrations were tested. The immobilisation of different concentrations of antibodies were verified through CV. CV results after adding Strep-HRP revealed a slightly lower current response compared to those without Strep-HRP. EIS data revealed a concentration-dependent behaviour, where higher antibody concentrations lead to higher impedance signals. Additionally, the BAM-modified electrodes exhibited very low R_{CT} values (and thus faster electron transfer), indicating the electrochemical activity at the electrode was kinetically-driven rather than diffusion-controlled. CA data revealed higher current responses with increasing antibody concentration in the presence of Strep-HRP. From this method, it was demonstrated that the presence of antibodies enhanced specificity.

In Method 3, the functionalisation steps from Method 1 and 2 were further advanced using click chemistry for specific and reliable analyte detection. For this purpose, a novel click chemistry protocol was developed and optimised. In the process of developing the protocol, a series of preliminary tests were conducted. Finally, functionalisation tests were performed on the click-functionalised electrodes using CA. From these tests, promising results were obtained, as they confirmed successful click reaction, functionalisation, and detection abilities. Despite the promising results, more work is required to optimise and verify the method by performing additional tests and measurements.

In the modelling part of the project, 3D biosensor models were developed and simulated to simulate the redox reaction of ferro/ferricyanide on both bare Au electrodes and Au electrodes functionalised with SAMs, enzymes, and antibodies, mimicking experimental test conditions. The simulated CV voltammograms closely mirrored the experimental data across various scenarios, with the impact of reaction rate kinetics on electron transfer and diffusive transport at the electrode-electrolyte interface being highlighted. The bare Au electrode presents a fast and diffusion-controlled electron transfer, while the functionalised electrodes with SAMs, enzymes and antibodies creates a controlled and systematic reduction in k_0 due to steric effects. The developed models lays the foundation for future works and can be applied to study different aspect of electrochemical biosensor platform. In addition, the model can be further extended to systems with multiple WEs in order to find the optimal distance between the electrodes to avoid cross-reactions or contaminations if multiple analytes are being tested. These models can be optimised even more by the inclusion of enzymatic reactions as well as diffusive transport across SAM layers by defining a separate thin-film subdomain on the electrode surface with a reduced diffusion coefficient D_{SAM} via expressions that includes the thickness of the SAM layer δ_{SAM}.

Bibliography

[1] Y. Zhou, Y. Fang, and R. Ramasamy, "Non-covalent functionalization of carbon nanotubes for electrochemical biosensor development," *Sensors*, vol. 19, no. 2, p. 392, Jan. 2019, ISSN: 1424-8220. DOI: 10.3390/s19020392. [Online]. Available: http://dx.doi.org/10.3390/s19020392.

[2] S. Clair and M. R. Norris, "Strategy for functionalization of electrodes with discrete, unmodified small molecules exhibiting aqueous stability," *Journal of Materials Chemistry A*, vol. 8, no. 31, pp. 15 681–15 686, 2020, ISSN: 2050-7496. DOI: 10.1039/d0ta03785k. [Online]. Available: http://dx.doi.org/10.1039/D0TA03785K.

[3] I.-H. Cho, D. H. Kim, and S. Park, "Electrochemical biosensors: Perspective on functional nanomaterials for on-site analysis," *Biomaterials Research*, vol. 24, no. 1, Feb. 2020, ISSN: 2055-7124. DOI: 10.1186/s40824-019-0181-y. [Online]. Available: http://dx.doi.org/10.1186/s40824-019-0181-y.

[4] H. Chen, J. Zhang, R. Huang, *et al.*, "The applications of electrochemical immunosensors in the detection of disease biomarkers: A review," *Molecules*, vol. 28, no. 8, p. 3605, Apr. 2023, ISSN: 1420-3049. DOI: 10.3390/molecules28083605. [Online]. Available: http://dx.doi.org/10.3390/molecules28083605.

[5] T. Pedersen, P. Fojan, A. K. N. Pedersen, N. E. Magnusson, and L. Gurevich, "Amperometric biosensor for quantitative measurement using sandwich immunoassays," *Biosensors*, vol. 13, no. 5, p. 519, May 2023, ISSN: 2079-6374. DOI: 10.3390/bios13050519. [Online]. Available: http://dx.doi.org/10.3390/bios13050519.

[6] R. Cancelliere, T. Cosio, E. Campione, *et al.*, "Label-free electrochemical immunosensor as a reliable point-of-care device for the detection of interleukin-6 in serum samples from patients with psoriasis," *Frontiers in Chemistry*, vol. 11, Nov. 2023, ISSN: 2296-2646. DOI: 10.3389/fchem.2023.1251360. [Online]. Available: http://dx.doi.org/10.3389/fchem.2023.1251360.

[7] P. Yáñez-Sedeño, A. González-Cortés, S. Campuzano, and J. M. Pingarrón, "Copper(i)-catalyzed click chemistry as a tool for the functionalization of nanomaterials and the preparation of electrochemical (bio)sensors," *Sensors*, vol. 19, no. 10, p. 2379,

May 2019, ISSN: 1424-8220. DOI: 10.3390/s19102379. [Online]. Available: http://dx.doi.org/10.3390/s19102379.

[8] L. Franchin, A. Paccagnella, and S. Bonaldo, "Multiphysics model for simulation of electrochemical signals for biosensing applications," in *2024 IEEE BioSensors Conference (BioSensors)*. IEEE, 2024, pp. 01–04. DOI: 10.1109/BioSensors61405.2024.10712666. [Online]. Available: https://ieeexplore.ieee.org/document/10712666.

[9] L. Franchin and S. Bonaldo, "Multiphysics modeling of electrochemical impedance spectroscopy responses of sam-modified screen-printed electrodes," *Sensors*, vol. 24, no. 3, p. 858, Jan. 2024, ISSN: 1424-8220. DOI: 10.3390/s24030858. [Online]. Available: http://dx.doi.org/10.3390/s24030858.

[10] S. Bonaldo, L. Franchin, G. Rosati, S. Tonello, A. Merkoçi, and A. Paccagnella, "Multiphysics simulations of screen-printed electrodes for electrochemical biosensing," in *2023 IEEE International Workshop on Metrology for Industry 4.0 & IoT (MetroInd4.0 & IoT)*. IEEE, 2023, pp. 320–325. DOI: 10.1109/MetroInd4.0IoT57462.2023.10180155. [Online]. Available: https://ieeexplore.ieee.org/document/10180155.

[11] J. Vinay Kumar, N. Shylashree, S. Hebbar, *et al.*, "Design and optimization of sensor electrode geometry for hormone sensing by comsol multiphysics software," *BioNanoScience*, vol. 14, no. 2, pp. 1044–1060, Mar. 2024, ISSN: 2191-1649. DOI: 10.1007/s12668-024-01357-5. [Online]. Available: http://dx.doi.org/10.1007/s12668-024-01357-5.

[12] A. J. B. L. R. F. H. S. White, *Electrochemical Methods: Fundamentals and Applications*, 3rd Edition. Wiley, 2022, ISBN: 978-1-119-33406-4.

[13] B. A. Patel, *Electrochemistry for Bioanalysis*, 1st Edition. Elsevier, 2021, ISBN: 978-0-12-821203-5. DOI: 10.1016/c2019-0-03108-1. [Online]. Available: http://dx.doi.org/10.1016/C2019-0-03108-1.

[14] N. Elgrishi, K. J. Rountree, B. D. McCarthy, E. S. Rountree, T. T. Eisenhart, and J. L. Dempsey, "A practical beginner's guide to cyclic voltammetry," *Journal of Chemical Education*, vol. 95, no. 2, pp. 197–206, Nov. 2017, ISSN: 1938-1328. DOI: 10.1021/acs.jchemed.7b00361. [Online]. Available: http://dx.doi.org/10.1021/acs.jchemed.7b00361.

[15] C. L. Brosseau, A. Colina, J. V. Perales-Rondon, *et al.*, "Electrochemical surface-enhanced raman spectroscopy," *Nature Reviews Methods Primers*, vol. 3, no. 1, Oct. 2023, ISSN: 2662-8449. DOI: 10.1038/s43586-023-00263-6. [Online]. Available: http://dx.doi.org/10.1038/s43586-023-00263-6.

[16] C. Brosseau, "Principles, characteristics, and applications of electrochemical surface-enhanced raman spectroscopy," in *Surface- and Tip-Enhanced Raman Scattering Spectroscopy*. Springer Nature Singapore, 2024, pp. 249–272, ISBN: 9789819758180. DOI: 10.1007/978-981-97-5818-0_10. [Online]. Available: http://dx.doi.org/10.1007/978-981-97-5818-0_10.

[17] N. K. Murugasenapathi and T. Palanisamy, "Electrochemical surface-enhanced raman spectroscopy (ec-sers): Techniques, applications, and future perspectives," in *Raman Spectroscopy*. Springer Nature Singapore, 2024, pp. 199–214, ISBN: 9789819717033. DOI: 10.1007/978-981-97-1703-3_9. [Online]. Available: http://dx.doi.org/10.1007/978-981-97-1703-3_9.

[18] D. Grieshaber, R. MacKenzie, J. Vörös, and E. Reimhult, "Electrochemical biosensors - sensor principles and architectures," *Sensors*, vol. 8, no. 3, pp. 1400–1458, Mar. 2008, ISSN: 1424-8220. DOI: 10.3390/s80314000. [Online]. Available: http://dx.doi.org/10.3390/s80314000.

[19] A. C. Lazanas and M. I. Prodromidis, "Electrochemical impedance spectroscopy–a tutorial," *ACS Measurement Science Au*, vol. 3, no. 3, pp. 162–193, Mar. 2023, ISSN: 2694-250X. DOI: 10.1021/acsmeasuresciau.2c00070. [Online]. Available: http://dx.doi.org/10.1021/acsmeasuresciau.2c00070.

[20] S. Wang, J. Zhang, O. Gharbi, V. Vivier, M. Gao, and M. E. Orazem, "Electrochemical impedance spectroscopy," *Nature Reviews Methods Primers*, vol. 1, no. 1, Jun. 2021, ISSN: 2662-8449. DOI: 10.1038/s43586-021-00039-w. [Online]. Available: http://dx.doi.org/10.1038/s43586-021-00039-w.

[21] H. S. Magar, R. Y. A. Hassan, and A. Mulchandani, "Electrochemical impedance spectroscopy (eis): Principles, construction, and biosensing applications," *Sensors*, vol. 21, no. 19, p. 6578, Oct. 2021, ISSN: 1424-8220. DOI: 10.3390/s21196578. [Online]. Available: http://dx.doi.org/10.3390/s21196578.

[22] B.-A. Mei, O. Munteshari, J. Lau, B. Dunn, and L. Pilon, "Physical interpretations of nyquist plots for edlc electrodes and devices," *The Journal of Physical Chemistry C*, vol. 122, no. 1, pp. 194–206, Dec. 2017, ISSN: 1932-7455. DOI: 10.1021/acs.jpcc.7b10582. [Online]. Available: http://dx.doi.org/10.1021/acs.jpcc.7b10582.

[23] B. Padha, S. Verma, P. Mahajan, and S. Arya, "Electrochemical impedance spectroscopy (eis) performance analysis and challenges in fuel cell applications," *Journal of Electrochemical Science and Technology*, vol. 13, no. 2, pp. 167–176, May 2022, ISSN: 2288-9221. DOI: 10.33961/jecst.2021.01263. [Online]. Available: http://dx.doi.org/10.33961/jecst.2021.01263.

[24] C. Robinson, V. B. Juska, and A. O'Riordan, "Surface chemistry applications and development of immunosensors using electrochemical impedance spectroscopy: A comprehensive review," *Environmental Research*, vol. 237, p. 116 877, Nov. 2023, ISSN: 0013-9351. DOI: 10.1016/j.envres.2023.116877. [Online]. Available: http://dx.doi.org/10.1016/j.envres.2023.116877.

[25] H. Wang, X. Long, Y. Sun, *et al.*, "Electrochemical impedance spectroscopy applied to microbial fuel cells: A review," *Frontiers in Microbiology*, vol. 13, Jul. 2022, ISSN: 1664-302X. DOI: 10.3389/fmicb.2022.973501. [Online]. Available: http://dx.doi.org/10.3389/fmicb.2022.973501.

[26] *Electrochemical impedance spectroscopy primer*, Accessed 09-02-2025. [Online]. Available: https://www.chem.uci.edu/~unicorn/243/papers/ECimp1.pdf.

[27] W. Giraud, L. Lesven, J. Jońca, *et al.*, "Reagentless and calibrationless silicate measurement in oceanic waters," *Talanta*, vol. 97, pp. 157–162, Aug. 2012, ISSN: 0039-9140. DOI: 10.1016/j.talanta.2012.04.011. [Online]. Available: http://dx.doi.org/10.1016/j.talanta.2012.04.011.

[28] "Faraday constant," 2019. DOI: doi:10.1351/goldbook.F02325. [Online]. Available: https://doi.org/10.1351/goldbook.F02325.

[29] U. Chadha, P. Bhardwaj, R. Agarwal, *et al.*, "Recent progress and growth in biosensors technology: A critical review," *Journal of Industrial and Engineering Chemistry*, vol. 109, pp. 21–51, May 2022, ISSN: 1226-086X. DOI: 10.1016/j.jiec.2022.02.010. [Online]. Available: http://dx.doi.org/10.1016/j.jiec.2022.02.010.

[30] S. Damiati and B. Schuster, "Electrochemical biosensors based on s-layer proteins," *Sensors*, vol. 20, no. 6, p. 1721, Mar. 2020, ISSN: 1424-8220. DOI: 10.3390/s20061721. [Online]. Available: http://dx.doi.org/10.3390/s20061721.

[31] A. G. Ochoa-Ruiz, G. Parra, D. López-Espinoza, *et al.*, "Electrochemical immunosensors: The evolution from elisa to eμpads," *Electroanalysis*, vol. 35, no. 4, Oct. 2022, ISSN: 1521-4109. DOI: 10.1002/elan.202200053. [Online]. Available: http://dx.doi.org/10.1002/elan.202200053.

[32] P. Karthick Kannan, C.-H. Chung, and C. Rout, *Encyclopedia of Nanoscience and Nanotechnology: Chemical and Biosensors Based on Graphene Analogue 2D Materials and Their Hybrids*, 1st Edition. ASPBS, 2016.

[33] A. Rubino and R. Queirós, "Electrochemical determination of heavy metal ions applying screen-printed electrodes based sensors. a review on water and environmental samples analysis," *Talanta Open*, vol. 7, no. 100203, p. 100 203, Aug. 2023.

[34] *Metrohm dropsens, screen-printed electrodes*, https://metrohm-dropsens.com/category/electrodes/screen-printed-electrodes/, [Accessed 14-11-2024].

[35] *Zimmer and peacock products, screen-printed electrodes*, https://www.zimmerpeacocktech.com/products/, [Accessed 14-11-2024].

[36] *Palmsens, screen-printed electrodes*, https://www.palmsens.com/products/sensors/screen-printed-electrodes/, [Accessed 14-11-2024].

[37] T. Martimiano do Prado, L. Gomes da Silva Catunda, D. Souza Correa, and S. Antonio Spinola Machado, "Homemade Silver/Silver chloride ink with low curing temperature for screen-printed electrodes," *J. Electroanal. Chem. (Lausanne Switz)*, vol. 915, no. 116316, p. 116 316, Jun. 2022.

[38] S. Hong, S. Oh, E. Kim, *et al.*, "Fabrication of screen-printed electrodes with long-term stability for voltammetric and potentiometric applications," *Sens. Actuators Rep.*, vol. 8, no. 100234, p. 100 234, Dec. 2024.

[39] S. Kongkaew, K. Joonyong, P. Kanatharana, P. Thavarungkul, and W. Limbut, "Fabrication and characterization of prussian blue screen-printed working electrode and their application for free chlorine monitoring in swimming pool water," *Electrochim. Acta*, vol. 388, no. 138558, p. 138 558, Aug. 2021.

[40] *Palmsens.com, redox.me-basic electrochemical cell setup*, https://www.palmsens.com/product/redox-me-basic-electrochemical-cell-setup/, [Accessed 27-11-2024].

[41] Z. Huang, L. Zhang, Y. Dou, *et al.*, "Electrochemical biosensor for point-of-care testing of low-abundance biomarkers of neurological diseases," *Analytical Chemistry*, vol. 96, no. 25, pp. 10 332–10 340, Jun. 2024, ISSN: 1520-6882. DOI: 10.1021/acs.analchem.4c01278. [Online]. Available: http://dx.doi.org/10.1021/acs.analchem.4c01278.

[42] C. Kokkinos, A. Economou, and M. I. Prodromidis, "Electrochemical immunosensors: Critical survey of different architectures and transduction strategies," *TrAC Trends in Analytical Chemistry*, vol. 79, pp. 88–105, May 2016, ISSN: 0165-9936. DOI: 10.1016/j.trac.2015.11.020. [Online]. Available: http://dx.doi.org/10.1016/j.trac.2015.11.020.

[43] N. Rafat, P. Satoh, S. Calabrese Barton, and R. M. Worden, "Integrated experimental and theoretical studies on an electrochemical immunosensor," *Biosensors*, vol. 10, no. 10, p. 144, Oct. 2020, ISSN: 2079-6374. DOI: 10.3390/bios10100144. [Online]. Available: http://dx.doi.org/10.3390/bios10100144.

[44] B. Mojsoska, S. Larsen, D. A. Olsen, J. S. Madsen, I. Brandslund, and F. A. Alatraktchi, "Rapid sars-cov-2 detection using electrochemical immunosensor," *Sensors*, vol. 21, no. 2, p. 390, Jan. 2021, ISSN: 1424-8220. DOI: 10.3390/s21020390. [Online]. Available: http://dx.doi.org/10.3390/s21020390.

[45] T. Bertok, L. Lorencova, E. Chocholova, *et al.*, "Electrochemical impedance spectroscopy based biosensors: Mechanistic principles, analytical examples and challenges towards commercialization for assays of protein cancer biomarkers," *ChemElectroChem*, vol. 6, no. 4, pp. 989–1003, Sep. 2018, ISSN: 2196-0216. DOI: 10.1002/celc.201800848. [Online]. Available: http://dx.doi.org/10.1002/celc.201800848.

[46] S.-J. Bu, K.-Y. Wang, X. Liu, *et al.*, "Ferrocene-functionalized nanocomposites as signal amplification probes for electrochemical immunoassay of salmonella typhimurium," *Microchimica Acta*, vol. 187, no. 11, Oct. 2020, ISSN: 1436-5073. DOI: 10.1007/s00604-020-04579-y. [Online]. Available: http://dx.doi.org/10.1007/s00604-020-04579-y.

[47] P. Ó Conghaile and D. W. M. Arrigan, "Ubiquinone electrochemistry in analysis and sensing," *Electrochemical Science Advances*, vol. 3, no. 3, Feb. 2022, ISSN: 2698-5977. DOI: 10.1002/elsa.202100214. [Online]. Available: http://dx.doi.org/10.1002/elsa.202100214.

[48] V. Svitková and V. Vyskočil, "Electrochemical behavior of methylene blue at bare and dna-modified silver solid amalgam electrodes," *Journal of Solid State Electrochemistry*, vol. 26, no. 11, pp. 2491–2499, Aug. 2022, ISSN: 1433-0768. DOI: 10.1007/s10008-022-05270-3. [Online]. Available: http://dx.doi.org/10.1007/s10008-022-05270-3.

[49] H. C. Kolb, M. G. Finn, and K. B. Sharpless, "Click chemistry: Diverse chemical function from a few good reactions," *Angewandte Chemie International Edition*, vol. 40, no. 11, pp. 2004–2021, Jun. 2001, ISSN: 1521-3773. DOI: 10.1002/1521-3773(20010601)40:11<2004::aid-anie2004>3.0.co;2-5. [Online]. Available: http://dx.doi.org/10.1002/1521-3773(20010601)40:11%3C2004::AID-ANIE2004%3E3.0.CO;2-5.

[50] S. Guerrero, D. Cadano, L. Agüí, *et al.*, "Click chemistry-assisted antibodies immobilization for immunosensing of cxcl7 chemokine in serum," *Journal of Electroanalytical Chemistry*, vol. 837, pp. 246–253, Mar. 2019, ISSN: 1572-6657. DOI: 10.1016/j.jelechem.2019.02.043. [Online]. Available: http://dx.doi.org/10.1016/j.jelechem.2019.02.043.

[51] F. Wang, Y. Xie, W. Zhu, and T. Wei, "Recent advances in functionalization strategies for biosensor interfaces, especially the emerging electro-click: A review," *Chemosensors*, vol. 11, no. 9, p. 481, Sep. 2023, ISSN: 2227-9040. DOI: 10.3390/chemosensors11090481. [Online]. Available: http://dx.doi.org/10.3390/chemosensors11090481.

[52] S. Guerrero, L. Agüí, P. Yáñez-Sedeño, and J. Pingarrón, "Design of electrochemical immunosensors using electro-click chemistry. application to the detection of il-1β cytokine in saliva," *Bioelectrochemistry*, vol. 133, p. 107 484, Jun. 2020, ISSN:

1567-5394. DOI: 10.1016/j.bioelechem.2020.107484. [Online]. Available: http://dx.doi.org/10.1016/j.bioelechem.2020.107484.

[53] M. Meldal and C. W. Tornøe, "Conference paper: Peptidotriazoles: Copper(i)-catalysed 1, 3-dipolar cycloadditions on solid phase.," *(Conference) Peptides: The Wave of the Future*, 2001. DOI: 10.13140/2.1.4092.6727. [Online]. Available: http://rgdoi.net/10.13140/2.1.4092.6727.

[54] M. Meldal and F. Diness, "Recent fascinating aspects of the cuaac click reaction," *Trends in Chemistry*, vol. 2, no. 6, pp. 569–584, Jun. 2020, ISSN: 2589-5974. DOI: 10.1016/j.trechm.2020.03.007. [Online]. Available: http://dx.doi.org/10.1016/j.trechm.2020.03.007.

[55] H. M. Pineda-Castañeda, Z. J. Rivera-Monroy, and M. Maldonado, "Copper(i)-catalyzed alkyne–azide cycloaddition (cuaac) "click" reaction: A powerful tool for functionalizing polyhydroxylated platforms," *ACS Omega*, vol. 8, no. 4, pp. 3650–3666, Jan. 2023, ISSN: 2470-1343. DOI: 10.1021/acsomega.2c06269. [Online]. Available: http://dx.doi.org/10.1021/acsomega.2c06269.

[56] S. R. Nxele, P. Mashazi, and T. Nyokong, "Electrode modification using alkynyl substituted fe(ii) phthalocyanine via electrografting and click chemistry for electrocatalysis," *Electroanalysis*, vol. 27, no. 10, pp. 2468–2478, Jun. 2015, ISSN: 1521-4109. DOI: 10.1002/elan.201500212. [Online]. Available: http://dx.doi.org/10.1002/elan.201500212.

[57] J. P. Collman, N. K. Devaraj, and C. E. D. Chidsey, ""clicking" functionality onto electrode surfaces," *Langmuir*, vol. 20, no. 4, pp. 1051–1053, Jan. 2004, ISSN: 1520-5827. DOI: 10.1021/la0362977. [Online]. Available: http://dx.doi.org/10.1021/la0362977.

[58] A. Onoda, N. Inoue, S. Campidelli, and T. Hayashi, "Cofactor-specific covalent anchoring of cytochrome b562on a single-walled carbon nanotube by click chemistry," *RSC Advances*, vol. 6, no. 70, pp. 65 936–65 940, 2016, ISSN: 2046-2069. DOI: 10.1039/c6ra14195a. [Online]. Available: http://dx.doi.org/10.1039/C6RA14195A.

[59] R. R. Pandey and C. C. Chusuei, "Carbon nanotubes, graphene, and carbon dots as electrochemical biosensing composites," *Molecules*, vol. 26, no. 21, p. 6674, Nov. 2021, ISSN: 1420-3049. DOI: 10.3390/molecules26216674. [Online]. Available: http://dx.doi.org/10.3390/molecules26216674.

[60] N. kumar and P. C. Thapliyal, "Graphene and carbon nanotube-based sensors," in *Sensors for Next-Generation Electronic Systems and Technologies*, 1st Edition. CRC Press, 2023. [Online]. Available: https://www.taylorfrancis.com/chapters/edit/10.1201/9781003288633-7/graphene-carbon-nanotube-based-sensors-neeraj-kumar-prakash-chander-thapliyal.

[61] S. M. Seifati, N. Nasirizadeh, and M. Azimzadeh, "Nano-biosensor based on reduced graphene oxide and gold nanoparticles, for detection of phenylketonuria-associated dna mutation," *IET Nanobiotechnology*, vol. 12, no. 4, pp. 417–422, Feb. 2018, ISSN: 1751-875X. DOI: 10.1049/iet-nbt.2017.0128. [Online]. Available: http://dx.doi.org/10.1049/iet-nbt.2017.0128.

[62] F. Rizzotto, M. Khalife, Y. Hou, *et al.*, "Recent advances in electrochemical biosensors for food control," *Micromachines*, vol. 14, no. 7, p. 1412, Jul. 2023, ISSN: 2072-666X. DOI: 10.3390/mi14071412. [Online]. Available: http://dx.doi.org/10.3390/mi14071412.

[63] H. Qi, C. Ling, R. Huang, *et al.*, "Functionalization of single-walled carbon nanotubes with protein by click chemistry as sensing platform for sensitized electrochemical immunoassay," *Electrochimica Acta*, vol. 63, pp. 76–82, Feb. 2012, ISSN: 0013-4686. DOI: 10.1016/j.electacta.2011.12.084. [Online]. Available: http://dx.doi.org/10.1016/j.electacta.2011.12.084.

[64] H. Qi, M. Li, R. Zhang, M. Dong, and C. Ling, "Double electrochemical covalent coupling method based on click chemistry and diazonium chemistry for the fabrication of sensitive amperometric immunosensor," *Analytica Chimica Acta*, vol. 792, pp. 28–34, Aug. 2013, ISSN: 0003-2670. DOI: 10.1016/j.aca.2013.06.046. [Online]. Available: http://dx.doi.org/10.1016/j.aca.2013.06.046.

[65] S. Ge, W. Liu, L. Ge, *et al.*, "In situ assembly of porous au-paper electrode and functionalization of magnetic silica nanoparticles with hrp via click chemistry for microcystin-lr immunoassay," *Biosensors and Bioelectronics*, vol. 49, pp. 111–117, Nov. 2013, ISSN: 0956-5663. DOI: 10.1016/j.bios.2013.05.010. [Online]. Available: http://dx.doi.org/10.1016/j.bios.2013.05.010.

[66] S. Ge, M. Sun, W. Liu, *et al.*, "Disposable electrochemical immunosensor based on peroxidase-like magnetic silica–graphene oxide composites for detection of cancer antigen 153," *Sensors and Actuators B: Chemical*, vol. 192, pp. 317–326, Mar. 2014, ISSN: 0925-4005. DOI: 10.1016/j.snb.2013.10.127. [Online]. Available: http://dx.doi.org/10.1016/j.snb.2013.10.127.

[67] E. Sánchez-Tirado, A. González-Cortés, P. Yáñez-Sedeño, and J. M. Pingarrón, "Carbon nanotubes functionalized by click chemistry as scaffolds for the preparation of electrochemical immunosensors. application to the determination of tgf-beta 1 cytokine," *The Analyst*, vol. 141, no. 20, pp. 5730–5737, 2016, ISSN: 1364-5528. DOI: 10.1039/c6an00941g. [Online]. Available: http://dx.doi.org/10.1039/C6AN00941G.

[68] Y. Zheng, L. Zhao, and Z. Ma, "Ph responsive label-assisted click chemistry triggered sensitivity amplification for ultrasensitive electrochemical detection of carbohydrate antigen 24-2," *Biosensors and Bioelectronics*, vol. 115, pp. 30–36, Sep.

2018, ISSN: 0956-5663. DOI: 10.1016/j.bios.2018.05.026. [Online]. Available: http://dx.doi.org/10.1016/j.bios.2018.05.026.

[69] T. S. Svalova, M. V. Medvedeva, A. A. Saigushkina, *et al.*, "A label-free impedimetric immunosensor based on covalent immobilization of anti-e. coli antibody via a copper-catalyzed azide-alkyne cycloaddition reaction," *Analytical and Bioanalytical Chemistry*, vol. 412, no. 21, pp. 5077–5087, Jan. 2020, ISSN: 1618-2650. DOI: 10.1007/s00216-019-02381-1. [Online]. Available: http://dx.doi.org/10.1007/s00216-019-02381-1.

[70] S. Bonaldo, L. Franchin, G. Rosati, A. Merkoçi, and A. Paccagnella, "Multiphysics modeling of the electrochemical response of screen-printed electrodes for sensing applications," *IEEE Sensors Journal*, vol. 24, no. 15, pp. 23 960–23 967, Aug. 2024, ISSN: 2379-9153. DOI: 10.1109/jsen.2024.3410094. [Online]. Available: http://dx.doi.org/10.1109/JSEN.2024.3410094.

[71] COMSOL, Inc., *COMSOL Multiphysics*, https://www.comsol.com/comsol-multiphysics, Accessed: 17/02-2025.

[72] COMSOL, Inc., *COMSOL Multiphysics Reference Manual*, version 6.2, Accessed: [Insert Date], 2022. [Online]. Available: https://doc.comsol.com/6.2/doc/com.comsol.help.comsol/COMSOL_ReferenceManual.pdf.

[73] E. J. Dickinson, H. Ekström, and E. Fontes, "Comsol multiphysics®: Finite element software for electrochemical analysis. a mini-review," *Electrochemistry Communications*, vol. 40, pp. 71–74, Mar. 2014, ISSN: 1388-2481. DOI: 10.1016/j.elecom.2013.12.020. [Online]. Available: http://dx.doi.org/10.1016/j.elecom.2013.12.020.

[74] COMSOL Multiphysics, *Introduction to the electrochemistry module*, COMSOL AB, 2024. [Online]. Available: https://doc.comsol.com/6.3/doc/com.comsol.help.echem/IntroductionToElectrochemistryModule.pdf.

[75] COMSOL Multiphysics, *Electrochemistry module user's guide*, Accessed: 16 February 2025, COMSOL AB, 2022. [Online]. Available: https://doc.comsol.com/6.2/doc/com.comsol.help.echem/ElectrochemistryModuleUsersGuide.pdf.

[76] D. Stan, A.-C. Mirica, R. Iosub, *et al.*, "What is the optimal method for cleaning screen-printed electrodes?" *Processes*, vol. 10, no. 4, p. 723, Apr. 2022, ISSN: 2227-9717. DOI: 10.3390/pr10040723. [Online]. Available: http://dx.doi.org/10.3390/pr10040723.

[77] J. Lee, D. W. Arrigan, and D. S. Silvester, "Mechanical polishing as an improved surface treatment for platinum screen-printed electrodes," *Sensing and Bio-Sensing Research*, vol. 9, pp. 38–44, Jul. 2016, ISSN: 2214-1804. DOI: 10.1016/j.sbsr.2016.05.006. [Online]. Available: http://dx.doi.org/10.1016/j.sbsr.2016.05.006.

[78] R. L. McCreery, "Advanced carbon electrode materials for molecular electrochemistry," *Chemical Reviews*, vol. 108, no. 7, pp. 2646–2687, Jun. 2008, ISSN: 1520-6890. DOI: 10.1021/cr068076m. [Online]. Available: http://dx.doi.org/10.1021/cr068076m.

[79] N. O. Laschuk, E. B. Easton, and O. V. Zenkina, "Reducing the resistance for the use of electrochemical impedance spectroscopy analysis in materials chemistry," *RSC Advances*, vol. 11, no. 45, pp. 27 925–27 936, 2021, ISSN: 2046-2069. DOI: 10.1039/d1ra03785d. [Online]. Available: http://dx.doi.org/10.1039/D1RA03785D.

[80] J. Pla-Tolós, Y. Moliner-Martinez, C. Molins-Legua, and P. Campins-Falcó, "Colorimetic biosensing dispositive based on reagentless hybrid biocomposite: Application to hydrogen peroxide determination," *Sensors and Actuators B: Chemical*, vol. 231, pp. 837–846, Aug. 2016, ISSN: 0925-4005. DOI: 10.1016/j.snb.2016.03.094. [Online]. Available: http://dx.doi.org/10.1016/j.snb.2016.03.094.

[81] M. Vazquez-Alvarado, S. Vanasupa, E. H. Valdez, *et al.*, "Evaluation of chromogenic substrates for horseradish peroxidase on paper-based microfluidic devices," *Sensors and Actuators B: Chemical*, vol. 377, p. 133 028, Feb. 2023, ISSN: 0925-4005. DOI: 10.1016/j.snb.2022.133028. [Online]. Available: http://dx.doi.org/10.1016/j.snb.2022.133028.

[82] K. Teeparuksapun, M. Hedström, and B. Mattiasson, "A sensitive capacitive biosensor for protein a detection using human igg immobilized on an electrode using layer-by-layer applied gold nanoparticles," *Sensors*, vol. 22, no. 1, p. 99, Dec. 2021, ISSN: 1424-8220. DOI: 10.3390/s22010099. [Online]. Available: http://dx.doi.org/10.3390/s22010099.

A Method 3 Protocol

Step 1: Formation and Activation of the MUA Layer

1. **Electrode Cleaning:**
   Clean the electrodes mechanically by polishing, followed by electrochemical cleaning.

2. **SAM of MUA Formation:**
   Prepare a MUA solution by dissolving the required amount of MUA in absolute ethanol first, then add an equal volume of Milli-Q water, and mix thoroughly. Immerse the electrodes in the solution in Eppendorf tubes, and incubate overnight at 4°C."
   Rinse afterwards with Milli-Q water.
   Verify the MUA layer.

3. **Activation with EDC/NHS:**
   Prepare a fresh batch of EDC/NHS solution.
   Add the EDC/NHS solution onto the WE and incubate it for 40 minutes at RT.
   Then, rinse with Milli-Q water.

Step 2: Conjugation of the Alkyne Layer

1. **Preparation of Alkyne Stock Solution:**
   To obtain a stock solution of 200 μL 200 mM Alkyne, dissolve 5.78 μL of Alkyne in 194.2 μL of DMSO and mix thoroughly.

2. **10X Dilution of Alkyne Stock:**
   To obtain a ten-fold dilution of Alkyne; transfer 10 μL of the stock solution into a new tube and add 90 μL of DMSO, resulting in a 20 mM alkyne solution.

3. **Application of the Alkyne Layer:**
   Add 5 μL of the 20 mM Alkyne solution to the activated MUA layer, and incubate for 1-2 hours at RT.

Rinse will Milli-Q water
Apply blocking agent either at this step (before the click reaction) or after click reaction occurs.

Step 3: Bioconjugation of Azide-Antibody (Azide-Ab)

1. **Preparation of Antibody Stock Solution:**
   Dilute the BAM1676 stock solution (V=5 μL, C=500 μg/mL) with 45 μL PBS to achieve a final concentration of 50 μg/mL.

2. **Preparation of Azide Stock Solution:**
   Prepare a 200 mM working stock solution from parent stock (with a concentration of 2.3 M).

3. **10X Dilution of Azide Stock:**
   To obtain a ten-fold dilution of Azide; transfer 1.74 μL of the working stock solution into a new tube and add 198.26 μL of DMSO, resulting in a 20 mM Azide solution.

4. **Formation of Azide-Antibody Conjugate:**
   Transfer 5 µL of the 20 mM Azide solution with 50 μL of the antibody solution, and incubate for 2 hours on ice or 30 minutes at RT.
   Then, add 1 μL of hydroxylamine to act as quencher.

Step 4: Click Reaction Via Two Approaches

The Copper(I)-catalysed Azide-Alkyne Cycloaddition (CuAAC) reaction can be performed using two distinct approaches. In both cases a droplet of 35 μL consisting of 30.75 µL of 0.5 M NaCl, 1.25 µL of $CuSO_4$, and 3 μL of Azide-Ab solution is applied. he required potential should be determined beforehand from CV experiments. Below are the detailed descriptions of the two approaches:

Approach 1: Sequential Activation and Click Reaction

1. **Preparation of Solutions:**
   (1) Prepare a solution of containing NaCl and $CuSO_4$
   (2) Prepare a solution of Azide-Ab

2. **Electrochemical Activation:**
   Apply 32 μL solution (1) to the electrode, and run CA at 160 mV for 15 minutes to electrochemically reduce Cu^{2+} to Cu^{+}, and hence activating the electrode surface for the click reaction.

3. **Click Reaction:**
   Immediately after activation, add 3 μL of Azide-Ab solution (2) to the electrode. Incubate for 2 hours at RT to allow the Cu^{+}-catalysed cycloaddition between the Alkyne and Azide-Ab to proceed.

4. **Washing and Blocking:**
   Rinse the electrode with PBS, followed by Milli-Q water to remove unbound reagents.
   At this step, the electrode surface can be blocked to prevent non-specific unbound reagents.
   Detection and Measurement:
   Add Strep-HRP, and incubate for 30 minutes at RT.
   Rinse with PBS, and Milli-Q water, then gently dry the electrode under nitrogen flow.
   Perform the final measurement by adding a droplet of Turbo TMB solution, and running CA at 0.0 V for 120 seconds.

Approach 2: One-Step Activation and Click Reaction

1. **Preparation of Solutions:**
   (1) Prepare a solution of containing NaCl and $CuSO_4$
   (2) Prepare a solution of Azide-Ab

2. **Electrochemical Activation and Click Reaction:**
   Add all solutions (1 and 2) onto the electrode with total volume of 35 μL.
   Run CA at 160 for 15 minutes to electrochemically reduce Cu^{2+} to Cu^{+}, activating the electrode surface for the click reaction.
   Incubate the system for 2 hours at RT to allow the Cu^{+}-catalysed cycloaddition between the Alkyne and Azide-Ab to proceed.

3. **Washing and Blocking:**
   Rinse the electrode with PBS, followed by Milli-Q water to remove unbound reagents.
   At this step, the electrode surface can be blocked to prevent non-specific unbound reagents.
   Detection and Measurement:
   Add Strep-HRP, and incubate for 30 minutes at RT.
   Rinse with PBS, and Milli-Q water, then gently dry the electrode under nitrogen flow.
   Perform the final measurement by adding a droplet of Turbo TMB solution, and running CA at 0.0 V for 120 seconds.